

TOPICAL REVIEW

Review: Pellet injection experiments and modelling

To cite this article: B Pégourié 2007 *Plasma Phys. Control. Fusion* **49** R87

View the [article online](#) for updates and enhancements.

You may also like

- [Statistical assessment of ELM triggering by pellets on JET](#)

M. Lennholm, R. McKean, R. Mooney et al.

- [Comparing spontaneous and pellet-triggered ELMs via non-linear extended MHD simulations](#)

A Cathey, M Hoelzl, S Futatani et al.

- [Achieving temporary divertor plasma detachment with MARFE events by pellet injection in the EAST superconducting tokamak](#)

Guozhong Deng (), Liang Wang (), Xiaoju Liu () et al.

TOPICAL REVIEW**Review: Pellet injection experiments and modelling****B Pégourié**Association Euratom-CEA, CEA/DSM/DRFC, Centre de Cadarache,
13108 Saint-Paul-Lez-Durance, FranceE-mail: bernard.pegourie@cea.fr

Received 10 January 2007, in final form 10 April 2007

Published 2 July 2007

Online at stacks.iop.org/PPCF/49/R87**Abstract**

During the last decade, significant progress has been made in the field of pellet injection with (1) the identification of the drift of the deposited material in the inhomogeneous magnetic field that opened the possibility of fuelling efficiently the plasmas from the high-field side of the torus, (2) the technique to mitigate ELMS in H-mode discharges with shallow pellet injection at high frequency and (3) with the development of high density, high performance scenarios close to the ITER requirements. Both the experimental and theoretical aspects of this domain are reviewed in this paper.

(Some figures in this article are in colour only in the electronic version)

Contents

1. Introduction	88
2. Ablation physics	90
2.1. Measurements	90
2.1.1. Cloud characteristics.	90
2.1.2. Ablation rate and pellet penetration.	91
2.1.3. Pellet trajectory.	93
2.2. Ablation models	93
2.2.1. Shielding mechanisms	93
2.2.2. Ablation models—previous situation	94
2.2.3. Ablation models—recent developments.	95
2.2.4. Ablation models—discussion	100
2.3. Striations	103
2.3.1. Striations characteristics.	103
2.3.2. Striations models	103
3. Homogenization of the pellet material	104
3.1. Measurements	104
3.1.1. Parallel expansion.	105
3.1.2. Plasma potential modification.	105
3.1.3. Outward displacement and drift velocity.	105

3.2.	Homogenization models	107
3.2.1.	Parallel expansion and potential perturbation.	107
3.2.2.	∇B -induced drift	109
4.	Fast plasma response	117
4.1.	MHD phenomena	117
4.1.1.	Impact on MHD activity.	117
4.1.2.	Interaction of pellets with the $q = 1$ surface.	117
4.1.3.	Snakes.	118
4.1.4.	Pellet-induced ELMs.	119
4.2.	Non-local transport	121
4.3.	Loop voltage modification	123
5.	Fuelling efficiency	124
5.1.	Dependence on injection and plasma characteristics	124
5.2.	Global particle balance	126
6.	High density/high performance scenarios	127
6.1.	H-mode plasmas	127
6.1.1.	L–H transition and operational domain.	127
6.1.2.	Integrated scenarios.	129
6.2.	ITBs plasmas	132
6.2.1.	Pellet-induced ITBs.	132
6.2.2.	Confinement and transport properties.	134
6.3.	Other regimes and confinement devices	136
6.3.1.	Other confinement regimes	136
6.3.2.	Stellarators and reversed field pinches.	139
7.	Pellets for plasma control	140
7.1.	ELMs mitigation	140
7.2.	Wall conditioning	141
7.3.	Fast plasma termination	142
8.	Pellets for diagnostic purpose	145
8.1.	Heat and particle transport	145
8.2.	Current density profile	148
8.3.	α -population	150
9.	ITER projections	151
10.	Concluding remarks	154
	References	155

1. Introduction

For more than three decades now both experimental and theoretical work has been devoted to the study of pellet injection in fusion devices and the whole development of the domain can be followed in the different reviews and Technical Committee Meeting reports already published. For present day and future devices, pellet injection has become a leading technique not only for fuelling purposes, but also for controlling the plasma, with applications in both core and edge physics. If the first studies were aiming at the estimation of the fuelling capability of pellets, it was rapidly noted that pellet injection was associated with a transient improvement of the confinement and allowed to operate at a higher density in both L and H-mode regimes, these beneficial effects often being linked to a nearly central matter deposition [1–5]. Rapidly, in all these experiments where the pellets were launched from the low-field side of the torus, it was noted that the fuelling efficiency, defined as the proportion of the pellet initial mass that

was remaining inside the plasma, was increasing with the pellet penetration. Correlatively, the matter deposition profile (i.e. the increment of plasma density) was observed to be significantly shifted in the direction of the major radius with respect to the ablation profile [2, 4, 5]. For this reason, an important part of the research and development in pellet injectors technology (which is not reviewed in the present paper) was devoted to the increase in the injection velocity. Concerning this field, and in addition to the information that can be found in the general reviews on pellet injection [1, 2, 4–6], more details are given in the two dedicated reviews [7, 8]. Simultaneously, estimations were given of the performances in terms of pellet size and velocity allowing to fuel a fusion reactor [9], with detailed simulations of the possible scenarios [2, 4, 5]. On the physics of the ablation process, a review of the early models can be found in [6]. Among the different phenomena invoked to explain the pellet self-shielding, the dissipation of the energy carried by the plasma electrons (and ions) in the cold and dense neutral cloud surrounding the pellet was shown to be dominant, and the corresponding model (the so-called neutral gas shielding model [10], hereafter referred to as the NGS model) widely used due to its capability to satisfactorily reproduce the pellet penetrations for a large range of plasma and pellet characteristics in several devices. Other shielding mechanisms were introduced later, in particular the one due to the ionized part of the ablation cloud (plasma shielding [1, 2]) and the one due to the charge of the ablation cloud with respect to the background plasma (electrostatic shielding [5]). Simultaneously, the main characteristics of the ablation cloud (dimensions, density, temperature, dynamics) were measured in a wide variety of situations (pellet material and plasma parameters in tokamaks, stellarators or reversed field pinches), this comprehensive set of data allowing a tight test of the different ablation models presently available.

The present paper focuses on the results obtained since the last review of Milora, Houlberg, Lengyel and Mertens in 1994 [5]. In this last paper, the emphasis was put on the increase in the operational domain with pellet injection, in relation to the modification of the current profile in the plasma core in the case of central penetration, and on the phenomenon of ‘prompt mass loss’ leading to limited fuelling efficiencies in the case of moderate penetrations, in relation to the outward displacement of the matter deposition with respect to the ablation profile. Since this time, constant progress has been made in the understanding of the confinement improvement consecutively to the injection of a pellet and this technique is now used to trigger ITBs and in integrated scenarios at high density and close to those envisaged in ITER. As regards the fuelling, it was demonstrated that the outward displacement of the matter deposition profile (and associated ‘prompt mass loss’) was in fact due to a drift of the pellet material down the magnetic field gradient. If, in tokamaks, this drift expels the deposited matter out of the discharge in the case of low-field side deposition, it favours its penetration when the deposition is on the high-field side. So, an important experimental effort was made to explore the possibilities offered by this new injection configuration, with significant technological consequences. Indeed, in the case of high-field side injection, the geometry of the guide tube is complicated and the stress experienced by the pellet in the curved sections limits the maximum injection velocity. Therefore, it now seems less critical to dispose of high-velocity pellet injectors to fuel a reactor scale device. Finally, an important finding was made in the control of the plasma edge in the H-mode regime with the demonstration that it was possible to control the ELMs size and frequency with the injection of shallow pellets at a high rate.

This constant progress has motivated an important body of literature. In order to limit the bibliography—and except in a few cases—only papers published in peer-reviewed journals, subsequently to the publication of [5], are referred to in the present review. The main topics are pellet ablation and matter deposition, pellet-induced transport modifications and the use of pellets as diagnostics, the high-performance integrated scenarios in present day tokamaks

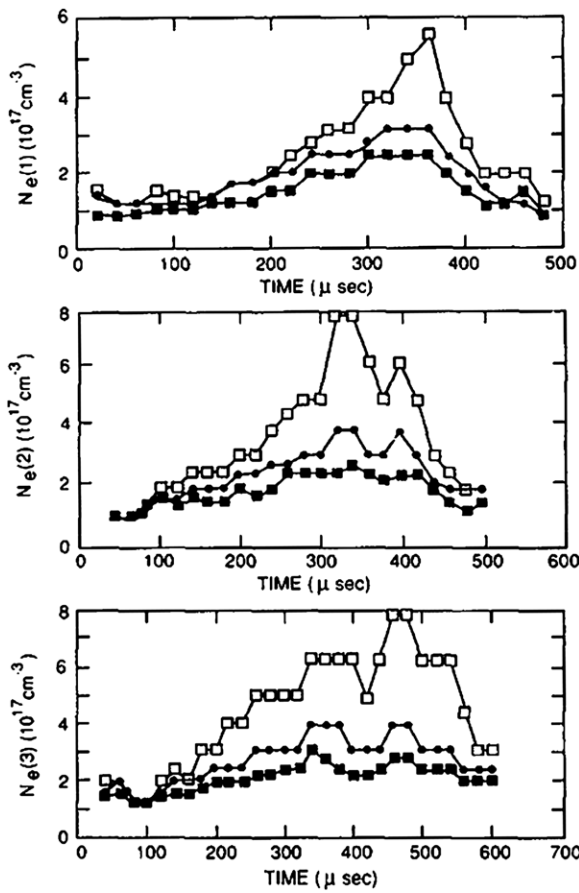


Figure 1. Time variation of the electron density $n_e(j)$ in the luminous region of a sequence of three TFTR pellets ($j = 1, 2, 3$). The different curves are calculated assuming that the emitting region is a spherical shell of thickness Δ . The densities corresponding to the model fits with $\Delta = 0$ (hollow squares), 0.5 (solid circles) and 2.0 cm (solid squares) are plotted. The best fit data correspond to $0.2 < \Delta \leq 0.5$ cm, giving $n_e = (3 \pm 1) \times 10^{17} \text{ cm}^{-3}$ during most of the lifetimes of all three pellets [15].

and their extrapolation to the next step and, finally, the use of pellets as a means to control the plasma.

2. Ablation physics

2.1. Measurements

2.1.1. Cloud characteristics. The first measurements of the ablation cloud characteristics were made in the early 1980s in ISX-B, PLT, TFR, TEXT and TFTR [11–15]. From ruby laser interferometry and spectroscopic measurements analysis (ratio between the continuum and the H α (D α) emission or H α /H β , profile analysis of the H α line), it was estimated that the density is 10^{25} – 10^{26} m^{-3} in the neutral cloud, close to the pellet surface, and 10^{23} – 10^{24} m^{-3} in the cigar-shaped emitting region—figure 1, with temperatures ranging from 1 to 4 eV. These values were confirmed by more recent measurements in ASDEX-U, T10 and JIPPT-IIU [16–19], in which identical temperatures are measured, and densities from 10^{23} to $(3.5\text{--}5) \times 10^{23} \text{ m}^{-3}$ in

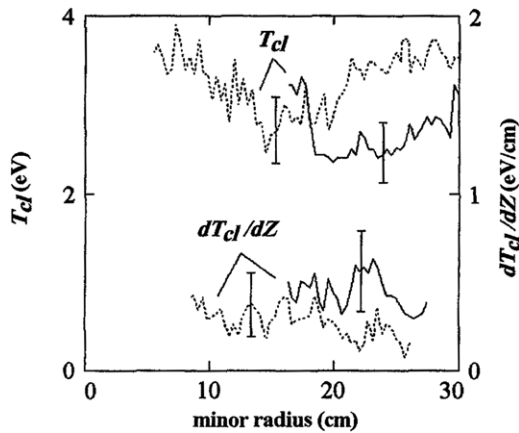


Figure 2. Central cloud temperature along the pellet path and spatial gradient along field lines in T10 discharges 58514 (full line) and 58517 (dotted line) [18].

the cloud surrounding the pellet. At the beginning of the homogenization phase, 5 to $10\ \mu\text{s}$ after the ablated material is deposited, the temperature increases up to 20–25 eV and the density decreases to $(1\text{--}2) \times 10^{22}\ \text{m}^{-3}$ [17]. Spatially resolved measurements were also made in T10 on hydrogen pellets, showing that the temperature is constant on a distance of $\sim 4\ \text{cm}$ along field lines, and then increases with a gradient of $0.3\text{--}0.4\ \text{eV cm}^{-1}$ [18, 20], figure 2. Finally, during injection of micro-pellets of aluminium in the MT-1M tokamak, the propagation of Al ions of different ionization degrees was analysed from spectroscopic measurements [21]. In the RFX reversed field pinch, both the density in the ionized part of the cloud and the ablation rate were simultaneously estimated from line integrated density measurements [22]. It is shown that the ablation rate is from 2 to 2.5 higher than what it is in tokamaks for similar plasma conditions (i.e. 2–2.5 higher than the neutral gas shielding model prediction) and that, correlatively, the density in the ionized part of the cloud is only $\sim 10^{21}\ \text{m}^{-3}$, about two orders of magnitude lower than its value in tokamaks. This high-ablation rate and low-cloud density are possibly due to the high transport that characterizes the RFP configuration and relatively low-magnetic field at the measurement location ($\sim 0.5\ \text{T}$).

2.1.2. Ablation rate and pellet penetration. On the ablation rate itself, there is no local measurement—except that in RFX reported above—and the only constraint available is the measurement of the pellet penetration (if one excludes the rough estimate given by the H α emission, assuming it is proportional to the pellet mass loss rate). In several cases, successful comparisons between experimental penetrations and model predictions have been performed, but on a limited parameter range (see [23] in HL-1M, [24] in Tore Supra or [25] in JET). To overcome this difficulty, and since ablation models are not supposed to be machine dependent, an international database (IPADBASE, for International Pellet Ablation Data Base) has been constituted [26]. In its initial version, it was regrouping data from nine machines (JET, Tore Supra, DIII-D, FTU, TFTR, ASDEX, JIPPT-IIU, RTP and T10), with about an order of magnitude of variation for both the pellet and plasma characteristics (density, temperature, injection velocity and pellet equivalent radius—i.e. three orders of magnitude in the pellet particle content), the range of parameters corresponding to each particular machine being of course more limited. A first analysis of the dependences of penetrations with pellet and plasma parameters led to a scaling close to that predicted by the NGS model, figure 3. The

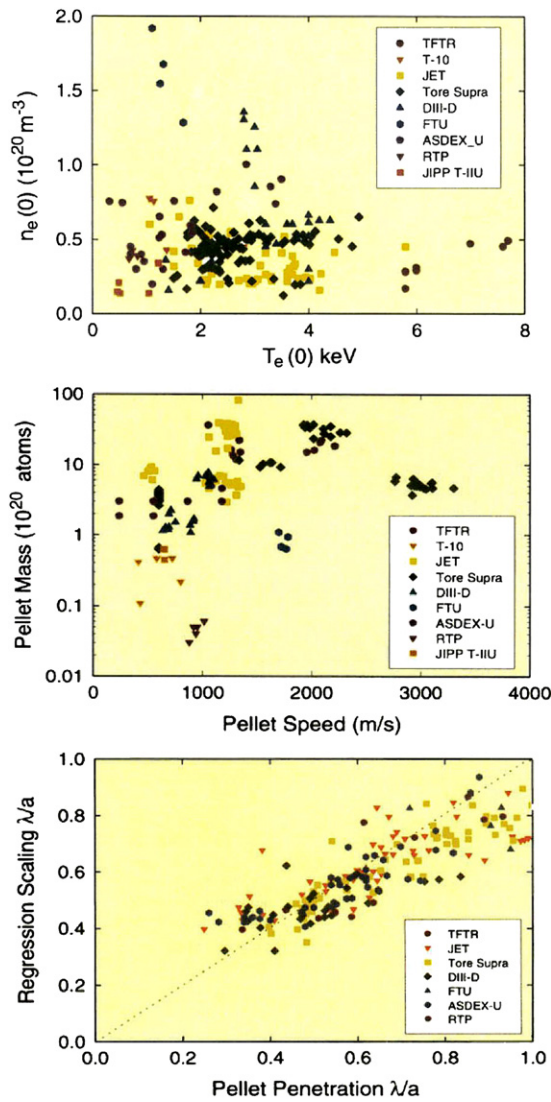


Figure 3. IPADBASE: (top) Plasma central electron density and temperature at the time of pellet injection identified by tokamak device. (middle) Pellet particle content and injection velocity. (bottom) Comparison of penetration depth with scaling using regression analysis [26]: $\lambda_p/a = 0.079 \times T_e \text{ (keV)}^{-0.51} \times n_e \text{ (10}^{20} \text{ m}^{-3}\text{)}^{-0.03} \times N_p \text{ (10}^{20} \text{ atoms)}^{0.12} \times v_p \text{ (m s}^{-1}\text{)}^{0.32}$.

IPADBASE was also used to assess the accuracy of specific ablation models, either from a case-to-case comparison between data and calculations [27, 28] or by using the scaling deduced from the general study mentioned above [29]. In stellarators, penetration measurements show that the physics of ablation is identical to what it is in tokamaks (which is not the case in RFPs, where ablation is enhanced by a factor of the order of ~ 2 , see section 2.1.2). As long as the injected power remains moderate, the ablation follows the NGS scaling, for hydrogen as well as impurity pellets [30, 31]. In such conditions, the pellet fuelling efficiency is high: typically higher than 50% and up to 100%. In the case where the injected power is high, over-ablation is observed—often localized—that is due to the interaction of the pellet with the high-energy

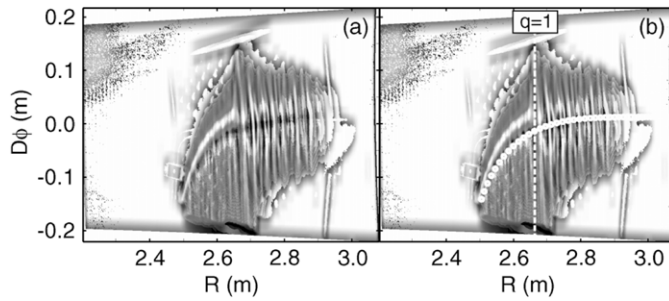


Figure 4. (a) Ablation pattern of a pellet injected in a Tore Supra ohmic discharge. The pellet is injected from right to left. $D\phi$ is the toroidal direction and R the major radius. (b) The same picture with the trajectory calculated by taking into account the Spitzer–Härm distortion of the electron distribution superimposed (circles) [37].

electrons or ions. Such effects are seen in tokamaks as well as in stellarators, with hydrogen or carbon pellets [28, 32–34]. However, the phenomenon at the basis of the increase in ablation differs depending on whether one considers electrons or ions: when hot ions deposit all their energy in the ablation cloud and first layers of the pellet surface, leading to an immediate increase in the ablation rate, high-energy electrons (>100 – 200 keV) cross the pellet from part to part and heat the ice in volume yielding, in some cases, to the whole pellet sublimation [28]. It is generally observed that the fuelling efficiency decreases with increasing power.

2.1.3. Pellet trajectory. In a number of experiments, the pellet trajectory is observed to be deflected in the toroidal and/or poloidal directions. This is due to the asymmetry of the electron or ion distribution function, which yields an unbalance of the ablation on the two sides of the pellet. The associated rocket effect is the cause of the pellet acceleration in the direction opposite to the side where ablation is stronger. In ohmic plasmas, the asymmetry is due to the distortion of the electron distribution function by the parallel electric field [35], figure 4. The observed deflection can then be used to characterize the electron distribution, as was done in RFX and Tore Supra [36, 37] or to determine the current profile, as in T10 [38, 39], see section 8.2. At low density, the origin of the unbalance of ablation can be the increase in the population of runaways consecutively to the injection of a previous pellet [40, 41]. In the case of high-additional power, as for unbalanced neutral beam injection (NBI), it is the asymmetry of the high-energy ion tail that is the cause of the deflection, figure 5. That was measured in LHD, with carbon pellets [32] and in CHF, with hydrocarbon pellets [42].

2.2. Ablation models

2.2.1. Shielding mechanisms For both hydrogen or impurity pellets, ablation is a self-regulated process, in the sense that the ablation cloud self-adapts for the heat flux at the pellet surface to be just enough to maintain the shielding capability of the cloud (i.e. its line integrated density) at the adequate value. By order of increasing importance, the phenomena that reduce the incident heat flux at the pellet surface are as follows:

- (i) The magnetic shielding, due to the partial expulsion of the magnetic field from the cloud interior by the expanding plasma, and the associated reduction of the incident heat flux. Almost negligible for present-day experiments (few %), it could be more efficient in reactor grade plasmas, due to the strong diamagnetism of the ablation cloud in such conditions.

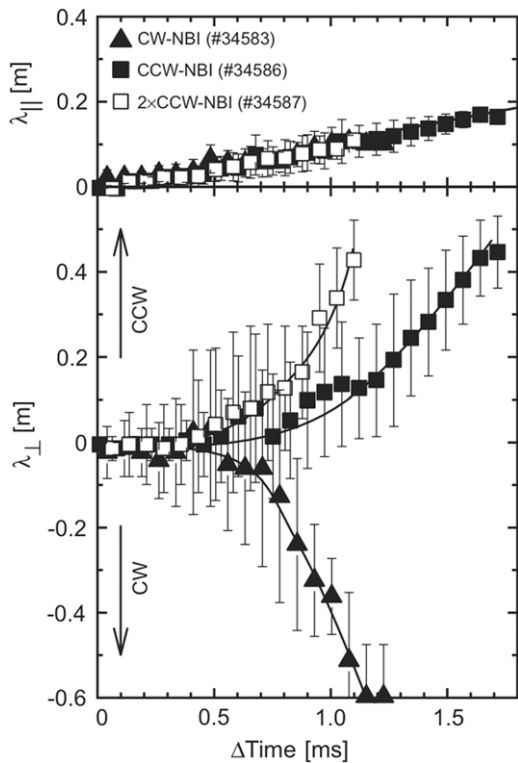


Figure 5. Plots of the pellet cloud motion in LHD plasmas, in both clockwise (CW) and counter-clockwise (CCW) NBI heating experiments. The movement is separated into the injection direction (λ_{\parallel}) and the field line direction (λ_{\perp}) [32].

- (ii) The electrostatic shielding, due to the negative charge of the cloud with respect to the background plasma. The associated negative potential accelerates the ions and repels the electrons, which lowers the electron energy flux at the cloud entrance and thus at the pellet surface. In what concerns the thermal ions, since they dissipate all their energy in the outer layers of the ablation cloud, they do not contribute directly to the ablation process. It follows that the presence of a negative sheath at the plasma–cloud interface significantly reduces the heat flux at the pellet surface.
- (iii) The gas dynamic—neutral gas and/or plasma—shielding, due to the collisions between the incident plasma particles and that of the cloud, which is responsible for the ionization and heating of the ablatant. This process is, by far, the most important for hydrogen pellets that—due to the low-sublimation energy of molecular hydrogen ($(1-1.5) \times 10^{-2} \text{ eV mol}^{-1}$)—are almost completely shielded by the ablation cloud ($q_p/q_{\infty} \sim 0$ and $E_p/E_{\infty} \sim 0$, where q and E are the heat flux and energy of the incident particles, and where the subscripts ‘p’ and ‘ ∞ ’ refer to the pellet surface and background plasma, respectively). Conversely, for impurity pellets, the sublimation energy is much higher ($\sim 7.5 \text{ eV/atom}$ for carbon) and the shielding of the pellet is only partial ($q_p/q_{\infty} \sim 0.7$).

2.2.2. Ablation models—previous situation Three approximations characterize the early ablation models: the gas dynamic shielding was the only mechanism considered, the cloud expansion was assumed to be spherically symmetric and the electron Maxwellian distribution

was replaced by a mono-energetic beam [10, 43]. Under these assumptions, the pellet radius regression speed was shown to scale as $r_p^{-2/3} n_\infty^{1/3} T_\infty^{1.64}$, the so-called NGS scaling. A further study including—with the same approximations—the effect of dissociation, ionization and radiative losses showed that these atomic processes were of low impact on the ablation rate and confirmed the previous scaling [44]. In what concerns impurity pellets, an ablation model was built on the same basis. Its main characteristics are that the vaporization front is treated as a shock, the cloud expansion dynamics is calculated in a simplified manner and only one degree of ionization of the ablatant is considered [45]. Despite these important simplifications, these models have shown a remarkable capability to reproduce the experiments. This has been verified for JET [25] and also for the whole IPADB BASE whose experimental dependences of ablation are very close to that of the NGS scaling [26], see section 2.1.2. Since this time, more sophisticated models have been developed, taking into account—although in a simplified way—the change in the geometry of the cloud expansion once it is ionized (from spherically symmetric to purely parallel) [2, 46–48] and the explicit shape of the distribution function of the incident particles (electrons and high-energy ions, in the case of beam injection) [47, 49]. Nevertheless, several questions were yet open, requiring a more rigorous treatment. When going from the pellet to the outer part of the ablation cloud, they are as follows:

- (i) The influence of the inhomogeneous heat flux in the cloud and at the surface of the pellet (i.e. the fact that it is directed along the magnetic field) and the phase solid–vapour transition at the pellet–cloud interface.
- (ii) The account for the inhomogeneous heating of the cloud due to Maxwellian distributions and the consequence of atomic physics on the expansion, especially in the case of impurity pellets.
- (iii) The accurate description of the dynamics of the cross-field expansion and transition to pure parallel expansion once the cloud conductivity becomes high enough for the flow to follow the magnetic field.
- (iv) The determination of the potential distribution in the cloud and at the cloud–plasma interface, that lowers the electron heat flux and changes the local heating rate.
- (v) Finally, it must be noted that all the models mentioned above are intrinsically steady state, in the sense that the ablation rate is calculated assuming a fully developed ablation cloud.

2.2.3. Ablation models—recent developments. Several points are included in the recent version of ablation models. For hydrogen pellets:

(i) In what concerns the anisotropy of the plasma heat flux introduced by the presence of the magnetic field, MacAulay calculates the 2D modification of the geometry of the cloud expansion and of the heat flux distribution at the pellet surface [50]. However, in this model, the pellet is assumed to remain always spherical and only an averaged speed is considered for the regression of the pellet surface.

On the same point, Kuteev [51] removes the approximation of a spherical pellet, which then takes the shape of a lentil, the surface regression rate being larger for the areas perpendicular to the magnetic field. But in this case, it is the cloud that is assumed to be spherically symmetric and to expand at the sonic velocity (Mach number equal 1 everywhere in the cloud). Two variations of the model are proposed, depending on whether the cloud is negatively charged—or not—with respect to the plasma. In the first case, the electrons are repelled by the cloud potential when the ions are accelerated, which lowers the electron heat flux at the poles of the pellet and increases the ion flux at its equator (with respect to the magnetic field direction). The resultant heat flux distribution is almost uniform and the shape of the pellet remains close to a sphere. Conversely, if there is no difference of potential between the pellet and the plasma,

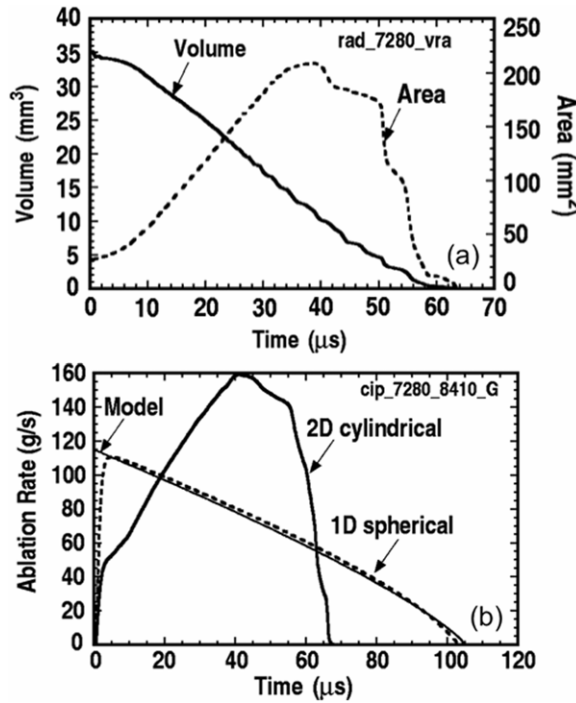


Figure 6. (a) Time dependence of the volume (full line) and area of the pellet projected normal to the magnetic field lines (dashed line)—i.e. effective area which absorbs the incoming heat flux—for a constant heat flux over the pellet lifetime. The initial pellet radius is 2 mm. Although the volume decreases monotonically with time due to surface recession, the area increases at first due to the pellet flattening, reaches a peak, and then falls to zero later on. (b) Time dependence of the pellet ablation rate. The solid curve pertains to 2D cylindrical axisymmetric geometry, taking into account the pellet flattening, the dashed curve is for the 1D spherically symmetric geometry. The thin solid line is the ablation rate from the NGS scaling law [29].

the ions are stopped in the outer layers of the cloud and the heat flux is strongly anisotropic, leading to a lentil-shaped pellet as mentioned above. Despite the differences in the distribution of ablation at the pellet surface, the global ablation rate predicted in the two cases is almost identical.

Parks and collaborators consider simultaneously the influence of the magnetic field on the heating of the cloud and on the distribution of the heat flux and ablation at the pellet surface [29, 52]. In this model, the solid–vapour interface is treated without imposing an ad hoc boundary condition at the pellet surface. One of the most important results is that, under high-heat flux conditions, the stress due to the non-uniform pressure distribution at the pellet surface can exceed the yield strength of the solid and become high enough for the pellet to be fluidized and flattened into a ‘pancake’ shape. The equilibrium shape is that of an oblate spheroid of elongation ~ 2 [53]. The resultant increase in the pellet surface also enhances the ablation rate and shortens the pellet lifetime, by as high a factor as 3 for reactor grade conditions, figure 6 [29]. The importance of this effect remains to be confirmed, however, since recent MHD simulations by Samulyak, Lu and Parks [54] show that the anisotropy of the pressure distribution at the pellet surface can be strongly reduced when both the $j \times B$ force and electrostatic shielding are taken into account.

Quantitatively, the different developments described above confirm the NGS scaling of the ablation rate with the pellet and plasma parameters—at least as long as the pellet remains

spherical—and agree on the fact that to take into account the anisotropic heating of the cloud reduces the ablation rate by a factor ~ 2 (except for the MHD computations presented in [54], where the corresponding reduction factor is only ~ 0.8 for purely hydrodynamic models).

(ii) One of the main approximations of first generation models was the replacement of the electron distribution function by an equivalent mono-energetic beam. This simplification has been removed in the models cited in the above paragraph, all of which include a more accurate description of the cloud heating by electrons (and/or ions) displaying a Maxwellian energy distribution. More precisely, the heat flux attenuation and local cloud heating is estimated from direct calculation of the evolution of (or moments of) the electron distribution function in [29, 50–52, 54] and from stopping length calculations in the models of Lengyel and collaborators [55, 56] and Pégourié and collaborators [24, 27, 28]. It is shown that an explicit account for the electron Maxwellian distribution increases the ablation rate by a factor ranging from ~ 3 to 5 (by a factor ranging from 2.3 to almost 10 if one includes the two simpler estimations of [22, 47]).

The presence of high-energy particles, generated by additional heating (beams or waves), is considered in two models [28, 51]. The first one is steady state, in the sense that the increment of electron and/or ion heat fluxes at the pellet surface immediately increases the ablation rate. This is not the case for the second, that takes into account the heating in volume of the ice by the high-energy electrons that cross the pellet from part to part (the threshold in energy is ~ 150 keV for a pellet of size ~ 1 mm), leading to its vaporization when the average energy per molecule deposited by the hot electrons is equal to the molecular sublimation energy. In what concerns hot ions, a detailed calculation of the geometrical effects due to the large dimensions of their orbit is included in the model, showing that their contribution to the ablation is weak, except for those whose orbit characteristics are such that they can penetrate the cloud by its lateral face and reach the pellet. Model predictions were compared with measurements for a limited number of experiments in plasmas with significant additional power (ion cyclotron resonance heating—IRH and lower hybrid current drive—LHCD), showing reasonable agreement [28]. Projections for reactor grade plasmas show that no significant over-ablation due to the fusion-born α particles is expected.

The role of the atomic physics processes is considered assuming local thermodynamic equilibrium in [29, 50, 52] and from finite rate calculations taking into account collisional and radiative ionization and recombination in [55, 56]. Quantitatively, it is found that to include these effects in the computation reduces the ablation rate by 25–30 %. The consequences on the dynamics of the cloud expansion are detailed in [29, 52] showing that, in the hydrodynamic approximation, the energy sink due to ionization is the cause of a shock front in the flow (this is not the case for dissociation because the latter is completed in the subsonic part of the cloud). In this case, the flow exhibits two sonic radii, the first upstream, the second downstream the ionization front.

A simple picture of the way the perpendicular expansion of the cloud is stopped by the $j \times B$ force once the ablatant is ionized can be found in [57]. It is illustrated in figure 7: as long as it is neutral, the ablation cloud, which expands at velocity v_0 , follows the pellet and moves across the plasma with velocity v_p . When the ablatant is hot enough to be partially ionized, it experiences the Lorentz force $F_L = e \cdot (v_p + v_0) \times B$, where e is the elementary charge. The latter can be split into two terms, F_p and F_0 , depending on the velocity component. The first one leads to a drift velocity $(F_p/e \times B)/B^2 = -v_p$, which stops the ablatant motion across the plasma (this point is discussed deeper in section 3). The second, $(F_0/e \times B)/B^2 = -v_0$, stops the transverse motion of the ablatant. As a consequence, the cloud expansion becomes essentially parallel. The first quantitative estimations of the transverse size of the cloud r_0 (of

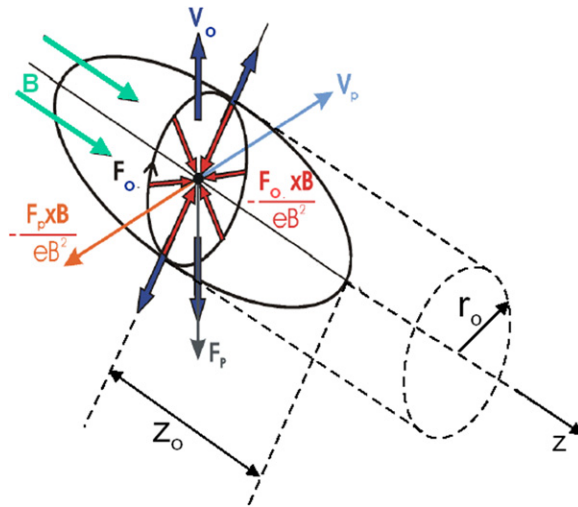


Figure 7. Schematic view of the cigar-shaped ablation cloud (of radius r_0 and half-length z_0) showing the different velocities and forces responsible for the full stop of the ablatant motion (see the text for more details). The green and light-blue arrows indicate the directions of the magnetic field and pellet motion, respectively.

the order of the ionization length of the ablatant) were calculated in [58, 59], using either a time-dependent one-cell Lagrangian model accounting for the $j \times B$ force only in average, or a steady-state calculation of the flow geometry near the stagnation plane in the case of an isothermal ablatant. The first determination is used in the ablation models [27, 28] with a different assumption on what concerns the residence time of the pellet inside the ablation cloud. In [28], as explained above, the ablatant is assumed to be frozen in the magnetic field as soon as it is ionized, leading to a parallel dimension of the cloud $z_0 \sim r_0 \cdot v_0/v_p$. In [27], the drift of the ablatant in the inhomogeneous magnetic field is taken into account (see section 3.1.3). In this case, once ionized, the deposited material experiences an acceleration $\propto T_0/R$ down the magnetic field gradient, where R is the tokamak major radius. It follows that the time required for it to drift over a distance r_0 is $\sim (r_0 \cdot R/T_0)^{1/2}$, corresponding to $z_0 \sim v_0 \cdot (r_0 \cdot R/T_0)^{1/2}$, i.e. $z_0 \sim (r_0 \cdot R)^{1/2}$ if one takes into account the fact that the parallel expansion of the cloud is nearly sonic. Although these two determinations of z_0 can be significantly different, the penetrations calculated by the two models for Maxwellian plasmas are almost identical, demonstrating that the additional shielding due to the ionized part of the cloud does not play a crucial role in the determination of the ablation rate. In [55, 56], the spatial distribution of ionization—and thus of the conductivity—is fully taken into account. The difference is that the dynamics of the neutrals and ions are calculated separately in [56]—with a collisional coupling between both populations—when only one fluid with weighted properties is considered in [55]. The calculated value of r_0 differs according to the approximations made in the calculation of the $j \times B$ force. The smallest value is obtained in the spatially resolved, one-fluid calculation, where a narrow layer at the cloud periphery ionizes rapidly, stopping its cross-field expansion [55]. The two other calculations yield larger values of r_0 , because the neutrals—that are not sensitive to the $j \times B$ force—continue to expand and drag collisionally the ions in the two-fluids approximation [56], and because ionization needs more time when averaged cloud properties are used [27, 28]. In [54], the change of the flow geometry owing to the $j \times B$ force is calculated in the MHD electrostatic approximation, i.e. under the assumption that the cloud β remains weak enough for the magnetic field to be uniform and constant outside

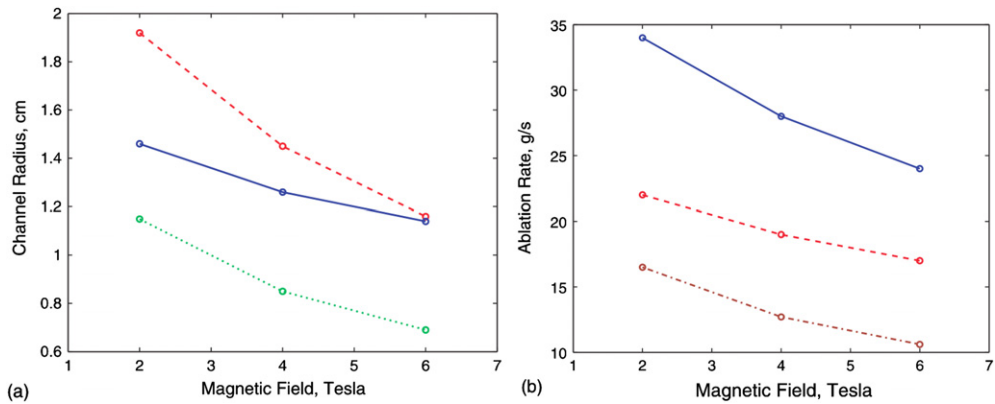


Figure 8. (a) Cloud radius r_0 as a function of the magnetic field strength. In all cases, the background plasma temperature and density are $T_\infty = 2 \text{ keV}$ and $n_\infty = 10^{20} \text{ m}^{-3}$, respectively and the pellet radius is $r_p = 2 \text{ mm}$. The blue-solid line is for a $10 \mu\text{s}$ warm-up time, the red-dashed line for a $10 \mu\text{s}$ warm-up time with electrostatic shielding and the green-dotted line for a $5 \mu\text{s}$ warm-up time. (b) Ablation rate as a function of the magnetic field. The blue-solid and red-dashed curves have the same parameters as the corresponding ones in (a), the dash-dotted curve is obtained with a $5 \mu\text{s}$ warm-up time with electrostatic shielding included [54].

as well as inside the ablation channel. If the calculated densities and temperatures in the ionized part of the cloud are in global agreement with previous estimations [27, 28, 55, 56], a new feature is the finding that the cloud radius r_0 depends on the rise time of the heat flux seen by the pellet. Shorter ‘warm-up’ times lead to narrower ablation channels, stronger shielding and reduced ablation rates, as displayed in figure 8. If, for present day tokamaks, the predictions of these different models are similar in terms of ablation rate or pellet penetration, they can differ significantly for reactor grade conditions, where a strong diamagnetism of the cloud [55] or high heating rates [54] are predicted to lead to smaller ablation rates. In what concerns the dynamics of the cross-field deceleration, the two-fluids and MHD electrostatic calculations [54, 56] show a slowing down of the flow without shock front, contrary to what is seen in the one-fluid, isothermal approximation [59].

(iii) In the early calculations of the electric potential of the ablation cloud, the latter was assumed to be at a zero temperature and only a single sheath was considered at the plasma–cloud interface [60]. Since that time, the calculation was improved by taking into account the return flux of electrons towards the plasma in the case of finite cloud temperature, with a detailed description of the double-sheath that develops in such conditions [61]. The corresponding electrostatic shielding is taken into account in the ablation models [27, 51] in the single sheath approximation, and considering the double-layer structure and possible shine-through of energetic particles that can cross the cloud without being stopped in [28]. A further step has been done in [55, 56], where the potential distribution is calculated in a self-consistent way in the whole volume of the ablation cloud. Quantitatively, the ablation rate changes by a factor of ~ 2 depending on whether electrostatic shielding is taken into account or not.

(iv) The approximation of a steady-state cloud has been partially removed in a number of works, but no complete pellet ablation with realistic plasma profiles has yet been computed in this way. In [55], and under the assumption that the pellet exits periodically from its ablation cloud, a ‘naked’ pellet is sequentially displaced at a discrete number of radial positions along its path. At each position, the instantaneous ablation rate is calculated as a function of the cloud development, decreasing rapidly with the increase in the cloud opacity. The average value over the first $10 \mu\text{s}$ of residence of the pellet inside the cloud is used as the effective

ablation rate, i.e. to calculate the pellet radius regression rate. In [29, 50, 52], the regression of the pellet radius is effectively taken into account in the calculation of the cloud expansion, but the incident heat flux is assumed to be constant. Finally, in [29, 52], it is shown that as long as the stress due to the inhomogeneous pressure distribution at the pellet surface is too weak to flatten it, the cloud expansion becomes rapidly steady state, which validates this approximation for present day experiments.

In what concerns more specifically impurity pellets, the original model of Parks, Leffler and Fisher [62], which was based on a simplified NGS calculation, was revisited in [45] with a much more detailed description of both the inner part of the cloud and solid–vapour phase transition at the pellet–cloud interface. Two descriptions are proposed for the latter: the first one is hydrodynamic, in which the vaporization front is considered to be analogous to a shock, and the second treats kinetically the thin Knudsen layer at the interface. Both descriptions are in close agreement and predictions of the more accurate ablation model fully confirm the results of the previous version. Finally, the Lengyel’s ablation model [55] was adapted to impurity pellets [63, 64]. The latter includes a spatially resolved determination of the potential distribution in the ablation cloud (i.e. taking into account the ionization state of the ions, see [61]) and a calculation of the collisional losses of the incident energy carriers on the electrons, ions and neutrals. Model predictions have been compared with experiments for pellets of both carbon and neon. When it is taken into account that the cloud is optically thick for the resonant lines, results show good agreement with measurements in what concerns both the cloud dimensions and pellet penetrations in Maxwellian plasmas [64]. Conversely, if the cloud is assumed to be optically thin at all wavelengths, its length is strongly over-estimated (by typically a factor of 10) [63], figure 9.

2.2.4. Ablation models—discussion As noted by several authors (see [25, 27, 29]), an intriguing question in ablation physics is the success of the NGS model in reproducing the experiments, when it is known that it considers only neutral gas dynamic shielding, and in an approximation that underestimates the effect of hot electrons (in a Maxwellian plasma, ablation is dominated by electrons of energy $(5\text{--}6) \times T_\infty$). Part of the answer can be found in the balance between the different additional mechanisms mentioned above. In most of the models presently available, it is found that if taking fully into account the Maxwellian distribution of electrons increases the ablation rate by a factor of ~ 4 , it is reduced by ~ 2 when one considers the non-uniform heat flux distribution at the pellet surface, by another factor of ~ 2 due to electrostatic shielding and by 25–30 % by the atomic physics, whose associated energy loss slows down the cloud expansion, and thus increases its shielding for a given ablation rate. In [54], somewhat different values are given for the contribution of the different mechanisms to the pellet shielding, but without changing their respective importance in the global picture.

More surprising is the fact that the change in the cloud expansion geometry—from spherical to purely parallel, as soon as the ionization degree reaches a few %—does not seem to be important in the total shielding, although it significantly increases the cloud line integrated density. An explanation is given in [65] in the case of hydrogen pellets, where estimates of the efficiency of neutral gas shielding and plasma shielding are compared, on the basis of a qualitative analysis of the main physical processes that govern the formation of the ablation cloud. The solution of this apparent paradox comes from the fact that—due to the low-sublimation energy of hydrogen—pellets are almost completely shielded, the consequence of which being that the cloud self-adapts to stop the most energetic electrons. Therefore, if the main part of the electron heat flux is effectively released in the ionized part of the cloud,

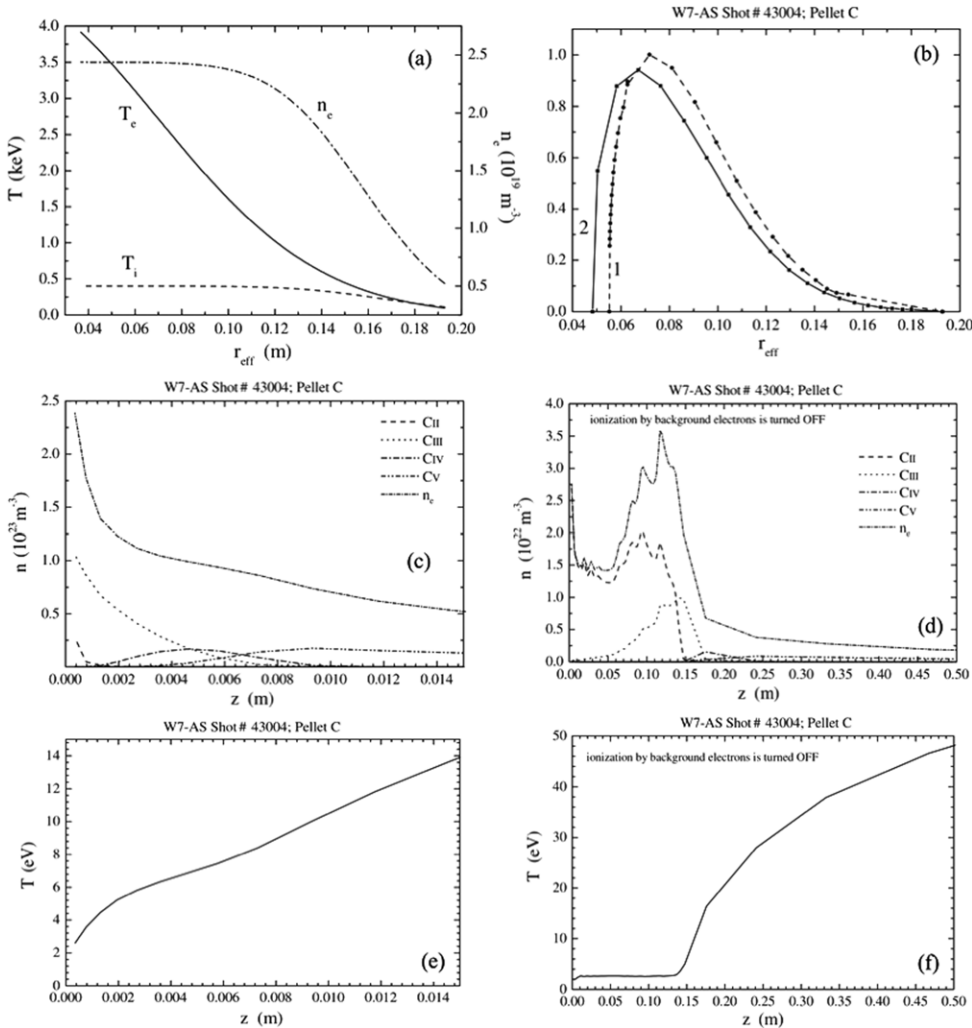


Figure 9. Effect of the opacity on the cloud structure. (a) Density and temperature profiles for W7-AS discharge #43004. (b) Ablation profile of C-pellet with (full line—2) and without (dashed line—1) opacity effect. (c) Parallel distribution of the ionization states with opacity effects. (d) Identical to (c) without opacity effect. (e) Longitudinal temperature profile with opacity effect. (f) Identical to (e) without opacity effect. Note the much shorter cloud length and absence of temperature plateau in the case where the cloud opacity is taken into account [64].

electrons of higher energy are only weakly affected by its crossing and are essentially stopped in the neutral region, close to the pellet surface. It follows that the ablation rate does not depend very much on the plasma shielding whose consideration—or not—changes only its value by a factor of ~ 2 . One must note that this analysis is in agreement with the fact that the two ablation models [27, 28], that differ by their estimation of the length of the plasma–cloud, predict very similar ablation rates, and by the fact that in RFPs, where the plasma–cloud is almost absent, the ablation rate is increased by a factor of ~ 2 – 2.5 [22]. However, a more complex picture is given in [54], where it is shown that the faster the heating rate during the cloud formation, the smaller the cloud radius r_o and thus the stronger the plasma shielding, leading possibly to a significant reduction of the ablation rate.

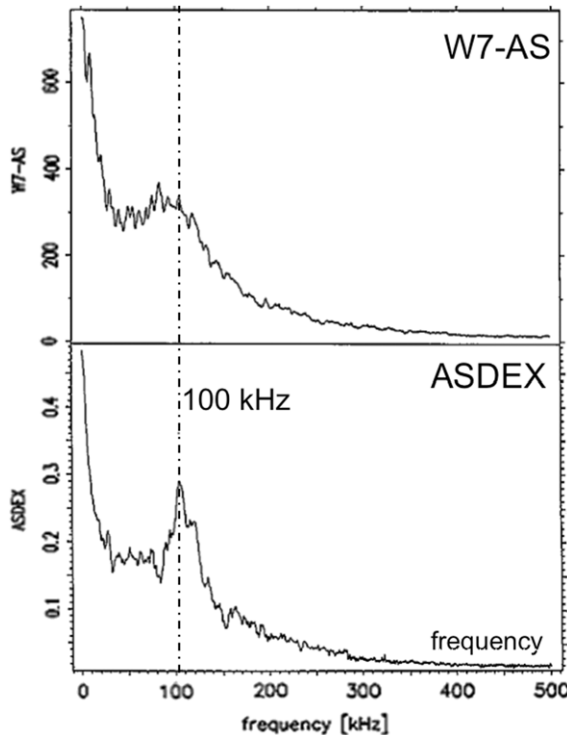


Figure 10. Mean frequency power spectra, a superposition of single FFT calculations. The upper spectrum is taken from W7-AS as a superposition of 53 single spectra, the lower from ASDEX as a superposition of 31 single spectra. The x-axis gives the frequency in kHz, the y-axis is in arbitrary units [70].

In spite of its simplicity, the NGS model can be used to estimate the ablation rate of pellets over a wide range of pellet and background plasma parameters. However, it is inapplicable for calculating the parameters of the emitting part of the cloud (especially its temperature), whose determination requires the use of more elaborated models (e.g. [27, 54, 55, 57, 66]).

Although all the models presently available predict ablation rates in agreement with the NGS scaling for the parameters of present day tokamaks, within a factor of $\sim 1.5\text{--}2$, they differ in their extrapolation to reactor grade conditions. Ablation models [27, 51] predict ablation rates higher by a factor of 1.5–3. In [29], it is shown that the warping of the pellet by the non-uniform pressure distribution at its surface can divide its penetration by a factor as large as ~ 3 . Conversely, in [55], penetration depths substantially larger than those obtained with the standard NGS ablation models are calculated owing to magnetic shielding effects. Also, it is pointed out in [54] that, owing to the dependence of the cloud radius on the heating rate, pellets traversing strong plasma gradients—as the pedestal region of reactor grade plasmas—could have significantly lower ablation rates if injected at high velocity. The last thing to be taken into account in the estimation of ablation rates in reactor grade plasmas is the pellet isotopic composition. Indeed, the average mass number of the ablatant being larger for DT or T₂ pellets than for pure D₂ or H₂ pellets, the cloud expansion is slower for the former, and thus the shielding is more efficient. This could lead to a relative increase in the penetrations by 25–30% for DT pellets with respect to that calculated for pure H₂ pellets, everything else being equal [67, 68].

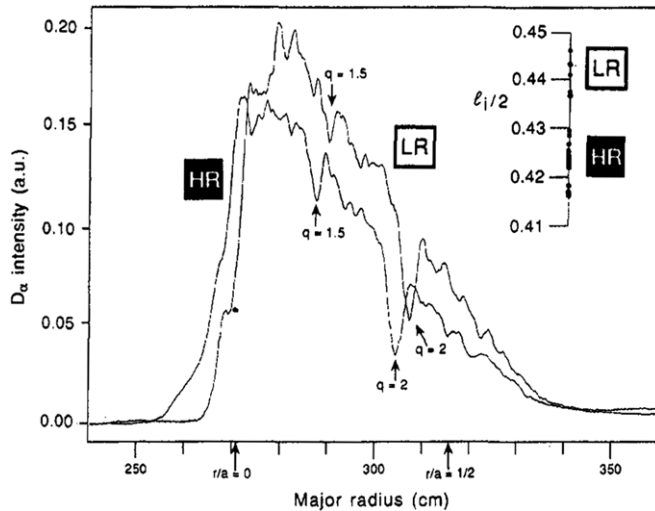


Figure 11. Averaged D_α traces of pellets injected in TFTR in two series of discharges characterized by different internal inductances: the high-recycling (HR) series, with $\sim 0.42\text{--}0.43$, and the low recycling (LR) series, with $\sim 0.44\text{--}0.45$. The outward displacements of the $q = 2$ and $q = 1.5$ surfaces are seen in going from the HR to the LR series, consistently with the increased internal inductance of the LR series with respect to that of the HR series [73].

2.3. Striations

2.3.1. Striations characteristics. Photographs or CCD pictures of ablation clouds display an alternation of dark and light-field aligned structures: the striations. The latter are clearly marked in the central region of the pellet trajectory, and are smoother or absent at its beginning and end [69]. In ASDEX-U, it was shown from spectroscopic measurements of the ablation cloud of D_2 pellets that striations are due to the pulsation of the cloud density ($\delta n_0/n_0 \sim 50\%$), with negligible variation of its temperature [16, 17]. As a whole, in tokamaks, they show no systematic correlation with rational values of the safety factor (q) and they exhibit the same spectrum in tokamaks and stellarators (namely, ASDEX and W7-AS, as shown in figure 10 [70]), demonstrating no strong link with the q -profile. However, they are almost systematically observed when a pellet crosses the $q = 1$ surface [71, 72] and it was demonstrated in TFTR that they are present for integer and half-integer q -values [73], see figure 11. The variation of their frequency with the pellet and plasma parameters was studied in three different machines: HT-1M, W7-AS and TEXTOR-94 by injection of micro-pellets of aluminium [74]. From the analysis of the observations, it follows that the fluctuation frequency does not depend on the velocity of the pellet, showing that the phenomenon responsible for the striation is governed by a characteristic time and not by a characteristic length. In fact, the variation of the mean fluctuation frequency for the three machines is better correlated with combinations of the electron temperature, electron density and magnetic field (B), like T_∞/B and $n_\infty \cdot T_\infty^{3/2}$.

2.3.2. Striations models A first interpretation of striations is that energy reservoirs of alternating low and high capacities represented by flux tubes located at rational and irrational magnetic flux surfaces are the cause of striations in the ablatant cloud. Following this model, the irreproducibility in the spectrum of striations exhibited by successive pellets injected into the same discharge is explained by the fact that a striation can exist only if a magnetic island or

a q -plateau is present [75]. This interpretation is supported by the fact that proper averaging shows that striations are present on integer and half-integer q -surfaces and that they follow them when the q -profile is modified [73], as shown in figure 11. As a consequence, the model was extended in an attempt to explain the observation of irregular striations as due to pre-existing electric and/or magnetic field perturbations [76] and to use their spectrum to determine the q -profile [77]. Despite some success (see e.g. [78]), this method of identification has not been validated and is now abandoned. One of the main reasons is that the similar characteristics of striations in both stellarators and tokamaks [70, 74] demonstrate that there is at least another phenomenon at work and that one cannot therefore link univocally a striation to a rational value of the safety factor.

The second mechanism originates in the relative motion of the ionized part of the ablation cloud with respect to the pellet, due either to the drift of the ionized material down the magnetic field gradient, or to the $E_r \times B$ rotation of the plasma. Due to this motion, the pellet periodically leaves its shielding cloud to build a new one, each exit of the pellet out of its cloud corresponding to a burst in the ablation rate [14, 17, 79]. Up to now, there has been no attempt to compare in detail calculations and experiments.

The last model, whose predictions reproduce the main dependence of the striation frequency with plasma parameters, is based on the Rayleigh–Taylor instability [80]. The latter is driven by the $E \times B$ rotation of the ablation column about its symmetry axis parallel to B . The radial E field comes from the radial variation of the cloud negative potential (see section 2.2.1), that results from attenuation of the field-aligned hot plasma electrons streaming through the inhomogeneous ablation cloud density. Indeed, due to the decreasing density in both the parallel and cross-field directions, the longitudinal opacity of the ablation cloud to incident electrons decreases radially. The absorption of incident electrons is higher near the axis of the cloud than at its periphery, causing a charge imbalance and a radial variation in the electrostatic potential within the cloud. The fact that the cloud pressure gradient and centrifugal force associated with the above rotation point in the opposite direction is the cause of the amplification of any outwardly directed displacement of the core of the cloud, leading to periodic ejection of cloudlets (in any cross-field direction), and thus to a quasi-periodic modulation of the ablation rate. This model reproduces many features of experimental striations: the calculated frequency ranges in the experimental values and is shown to depend on T_∞/B , but not on v_p , in agreement with the statistical analysis of [74]. The onset of the instability is predicted to occur when a threshold rotation frequency (or T_∞) is reached, in agreement with the fact that striations are generally not observed at the beginning of ablation and that their amplitude increases with pellet penetration [69]. Also, the observation of vertically displaced (randomly up or down) or curved striations in hydrogen (in TFTR and Tore Supra) or lithium pellet (in ALCATOR C-Mod) injection experiments support this interpretation [76, 81].

3. Homogenization of the pellet material

3.1. Measurements

Several phenomena take place between the time when the pellet deposits its material along its path and that when new axisymmetric temperature and density profiles are recovered in the discharge. They are as follows:

- (i) The parallel expansion of the deposited material along the field lines, until complete pressure homogenization with the surrounding plasma.
- (ii) The simultaneous modification of the potential distribution in the plasma, and thus of the poloidal rotation profile.

- (iii) The drift of this same material down the magnetic field gradient. In tokamaks, this drift expels the deposited matter out of the discharge in the case of low-field side (LFS) deposition, but favours its penetration when it is deposited on the high-field side (HFS).

3.1.1. Parallel expansion. The parallel expansion velocity of the deposited material was measured in TFTR from the analysis of the dynamics of the density increase at the plasma edge after the injection of a pellet, or of fragments of pellets [82]. Two diagnostics were used: an x-ray camera and a FIR interferometer with a time resolution of $\sim 10\ \mu\text{s}$, showing two density peaks propagating symmetrically along the field lines. In some cases, these structures last a distance longer than a toroidal turn, allowing the determination of their velocity from the time interval that separates two successive crossings of the plane of measurement. It is shown that the parallel velocity is $(1-2) \times 10^5\ \text{m s}^{-1}$ at the beginning of the homogenization phase and then slows down to $\sim 3 \times 10^4\ \text{m s}^{-1}$ after about $200\ \mu\text{s}$. Globally, it is measured that the whole homogenization process lasts less than $1\ \text{ms}$ [83]. In Tore Supra, the same conclusions were drawn from the modelling of the time behaviour of line integrated densities (time resolution of $16\ \mu\text{s}$) during the density rise consecutively to the injection of a pellet [84]. Similar observations were made in the stellarator LHD where, with hydrogen pellets, the redistribution phase of the pellet material was found to be globally adiabatic and to last $\sim 400\ \mu\text{s}$ [85].

3.1.2. Plasma potential modification. During and after the injection of a pellet, the plasma potential distribution is significantly affected. This was measured at the edge of HL-1M with a Langmuir probe array [86] and deeper in the plasma, beyond the radius of maximum pellet penetration, in JIPPT-IIU, with a heavy ion beam probe (HIBP) [19]. In the former case, it is observed that the edge potential becomes more negative at the moment of the pellet injection, and the corresponding modification of the plasma rotation is consistent with the poloidal deformation of the ablation cloud observed on the same machine [98]. Conversely, in JIPPT-IIU, the sign of the potential perturbation changes depending on whether the pellet is injected above or under the equatorial plane, which could indicate a link between the potential perturbation and the vertical drift of the pellet deposited electrons and ions in the inhomogeneous magnetic field [78, 87], figure 12.

3.1.3. Outward displacement and drift velocity. From an experimental point of view, the most obvious signature of the drift of the deposited material down the magnetic field gradient is the discrepancy between the measured increment of density and that expected by mapping the (calculated) ablation profile onto the flux surfaces. In tokamaks, this discrepancy consists essentially of a net outward displacement of the deposition profile for pellets injected from the LFS of the device [88, 89], when the matter penetrates significantly beyond the radius of maximum pellet penetration in the case of HFS injection [90], figure 13. The drift was directly measured: first in RTP, with an array of 16 optical fibres, on pellets injected from the LFS in ohmic and electron cyclotron resonance heated (ECRH) plasmas, yielding a value of $3.5 \times 10^3\text{--}10^4\ \text{m s}^{-1}$ for the drift velocity [91], figure 14. Then in ASDEX-U, with a dedicated diagnostic composed of two arrays of optical fibres, the first for LFS, the second for HFS-launched pellets. In both cases, the measured drift velocity was $(1-2) \times 10^4\ \text{m s}^{-1}$ and the corresponding acceleration $5 \times 10^8\text{--}10^9\ \text{m s}^{-2}$ [16, 17]. As for the magnitude of the displacement, it depends on the pellet and plasma characteristics, and particularly on the β of the latter: in JT60-U, in vertical high field side (VHFS) injection, no drift is observed when the pellets are injected in ohmic plasmas, probably due to their low temperature. Conversely, significant displacement is observed in NBI plasmas [92]. In FTU, no significant drift is

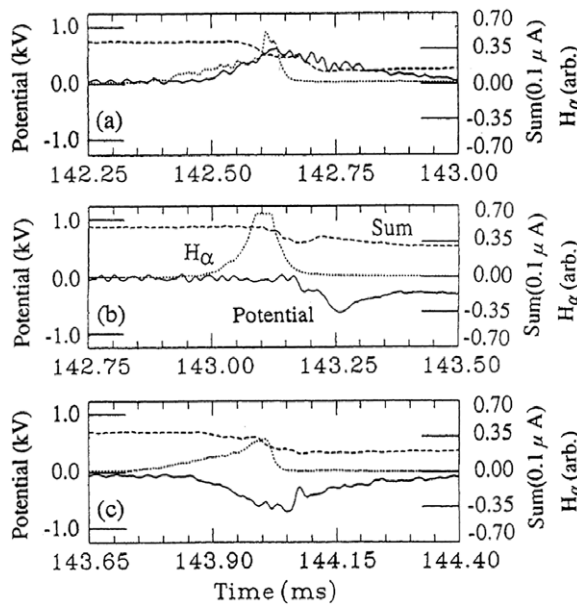


Figure 12. Change of plasma potential measured by HIBP in JIPPT-IIU. Plasma potential (solid line), sum of the currents collected on the upper and lower detectors (dashed line) and H_α light as a monitor of a pellet ablation (dotted line): (a) off-axis downward injection, (b) horizontal (on-axis) injection and (c) off-axis upward injection [87].

observed in ohmic plasmas (displacement $\leqslant 3\text{--}4\text{ cm}$), whatever the injection geometry, LFS or VHFS [93–95]. Finally, in JET, the initial matter deposition profile required to fit the post-pellet density behaviour shows only a small or even no displacement with respect to the ablation profile when the pellets are ablated in the outer part of the plasma [96]. Conversely, in ELMMy H-mode plasmas, a better matter penetration is observed when the pellets are injected from the HFS than from the LFS [97].

Another consequence of the presence of such a drift is the acceleration of the pellet in the direction of the plasma major radius, with typical value $\sim 5 \times 10^5 \text{ m s}^{-2}$ [17, 98], figure 15. It could be due either to a rocket effect associated with a front-back asymmetry of the ablation at the pellet surface, the front face (back face) of the pellet being over-shielded by the drifting part of the cloud in the case of HFS (LFS) injection [17], and/or to the drag force between the drifting material and the pellet surrounded by its neutral cloud [99].

In stellarators, the interpretation of the measurements is more difficult due to the complexity of the magnetic configuration and averaging effects. In LHD, several configurations of injection were tried with hydrogen pellets, showing that the drift of the deposited material is globally aligned down the magnetic field gradient—as in tokamaks [33], figure 16. However, owing to helical ripples and large rotational transform, both the magnetic field and ∇B vary drastically within a short space, making difficult the analysis of the measurements and the determination of the best location for pellet injection [32]. In addition, other phenomena can be at work simultaneously, blurring out the simple picture of the deposited material drifting down the magnetic field gradient. For example, during carbon pellet injection experiments in W7-AS, a low-velocity inward drift was observed, attributed to the drag of the pellet material by a flow present in the background plasma [100].

Finally, in the RFX reversed field pinch, no displacement of the ablated material is required to reproduce the time-history of the density profile during and after the injection of a pellet [22].

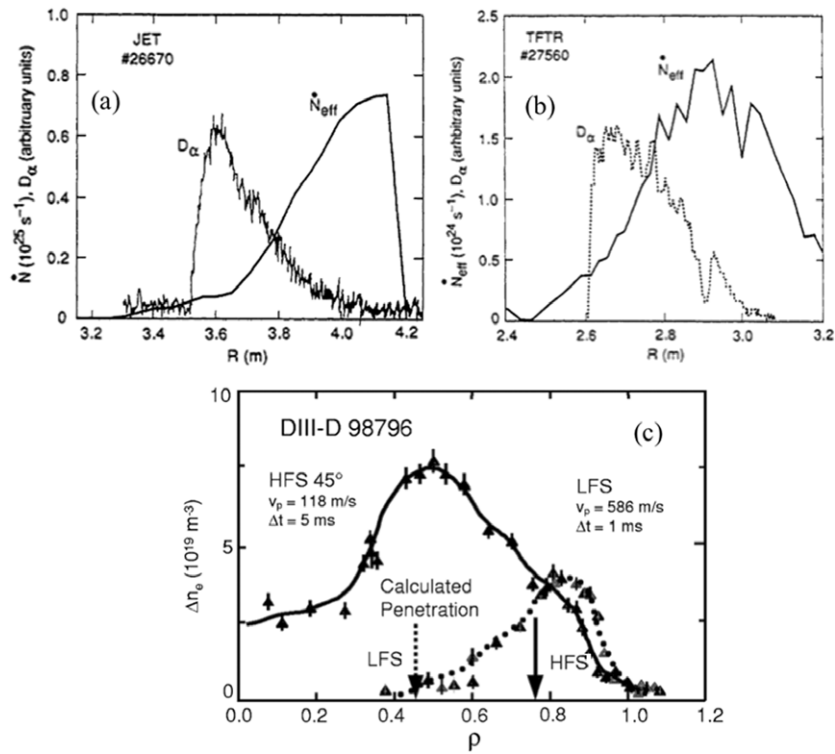


Figure 13. (a) LFS injection. D_α emission and effective deposition profile for a $r_p = 2$ mm D-pellet injected from the LFS in a steady-state JET H-mode plasma (9 MW NBI, $T_e(0) = 3.1$ keV), (b) same as (a) for a $r_p = 1.5$ mm pellet injected from the LFS in a TFTR ohmic plasma, (c) comparison between the effective deposition profiles for two $r_p = 1.35$ mm pellets injected in the same ELMY H-mode discharge in DIII-D, the first one from the HFS 45° , the second from the LFS outside midplane. The calculated penetration depths for these pellets are shown as vertical arrows [88, 90].

3.2. Homogenization models

3.2.1. Parallel expansion and potential perturbation. Three models were developed to calculate the parallel expansion of the pellet deposited material. Two of them are 1D, and consider as boundary conditions the density and temperature in the unperturbed plasma, the last is 0D but takes into account the change in the plasma characteristics due to the plasma compression and the heat transfer to the expanding cloud. The first one, developed by Parks and collaborators, is a Lagrangian model, 1D in the parallel direction, in which the heating of the cloud is based on a kinetic calculation of the energy deposition by incident electrons [101]. It shows a rapid pressure equilibration between the cloud and the plasma (of the order of $100 \mu\text{s}$), much faster than the temperature equilibration. For the end of the homogenization phase (that lasts ~ 1 ms), the cloud goes through a series of quasi-equilibrium states, the increase in temperature being balanced by the dilution of the cloud material due to its parallel expansion. In the Rozhansky's model [102], the cloud heating is described by non-local conductivity [103], and different regimes are obtained as a function of the plasma temperature (which is correlated with the magnitude of the ablation rate). For medium values, typical of present day tokamaks, the cloud heating is fast enough for the electron temperature to homogenize rapidly. In this

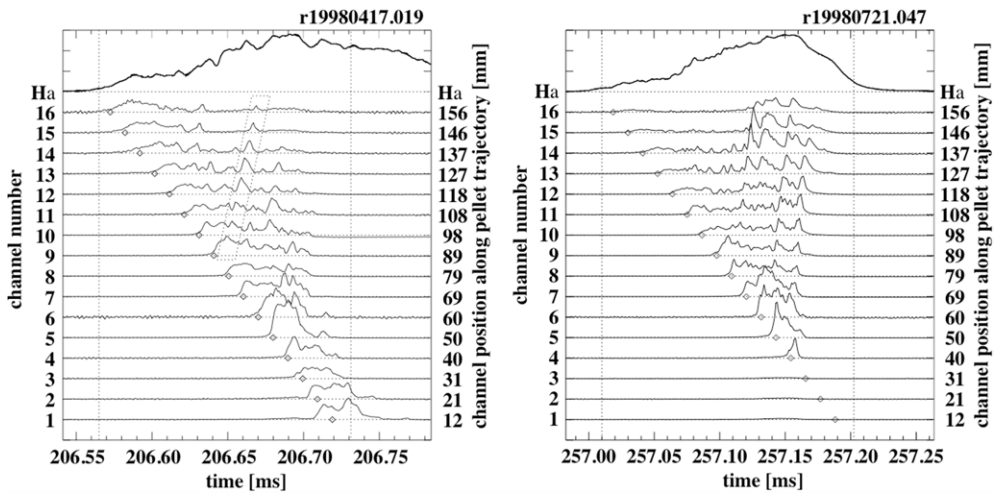


Figure 14. LFS injection. Two examples of the pellet ablation process as observed by the RTP fibre array. The diamonds indicate the expected passage times of the pellet using the measured pellet velocity and timing in the injector. The vertical dashed lines indicate the moments that the pellet passes the limiter radius and the plasma centre (if it would penetrate that far). The top trace is the wide angle H_α monitor. A clear peak is seen at the passage of the pellet at each channel. (left) Ohmic plasma: besides much broader peaks at all channels after passage of the pellet also a substructure of peaks can be recognized that are correlated on separate channels. An example of this is highlighted by the over-plotted parallelogram. This sequence of correlated peaks shows the presence of a light source which moves faster than the pellet and in the opposite direction. The pellet and plasma parameters are $n_\infty(0) = 3.93 \times 10^{19} \text{ m}^{-3}$, $T_\infty(0) = 900 \text{ eV}$, $v_p = 986 \text{ m s}^{-1}$, $N_p = 2.03 \times 10^{19}$ atoms. (right) Same as (a) for a pellet injected in a centrally ECH-heated plasma. Clearly the secondary peaks have much higher amplitude on the outer channels than the primary pulse (channels 10–16). The pellet and plasma parameters are $n_\infty(0) = 5.23 \times 10^{19} \text{ m}^{-3}$, $T_\infty(0) = 1450 \text{ eV}$, $v_p = 852 \text{ m s}^{-1}$, $N_p = 2.03 \times 10^{19}$ atoms, ECH-power = 320 kW [91].

case, the expansion is supersonic (with respect to the ambient electron temperature). A shock is formed in front of the cloud, inside which the density is homogeneous. For such conditions, the time-history of the density at a given location reproduces qualitatively the peak structure observed in TFTR [82]. For higher ablation rates, the cloud heating is slower and the density profile remains more strongly peaked during the major part of the homogenization phase, figure 17. For reactor grade parameters, the cloud temperature remains colder than that of the surrounding plasma for a long time, and the expansion is subsonic except for the latest stages. Finally, Pégourié's calculation is based on a two-cells four-fluids Lagrangian model (the electrons and ions in the cloud and the plasma) [84], derived from the original Lengyel's calculation of [58]. It takes into account the compression of the plasma by the expanding cloud (each toroidal shell being assimilated to a box of finite dimension), the slowing down of the expansion by the viscosity forces that develop at the cloud–plasma interface, the increase in the cloud lateral surface by the magnetic shear and the increase in the system inertia due to the part of the plasma put in motion by the cloud expansion. Results show that, for Tore Supra typical parameters, the cloud expansion is first supersonic, then subsonic when the viscosity forces are at work, with values comparing well with TFTR measurements [82, 83].

A possible explanation of the plasma potential perturbation is that the temperature difference between the cloud and the background plasma vanishes more rapidly than the one in density. Then, for a given temperature, the electrons propagate much faster than ions and tend to leave the cloud, charging the latter positively and the plasma negatively [84]. At the

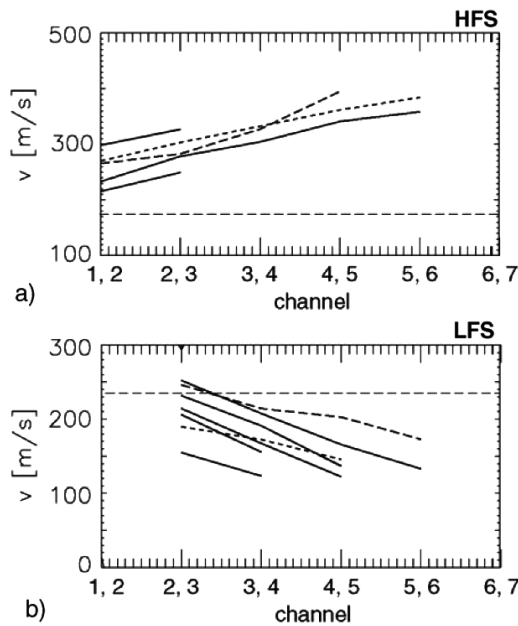


Figure 15. Pellet acceleration inside the plasma in ASDEX-U. Velocity trajectories determined from subsequent time of flight measurements for several pellets are shown, demonstrating that pellets are accelerated or decelerated depending on whether they are launched from the HFS or LFS of the tokamak. The broken horizontal lines show the nominal pellet velocities [17].

equilibrium, there results from this process a difference of potential $\Delta\Phi \sim 0.2\text{--}1\text{ kV}$ between the cloud and the surrounding plasma, in qualitative agreement with probe measurements in HL-1M [86]. However, this model is unable to reproduce the measurements in JIPPT-IIU [78, 87], where it was measured that the sign of the potential perturbation changed depending on whether the pellet is injected above or under the equatorial plane (according to [84], the potential perturbation is always negative). If such a perturbation $\Delta\Phi$ exists, it changes the radial electric field profile and thus the plasma poloidal rotation, dragging the pellet deposited material. Poloidal drifts of the ablation clouds of direction corresponding to that expected from the above process were observed in HL-1M and ASDEX-U [98, 104, 105]. In addition, in Tore Supra, such a rotation has been shown to be necessary to reproduce accurately the time-history of the line integrated density measurements during the injection of a pellet [84], and particularly the duration of the peaks of density, figure 18.

In the reversed field pinch RFX, the increase in the density during the injection of a pellet was analysed by means of a simple model emphasizing the link between the magnetic configuration and the dynamics of the homogenization [22]. In particular, it was shown that, owing to the strong transport and magnetic shear, the homogenization of the deposited material is faster than in tokamaks, without significant drifts. In addition, due to the fact that the winding of the field lines is essentially poloidal in the outer part of the discharge and toroidal in the core, axisymmetric density profiles are first recovered in the plasma core, the material deposited at the edge forming a high-density poloidal ring that decreases on a long time scale.

3.2.2. ∇B -induced drift If the models mentioned above can reproduce the dynamics of the density increase consecutively to the injection of a pellet, the predicted density profile disagrees

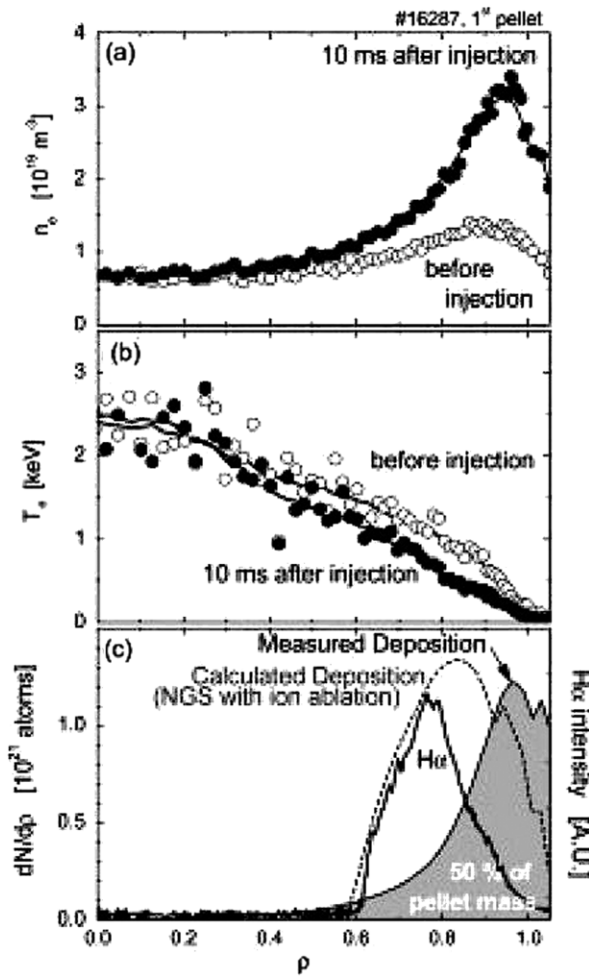


Figure 16. Radial profiles before and after pellet injection in LHD: (a) electron density, (b) electron temperature, (c) H_α intensity, which indicates penetration depth and calculated and measured deposition profiles [33].

generally with the measurements because the drift of the deposited material down the magnetic field gradient is not taken into account in these simulations. This drift originates in the vertical motion (in tokamaks) of the electrons and ions of the ionized cloud in the inhomogeneous magnetic field, giving rise to an uncompensated current $j_{\nabla B} = 2(p_\infty - p_0)/RB$ (which is non-zero since the cloud pressure p_0 is larger than that p_∞ in the plasma). Under open circuit conditions, which is the case at least at the beginning of the cloud expansion, this current is cancelled by an opposing ion polarization current, $j_{\text{pol}} = (n_0 m_i / B^2) dE/dt$, where m_i is the ion mass and E the electric field resulting from the charge separation due to $j_{\nabla B}$. At the equilibrium, dE/dt is determined from the condition of current closure, yielding for the cloud acceleration: $dv_d/dt = (dE/dt \times B)/B^2 = 2(p_\infty - p_0)/R n_0 m_i$ [106, 107]. As long as the cloud remains in a situation of open circuit, the potential perturbation (of the order of $\sim r_0 E$) propagates in the parallel direction at the Alfvén velocity, which lowers the cloud polarization and thus the drift velocity. Following this picture, the drift stops at the pressure equilibration.

Numerical MHD simulations were performed by Aiba and collaborators, in a simplified

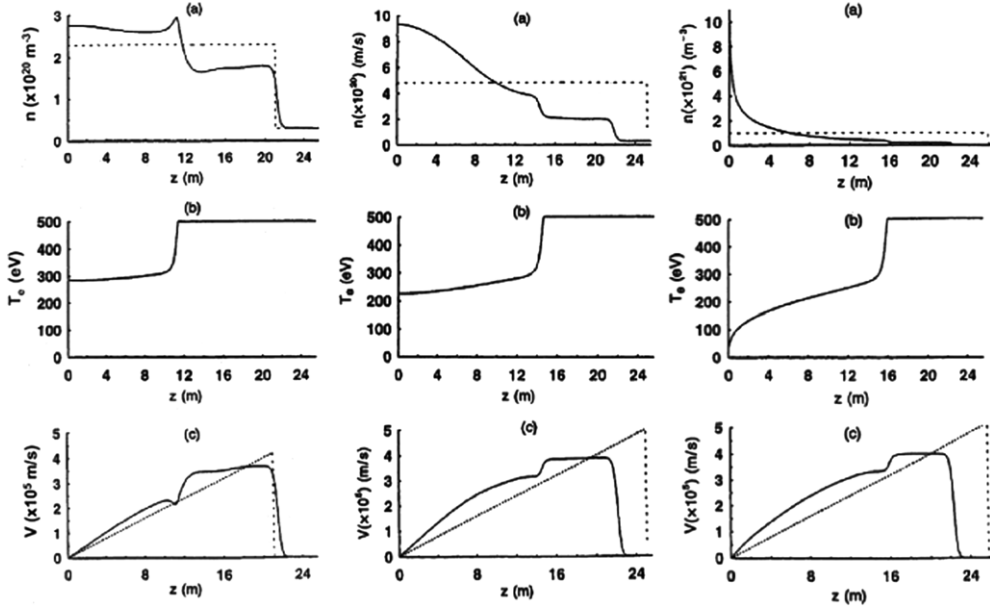


Figure 17. (left) Parallel distribution at $t = 50 \mu\text{s}$ for (a) the density, (b) the temperature and (c) the expansion velocity in a cloud of radius $r_0 = 2.5 \text{ cm}$, constituted by a particle source of intensity $dN_p/dt = 10^{23} \text{ s}^{-1}$, switched on during $\tau = 2.5 \mu\text{s}$, in a plasma of density $n_\infty = 3 \times 10^{19} \text{ m}^{-3}$ and temperature $T_\infty = 500 \text{ eV}$. The dotted lines are the corresponding self-similar solution. (middle) Same display for a moderate ablation rate $dN_p/dt = 2.5 \times 10^{23} \text{ s}^{-1}$. (right) Same display for a high-ablation rate $dN_p/dt = 5 \times 10^{23} \text{ s}^{-1}$ [102].

geometry and limited to the first phase of the drift [108], and by Strauss and Park, in a realistic 3D geometry and until the recovery of axisymmetric profiles in the discharge [109]. In this last study, the initial flux surface averaged pressure $\langle p(\psi) \rangle$ is that of a 2D equilibrium, upon which the pellet deposited cloud is simulated by a localized over-density of the order of $\delta n/n \sim 10-15$, the temperature being uniformly reduced on the perturbed flux surface to ensure that $\langle p(\psi) \rangle$ remains unchanged. If this last approximation is justified because the parallel thermal conduction time is much shorter than the time of density homogenization, it remains that the model cloud is considerably less localized and the density contrast much smaller than in experiments. Simulation results show that during the phase of density spreading, the cloud moves in the direction of the major radius of the torus. However, when the initial perturbation is localized on the LFS, the displacement is essentially reversible: the system tends to come back at its equilibrium position, defined by the flux surface averaged pressure $\langle p(\psi) \rangle$. Conversely, when the pressure perturbation is large enough and located on the HFS, the matter penetrates up to the magnetic axis and in the process drives magnetic reconnection to produce negative central shear. As a whole, the cloud displacement scales as $(\delta p/p) \cos \theta$, where θ defines the initial position of the pressure perturbation, and no significant drift is predicted in the case of vertical injection, see figure 19. The same authors studied pellet driven MHD instabilities with high-toroidal wavenumber ($n > 4$) [110, 111]. They show that instabilities are easier to excite when the pellet is injected from the LFS, because the cloud pressure perturbation tends to add to the background pressure drive. At the opposite, for HFS injection, the pressure perturbation opposes the background pressure drive and the instabilities are harder to excite. Also, they show that the instability can cause the fragmentation of cloud, leading to

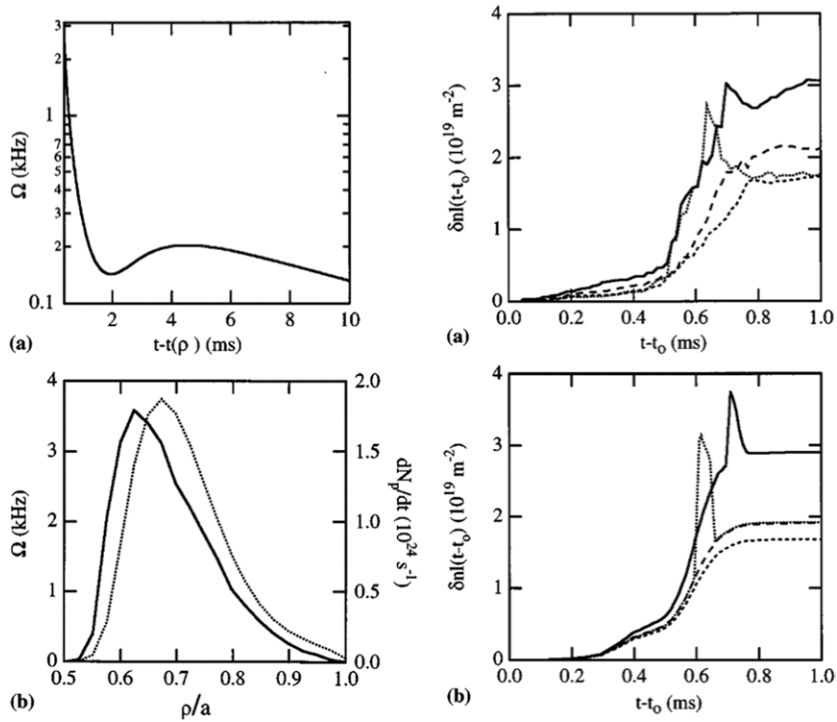


Figure 18. (left) Poloidal rotation induced by the negative perturbation of the plasma potential consecutively to the injection of a pellet. The poloidal frequency Ω is linked to the potential perturbation $\Delta\Phi$ by $\Omega = (\Delta\Phi \cdot N_p)/(2\pi(N_p + N_\infty \rho^2 B))$, where N_∞ is the particle content of the toroidal shell in which the cloud is deposited. (a) Time-history, (b) rotation profile. For comparison, the ablation rate dN_p/dt is also plotted (dotted line). (right) Time-history of the increase of the line integrated densities in the Tore Supra discharge TS3177. The pellet and plasma parameters are: $N_p = 8.6 \times 10^{19}$ atoms, $v_p = 600 \text{ m s}^{-1}$, $n_\infty(0) = 4.1 \times 10^{19} \text{ m}^{-3}$, $T_\infty(0) = 1850 \text{ eV}$, $B = 3.9 \text{ T}$. (a) Measurements, (b) simulations results, taking into account the pellet-induced poloidal rotation [84].

an anomalous penetration of the deposited matter (such a fast penetration of the pellet material was observed in DIII-D during fast plasma shutdown by injection of a killer-pellet [112]), see subsection 4.1.1.

Fuelling scenarios for several machines were analysed by Polevoi and Shimada [99], by means of a heuristic model combining scaling laws extracted from papers previously mentioned: the ablation rate from [51], the cross-field dimension of the cloud from [101] and the maximum ∇B -induced displacement from [109]. The model reproduces satisfactorily the displacements of the pellet deposited material measured in DIII-D (in the LFS and HFS-45° configurations, where the angle 45° defines the location of the injection point above the equatorial plane) and in ASDEX-U (in HFS injection), giving confidence in its predictions. However, the calculated deposition profile is systematically narrower than the measurements (which could be the signature of a transient increase in the post-pellet plasma transport) and no dissipation process is included to explain the irreversibility of the displacement (in the original paper [109] the cloud comes back at its almost initial position). First projections are presented for ITER-like conditions, showing a deposition profile peaking at midradius for a big pellet (50% of the plasma particle content) injected from the HFS at $v_p \sim 300 \text{ m s}^{-1}$. It is also shown

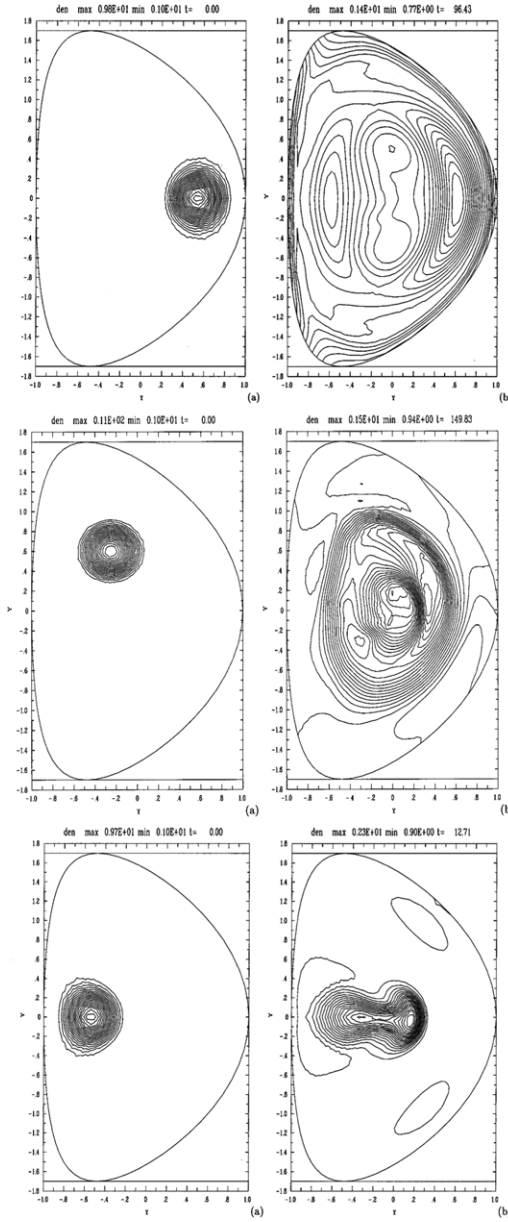


Figure 19. Poloidal contour-plot of the density in the plane of symmetry of the initial pressure perturbation. (top) LFS midplane deposition (a) $t/\tau_A(R/a) = 0$, where τ_A is the Alfvén time defined in terms of average magnetic field and background density, (b) $t/\tau_A(R/a) = 96$. (middle) Top deposition (a) $t/\tau_A(R/a) = 0$, (b) $t/\tau_A(R/a) = 150$. (bottom) HFS midplane deposition (a) $t/\tau_A(R/a) = 0$, (b) $t/\tau_A(R/a) = 12.7$ [109].

that larger displacements are expected in reversed shear configurations.

Several authors developed models taking into account more accurately the coupling between the cloud expansion and drift. Their common feature is that the drift velocity is determined for a part by the balance between (i) a leading term resulting from the compensation

of the curvature current $j_{\nabla B}$ by the polarization current j_{pol} and (ii) a braking term due to an Alfvén wave emission at both ends of the cloud (see, e.g. [101]). However, if this process only allows one to reproduce the acceleration and drift velocity at the beginning of the cloud homogenization, it also leads to calculated displacements significantly larger than those measured and supplementary phenomena must be added to reconcile code predictions with experiments. Although using different approaches, all the phenomena invoked up to now originate in the winding of the field lines around the major axis of the machine and specificity of the magnetic configuration. It must be noted here that these different phenomena are not exclusive to each other and can apply simultaneously.

First, Parks and Baylor [113] introduced two toric effects acting oppositely on the magnitude of the drift. The first originates in the parallel expansion of the cloud that enhances the curvature drift and thus the cloud polarization. The second is due to the shear-induced twist in the cloud cross-section that gradually changes the cloud boundary from a circle into a rotated ellipse when expanding in the parallel direction. This geometric distortion brings the space charge layers closer together as the cloud length increases, resulting in a differential poloidal drift of the cloud ends. Following the authors, this yields a loss of coherency by shifting the end parts of the cloud outside the influence of the electrostatic fields when the centre of those parts shifts by an amount $\sim 2r_0$ with respect to the cloud axis. Then, those fluid elements are unable to participate in the coherent drift motion and stop drifting with the rest of the cloud. Beginning with the outermost elements, they sequentially peel off one by one and—because of their small relative mass—get deposited in the plasma almost immediately. This dispersal of the cloud material, which fastens the homogenization process and thus limits the overall displacement, is shown to be necessary to obtain a quantitative agreement between simulations and experimental deposition profiles for both HFS and LFS-launched pellets in DIII-D. However, the way the differential drift mentioned above contributes or not to the global alignment of the cloud with the local magnetic field is not considered in the above model, which could limit its validity.

For Rozhansky and collaborators [114], the reduction of the cloud polarization is due to the compensation of the curvature and ∇B drifts along the cloud length as soon as the latter exceeds a critical length $L_c \approx \pi q R$. In this case, indeed, the projection of the cloud onto a poloidal plane covers more than half a turn and the same field line connects parts of the cloud of opposite polarization, which short-circuits $j_{\nabla B}$ and thus stops the drift. In its original form, this model predicted displacements typically 4 times larger than those observed in ASDEX-U. For this reason, and arguing that the $j_{\nabla B}$ compensation is essentially a 3D phenomenon, the same authors performed simulations in which L_c is considered a free parameter. For parameters typical of pellet injection experiments in ASDEX-U, a qualitative agreement between the simulated and measured displacements and post-pellet density profiles is obtained for $L_c \sim 2\pi R$ [66, 115], figure 20.

Finally, the finite size of the plasma is taken into account in the model developed by Pégourié and collaborators [116]. The latter is based on the fact that, due to the winding of the field lines around the torus, the different images of the potential distribution resulting from the cloud polarization overlap when propagating in the plasma. As a consequence, connections appear between the positively and negatively charged parts of the cloud, along which a parallel—resistive—current flows, reducing the cloud polarization and thus the drift velocity. In computing the increment of density and fuelling efficiency, the model also takes into account the recycling of the pellet material expelled out of the discharge. Model predictions were compared with measured fuelling efficiency and global displacement of the deposited material, showing reasonable agreement, figure 21. Also, when applied to FTU, this model was shown to reproduce reasonably the measured drift for both LFS and VHFS-launched

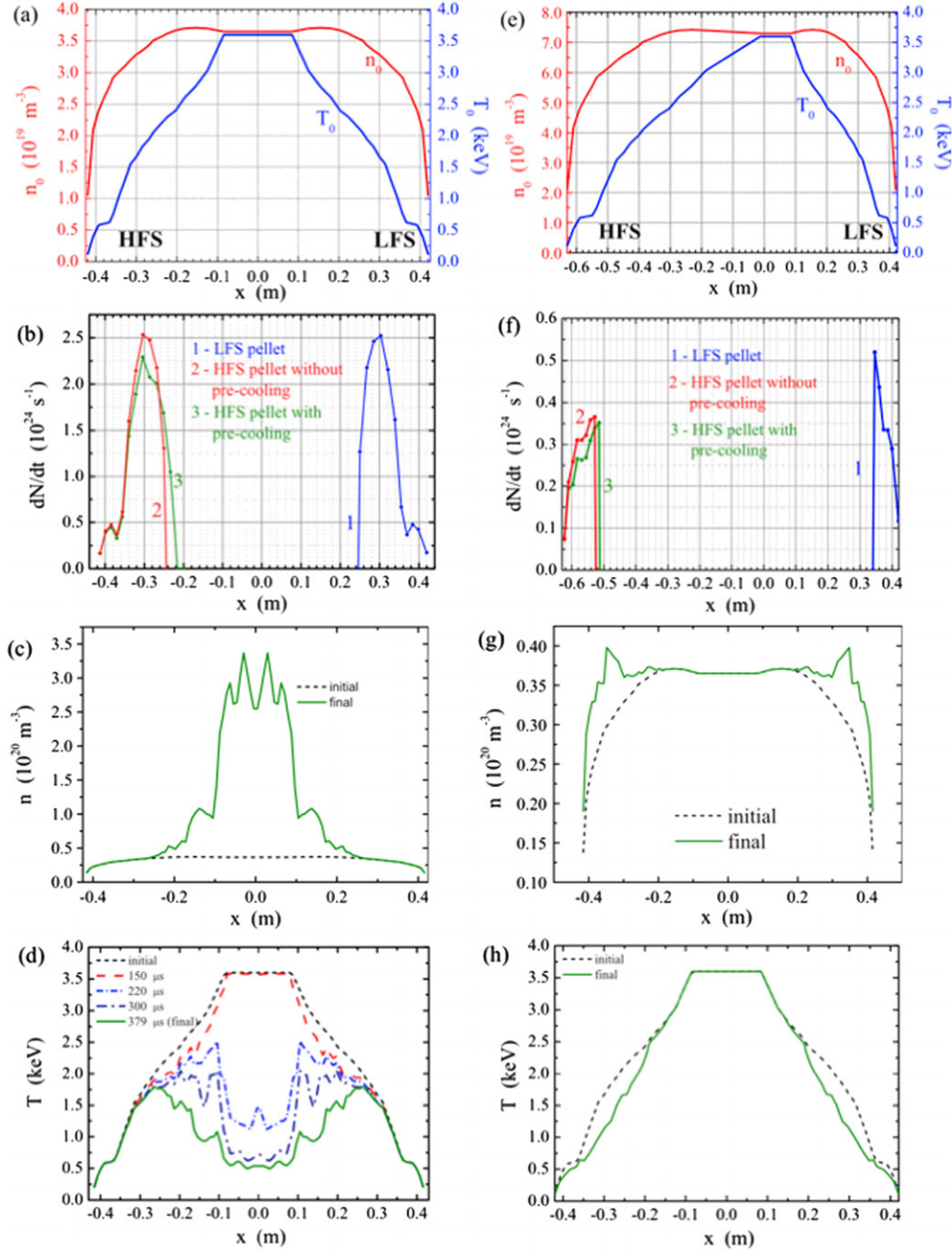


Figure 20. Simulations for typical ASDEX-U plasma and pellet parameters: $B = 2.5 \text{ T}$, $n_0 = 3.7 \times 10^{19} \text{ m}^{-3}$, $T_0 = 3.6 \text{ keV}$, $r_p = 1.2 \text{ mm}$, $v_p = 560 \text{ m s}^{-1}$. (left) HFS injection: (a) initial density and temperature profiles, (b) pellet ablation profile with (green line) and without (red and blue lines) pre-cooling, (c) density profile after the homogenization of the pellet material, (d) temperature profile at different times after the pellet injection. (right) (e–h) Identical to (a–d) in the case of LFS injection [115].

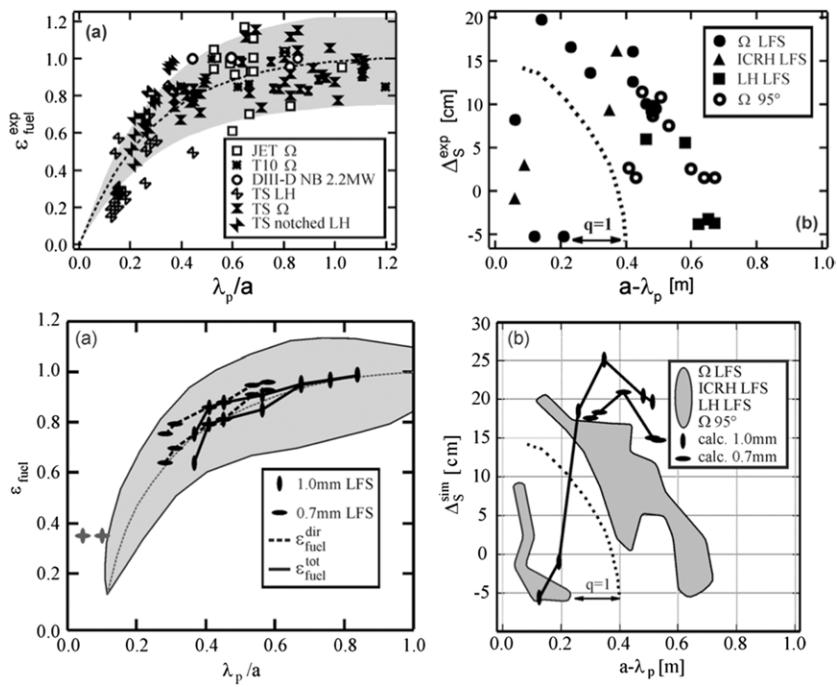


Figure 21. (Top) (a) LFS injection. Fuelling efficiency as a function of the pellet relative penetration for JET ohmic (open squares), T10 ohmic (diamonds), DIII-D 2 MW NBI (open circles), Tore Supra ohmic and LHCD (hourglasses, see the legend in the figure for details). (b) Mean displacement of the deposited material as a function of the radius of maximum pellet penetration for Tore Supra LFS (full symbols) and vertical injection (open symbols). (Bottom) Simulated counterparts of top figures: vertical bars are for a big pellet ($N_p = 2.5 \times 10^{20}$ atoms), horizontal bars for a small one ($N_p = 8.65 \times 10^{19}$ atoms), shadowed regions correspond to the location of the experimental points. (a) Direct fuelling efficiency (pellet source only, full line) and total fuelling efficiency (pellet + recycling sources, dashed line), (b) mean displacement [116].

pellets [95]. However, here also, the study of individual cases shows that the calculated deposition profile is generally narrower than the experimental density increment. As mentioned above, this could be the signature of a transient transport enhancement and could explain why the fuelling efficiency is always lower than 100% even for pellets launched from the HFS (in a configuration where the ∇B -induced drift would, in principle, only increase the penetration of the deposited material) [117, 118]. In what concerns the optimization of the injection geometry, computations show that the mean displacement is smaller for a VHFS than for a pure HFS injection configuration even if—in this last case—the pellet is launched at a lower velocity.

Up to now, there is no drift model taking into account the interaction between the ∇B -induced drift and the pellet-induced change in the plasma poloidal rotation (see [84]). Only the pre-cooling of the plasma by the deposited material drifting in front of the pellet in the case of HFS injection is estimated in [115], showing that—in the investigated range of pellet and plasma parameters—only a small increase in the pellet penetration can be attributed to this phenomenon. However, further work is needed to clarify this point since it was reported in [117] that shallow HFS-launched pellets could penetrate significantly deeper than what was expected from the NGS scaling. The solution of this apparent discrepancy can probably be found in the different pellet and plasma parameters characterizing the experiments reported in [117] and the simulations described in [115].

4. Fast plasma response

In addition to the modification of the plasma transport properties due to the peaking of the density profile, a pellet can trigger different types of instabilities, like snakes or ergodization of the plasma core when interacting with the $q = 1$ surface, edge localized modes (ELMs) when injected into H-mode discharges or non-local response of the plasma temperature.

4.1. MHD phenomena

4.1.1. Impact on MHD activity. On the whole, the injection of a pellet increases the MHD activity. In T10, big LFS-launched carbon pellets ($r_p > 1.5$ mm) penetrating beyond the magnetic axis trigger tearing processes on simple $q < 2$ resonant surfaces and a prompt $q = 1$ reconnection in the plasma centre [119]. In ASDEX-U, neoclassical tearing modes (NTMs) are triggered when the pellet itself reaches $q = 3/2$ in the case of LFS injection, and even for a shorter penetration in the HFS configuration because, in this latter case, the deposited material is transported up to the surface $q = 3/2$ by the ∇B -induced drift [16, 17]. In DIII-D, the injection of a killer-pellet triggers strong magnetic fluctuations ($\delta B/B \sim 0.2\%$) that are responsible for a rapid penetration of the deposited material into the plasma core [112]. From a theoretical point of view, 3D MHD simulations predict that ballooning like instabilities driven by the pressure perturbation can be destabilized by the injection of a pellet [110, 111], see section 3.2.2. But both injection geometries are not equivalent: LFS-launched pellets are more destabilizing because the pellet pressure perturbation and the background pressure drive tends to add, when they are opposed to each other in the HFS configuration. Despite this general behaviour, it was shown in T10 that both the large-scale MHD perturbations and high-frequency noise were stabilized by the shallow injection of a pellet of appropriate size, with a beneficial impact on the plasma thermal insulation [120].

4.1.2. Interaction of pellets with the $q = 1$ surface. A detailed study of the interaction of pellets with the $q = 1$ surface was done in FTU, showing the following phenomenology with increasing penetration. As long as the pellet approaches but remains outside the $q = 1$ radius, only a slowing down of the sawtooth activity is observed [93]. Conversely, as soon as it penetrates—even weakly—inside the $q = 1$ surface, it causes the rapid growth ($\sim 20\ \mu\text{s}$) of an $m = 1$ magnetic island that can survive several energy confinement times [121, 122], figure 22. As a consequence of the island evolution, the pellet material deposited in the annular region between the $q = 1$ radius (prior to pellet injection) and the Kadomtsev mixing radius is rapidly transported toward the plasma centre [123]. This advection is tantamount to an effective inward particle transport and is very sensitive to the pellet penetration depth because of the sharp slope of the density profile resulting from pellet ablation. It was observed for pellets launched from the LFS as well as from the VHFS (with an impact parameter $\rho/a \sim 0.5$). In this last case, it is the ∇B -induced drift of the material deposited close to the equatorial plane that is the cause of the growth of an $m = n = 1$ island and subsequent advection of the pellet material [94]. For a given magnetic field, this enhancement of the central fuelling increases with the plasma current, due to the higher density of the target plasma and larger inversion radius that increase the effects of $m = 1$ modes to take the density to the plasma centre.

Different scenarios were observed in RTP and Tore Supra, although showing also the rapid development of a magnetic island followed by an ergodization of the magnetic field in the plasma centre. In the former machine, it was shown that if ablation is a process globally adiabatic as long as the pellet remains outside the $q = 1$ surface, a rapid ($\sim 10\ \mu\text{s}$) collapse of the electron pressure is observed when it penetrates inside, figure 23. This collapse is interpreted

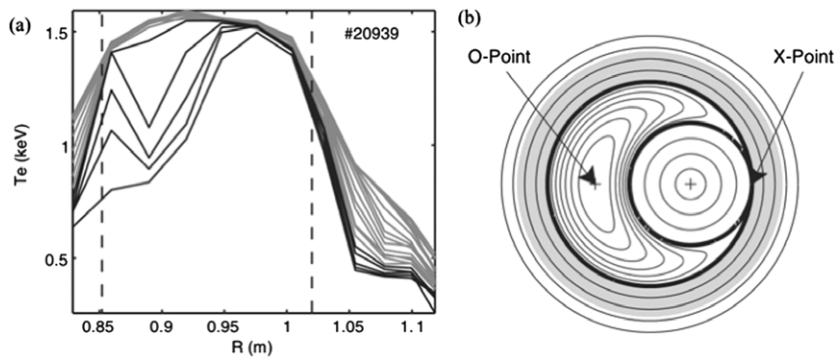


Figure 22. (a) Temperature profiles taken every $5\ \mu\text{s}$ during and just after pellet ablation in FTU pulse #20939. Grey lines correspond to the first $70\ \mu\text{s}$ after the beginning of significant pellet ablation (this is the time taken by the pellet to reach the $q = 1$ surface), black lines to the following $25\ \mu\text{s}$. The plasma centre lies at $R = 0.934\ \text{m}$. (b) Schematic diagram of the reconnection process: while the island is growing, the outer circle enlarges and the pellet deposition region surrounding the $q = 1$ surface is mixed with the island interior. The island O- and X-point are shown in the figure. The X-point is where the reconnection of the magnetic field lines takes place during the island growth. The separatrix is shown as a thick line [122].

as a transient ergodization of the field lines in the plasma centre, and is followed by a phase of restoration of the magnetic configuration that lasts $\sim 40\ \mu\text{s}$ [124, 125]. In Tore Supra, a pellet penetrating close to the plasma centre triggers systematically a sawtooth crash. If it is injected at the end of a sawtooth cycle (i.e. at a time close to that at which the next crash is expected), its trajectory can be significantly perturbed, exhibiting a toroidal deflection abruptly enhanced at the crossing of the $q = 1$ radius and reduced to almost nothing afterwards, figure 24. These features are interpreted as the signature of the rapid development of an $m = n = 1$ island whose evolution leads to a total reconnection in the plasma centre. Following this picture, the sharp deflection of the pellet trajectory at the crossing of the $q = 1$ surface would be due to the negative current singularity that develops at the island X-point and the absence of deflection in the plasma centre as the consequence of the loss of the most energetic electrons during the reconnection [37].

4.1.3. Snakes. The snake is a MHD phenomenon initially observed in JET on the $q = 1$ and $q = 3/2$ flux surfaces [126]. Its name comes from the aspect of the soft-x-ray emissivity reconstructed in a plane $\rho \times t$ or $R \times t$ (where ρ is the plasma minor radius and t the time), figure 25. Although spontaneous snakes were already observed, it appears in most cases on/inside the $q = 1$ flux surface after the nearly central injection of a pellet [78, 124, 127–130, 131]. It consists in a large perturbation ($25 \times 17\ \text{cm}^2$ in JET, $15 \times 15\ \text{cm}^2$ in Tore Supra) of larger density and lower temperature than the surrounding plasma, with typical values $\delta n/n \sim 25\text{--}140\%$ and $\delta T \sim 100\ \text{eV}$ [128, 130]. A snake lasts several confinement times and can survive several sawtooth crashes, but the temperature perturbation weakens more rapidly than that of density. It is observed to rotate poloidally with a frequency that increases continuously all along its lifetime, up to a few 100 Hz. At every sawtooth crash, both the snake radius and the rotation frequency decrease. This can lead to a reversal of the rotation direction at the beginning of the snake life and the variation of its radius can be as large as 30–50% [127, 128], figure 26. In Tore Supra, the soft-x-ray emissivity is observed to increase $\sim 100\ \text{ms}$ after the appearance of the snake, indicating an impurity accumulation, by a factor of up to 20–30 with respect to the surrounding plasma [128].

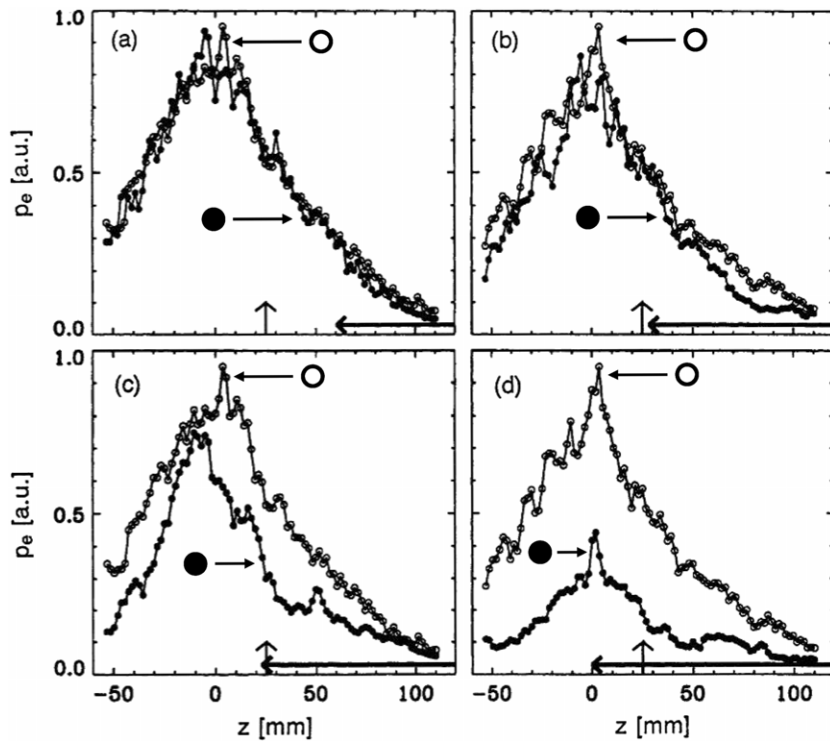


Figure 23. Electron pressure profiles measured during pellet ablation in four RTP discharges (closed symbols). For comparison a pre-pellet profile is plotted in each case (open symbols). The horizontal arrows indicate the region passed by the pellet, the vertical arrows indicate the sawtooth inversion radius that is ~ 2.5 cm for all discharges. The ablation process remains globally adiabatic as long as the pellet remains out of the $q = 1$ surface: (a) and (b), but the core electron pressure collapses as soon as it penetrates inside: (c) and (d) [125].

A model was presented [132] in which the formation of the snake is attributed to the growth of a magnetic island driven by the localized cooling of the $q = 1$ surface by the pellet. This island traps some of the ionized pellet material and the density perturbation increases the resistivity through impurity concentration, which maintains the magnetic island. On the other hand, the magnetic island affects the local confinement in such a way as to increase the density. A possible source for the background density perturbation is the divergence of the pinch velocity. This model is consistent with the main observations reported above, except in what concerns the snake radius which is, in many cases, significantly smaller than that of the $q = 1$ surface, pointing out the problem of the interpretation in terms of current profile.

4.1.4. Pellet-induced ELMs. Edge localized modes (ELMs) are MHD instabilities in the pedestal region typical for H-mode scenarios. They provide burst-like energy and particle transport through the external transport barrier in a quasi-periodic way, followed by a phase of pedestal pressure rebuilding [133, 134]. When injected into H-mode plasmas, pellets tend to trigger systematically an ELM [90, 118, 135–138], whose cause originates in the difference between the particle and heat transport characteristics. Indeed, because ablation is a globally adiabatic process, a pellet cools down the plasma and increases the density within the deposition

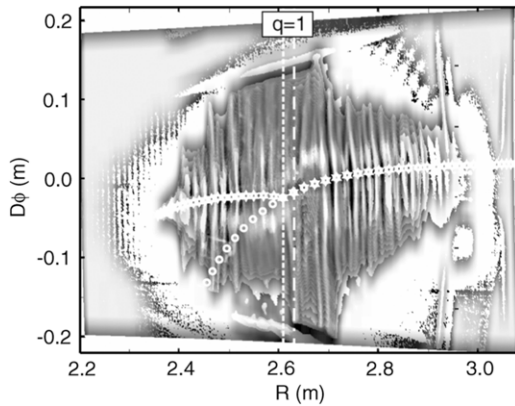


Figure 24. Image of the ablation pattern of a pellet injected just before the time of a sawtooth crash in Tore Supra (pellet TS12637). The pellet is injected from right to left. D_ϕ is the toroidal direction and R the major radius. Both the unperturbed (circles—see figure 4) and perturbed trajectories (stars) are displayed. The position of $q = 1$ is shown, as determined by magnetic equilibrium reconstruction (dash-dotted line) and analysis of the H_α signal (dashed line) [37].

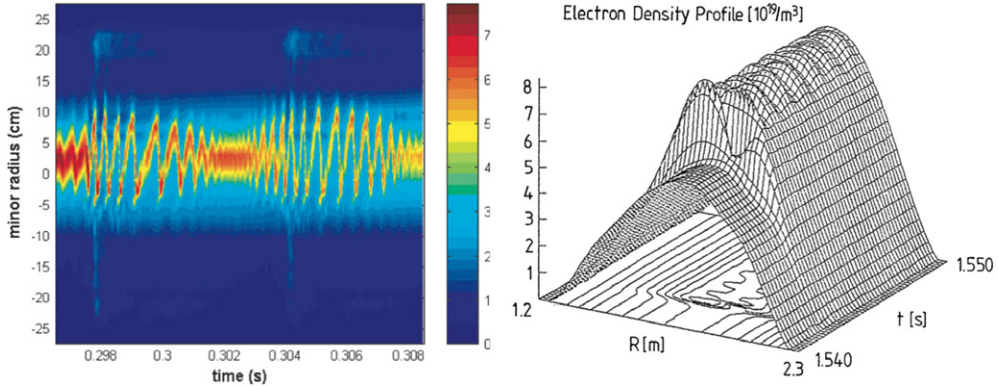


Figure 25. (left) Time-history of a typical pellet-induced snake oscillation viewed from the top of the HT-7 tokamak by the vertical SXR camera [129]. (right) Snake-like oscillation of the electron density after pellet injection in TEXTOR-94 [78].

area. This generates strong density and temperature gradients that lead to a non-adiabatic evolution of the pressure profile driven by energy and particle diffusion: at the end of the ablation zone, a pressure perturbation with a dipole structure appears, the zone of higher pressure being located outside the radius of maximum pellet penetration, that of lower pressure inside. With increasing time, both the inner-negative and outer-positive pressure blobs start transforming and moving as prescribed by diffusion: they broaden while shifting their centre of mass. The negative blob moves towards the plasma centre, the positive blob towards the plasma edge. When the latter reaches the pedestal region, it causes a strong increase in the pressure gradient, which triggers an ELM when the ballooning limit is exceeded [137]. This mechanism is consistent with the fact that the delay between the time at which the pellet is injected and that at which the ELM is triggered scales as the square-root of the pellet penetration, figure 27. It also explains why the fuelling efficiency increases with penetration: the longer time delay

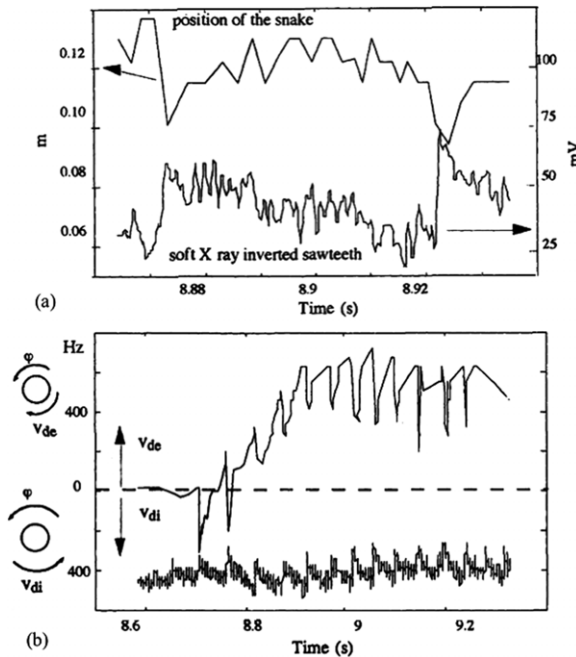


Figure 26. (a) Sawtooth effect on the snake radius in Tore Supra. The snake radius is displayed along with a soft-x-ray diode signal viewing the plasma vertically, showing a sharp decrease at each sawtooth crash. (b) Snake frequency as a function of time, showing the influence of the sawtooth crashes (visible on the soft-x-ray signal at the bottom). For reference, the toroidal rotation direction is also indicated [128].

allows the deposited material to diffuse deeper in the discharge, in regions non perturbed by ELMs.

Pellet-induced ELMs are responsible for a significant loss of the deposited material. In ASDEX-U, after each pellet injection, a series of ELMs is triggered that can expel out of the plasma up to 50% of the pellet material in ~ 10 ms. This first phase corresponds to a decrease of the plasma energy content due to convective losses associated with the ejected particles [139, 140]. The ELM characteristics also depend on the poloidal location of the injection point. In DIII-D, LFS-launched pellets can induce a H- to L-mode transition of duration up to ~ 25 ms, when HFS-launched pellets trigger only an ELM of type-I, figure 28. Globally, the pellet-induced perturbation is shorter and the fuelling efficiency higher for HFS than for LFS injection, partly due to the ∇B -induced drift that helps the matter penetration in the former configuration [90, 118, 136]. The same picture is observed in ASDEX-U, showing that the fuelling efficiency increases and that the ELM activity decreases when the pellet launching point is shifted from the LFS to the HFS and when the pellet penetration increases [141].

4.2. Non-local transport

The non-local response of the plasma to the injection of a pellet was first observed in TFR, where a cold front was measured, propagating in front of the pellet and causing at the crossing of the $q = 1$ radius an instantaneous fall of the electron temperature in the plasma centre [142]. The same phenomenon was also observed in other devices in the case of significant pellet penetration. In Tore Supra, the cold front is measured to propagate at ~ 25 km s $^{-1}$ in front of

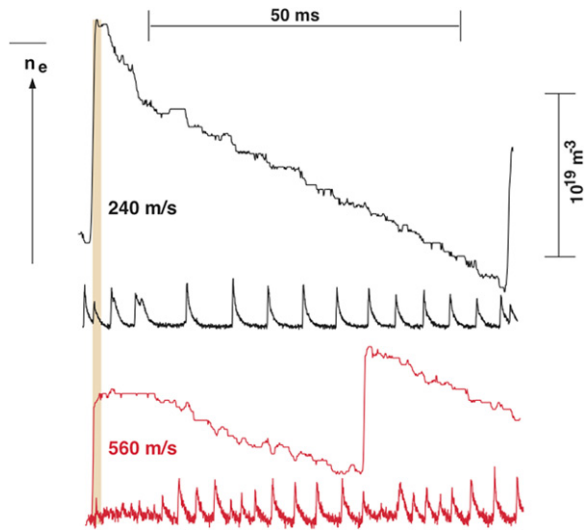


Figure 27. Density decay and ELM activity (D_α in the divertor) after HFS pellet injection at two velocities in ASDEX-U. The initial density decay time increases from 48 ms (at $v_p = 240 \text{ m s}^{-1}$) to 58 ms (at $v_p = 560 \text{ m s}^{-1}$) and the ELM activity in the first 15 ms after the pellet injection is reduced for the higher injection velocity [141].

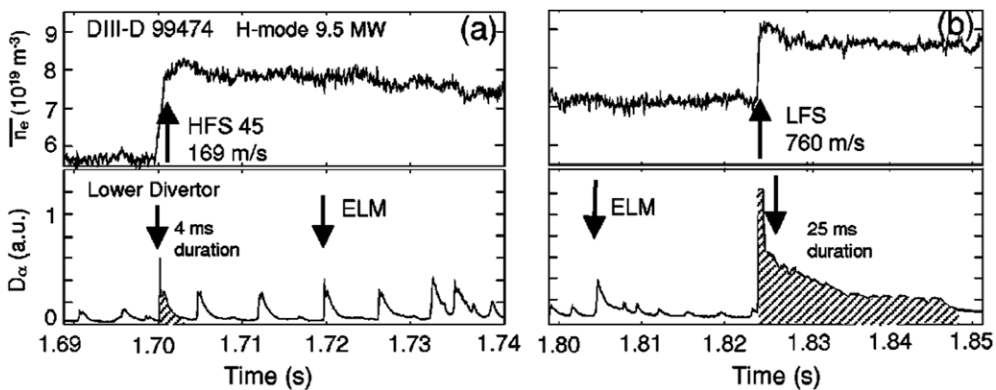


Figure 28. Details of pellet-induced ELM activity in an ELMy H-mode DIII-D discharge. Line average density and divertor D_α light emission for (a) a HFS-launched pellet and (b) a LFS-launched pellet [90].

the pellet, causing a decrease of the local temperature of $\sim 10\%$. The rapid phase is triggered when the front is yet outside the $q = 1$ surface: it starts from the magnetic axis and propagates outward, the temperature profile becoming hollow during a short time interval [143], figure 29. In JIPPT-IIU, the cold front propagates at about the pellet velocity, but accelerates dramatically when it crosses the $q = 1$ radius [78].

The picture is different in the case of shallow pellet injection. Then, the same cold front propagating inward is observed, but it is followed by an increase in the central temperature. This phenomenon was studied in RTP, Tore Supra and LHD, in discharges purely ohmic or with significant additional power (ECRH and LHCD) [144–147], figure 30. The temperature increase disappears at high density and is limited to the plasma core ($\rho/a \leq 0.3$). In RTP, it

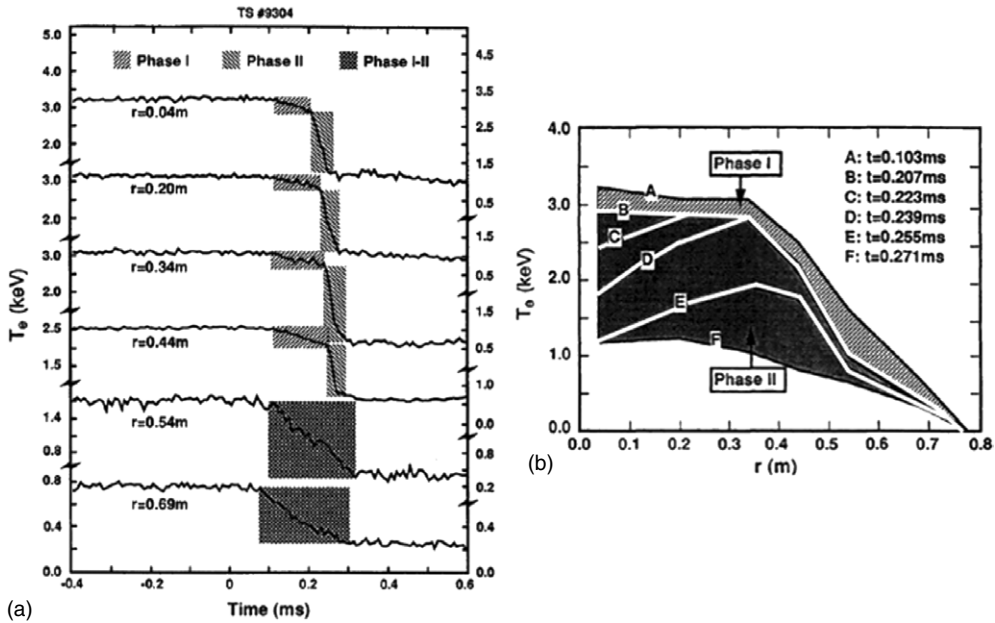


Figure 29. (a) Time evolution of electron temperature of six horizontal channels by a fast acquisition ECE system during pellet injection in Tore Supra. The sampling time is $8\ \mu\text{s}$ and the time origin is set to the moment when the pellet arrives at the plasma edge. Phases I, II and I-II are the central slow decrease phase, the central fast decrease phase and the edge decrease phase, respectively. (b) Temperature profiles at different times during pellet injection [143].

is associated with the formation of a region of high-temperature gradient (transient transport barrier) whose position appears to be linked to the location of low-order rational magnetic surfaces. For ohmic and EC-heated plasmas with the resonance moderately off-axis, the temperature rise is peaked in the plasma centre and the base of the barrier is located close to the $q = 2$ surface. For EC-heated plasmas with far off-axis resonance, i.e. in plasmas exhibiting hollow temperature profiles, the temperature rise starts off-axis, near the innermost low-order rational surface (typically $q = 3$). Time-dependent transport simulations show that the propagation of the inward cold pulse is consistent with local transport, while the core temperature rise is a slower phenomenon requiring a large transient drop of the heat diffusivity in the region $1 < q < 2$ [144, 145].

4.3. Loop voltage modification

In T10, post-pellet peaks of loop voltage are observed that cannot be explained by the change of temperature or effective charge. The authors propose an explanation according to which the term containing the product $v_r \times B_\theta$, where v_r is the plasma flow velocity and B_θ the poloidal field, must be retained in Ohm's law [148]. With this hypothesis, the latter writes: $j_\phi = \sigma(E_\phi + v_r \times B_\theta)$, where $v_r = -D\nabla n/n + v_{\text{pinch}}$. In these expressions, j_ϕ is the current density, σ the plasma conductivity and E_ϕ the toroidal electric field. The peaks of loop voltage would be due to the inward v_r resulting from the penetration of the pellet deposited material. Since in this case the E_ϕ and $v_r \times B_\theta$ contributions are of opposite sign in Ohm's law, to maintain the current density at its prescribed value requires a higher value of E_ϕ .

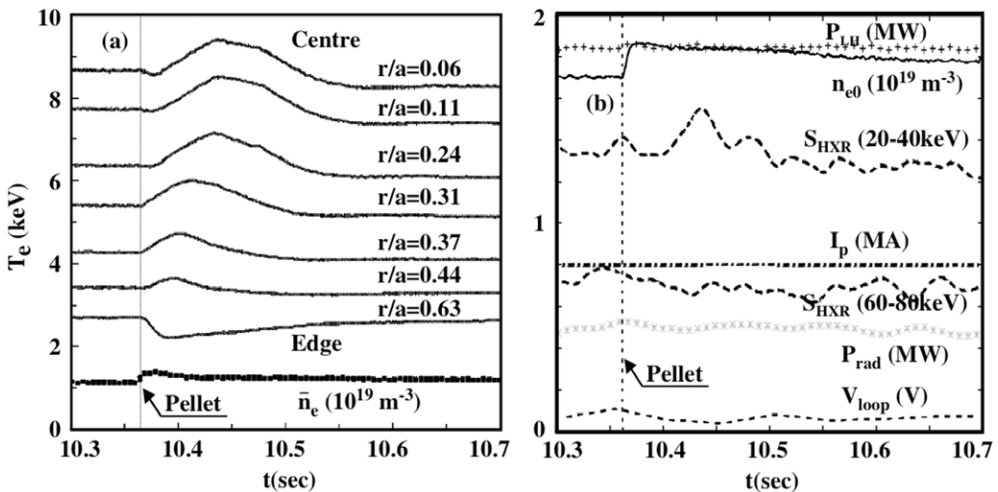


Figure 30. Evidence of non-local transport during pellet injection experiment in the full non-inductive current regime with LHCD in Tore Supra. (a) ECE temperature response and line average density $\langle n_e \rangle$. (b) Time evolution of the plasma current I_p , central density n_{e0} , LH input power P_{LH} , total radiated power P_{rad} , loop voltage V_{loop} and HXR signal (a.u.) [146].

5. Fuelling efficiency

5.1. Dependence on injection and plasma characteristics

Although the pellets are entirely ablated inside the plasma, their fuelling efficiency ε_f —defined as the proportion of the deposited material that remains effectively in the discharge, is almost never found to reach 100%. This is partly due to the particle diffusion (possibly transiently enhanced after the injection of a pellet) but also to the ∇B -induced drift that, for LFS-launched pellets, expels a part of the deposited particles out of the discharge. This dependence of the fuelling efficiency on the pellet injection location was first evidenced in ASDEX-U with pellets injected at 130 m s^{-1} from both the LFS and HFS of the machine [117]. An increase in penetration was observed—by up to a factor of 2 (from 7 to 15 cm, see section 3.2.2)—and a fuelling efficiency four times larger (from 14% to 55%) when the pellets were launched from the HFS, with a degradation of ε_f with additional power weaker than in the case of LFS injection [135, 136]. These different features are explained by the drift of the pellet material down the magnetic field gradient.

- (i) In the case of HFS injection, the deposited material drifts in front of the pellet, penetrating deeper in the discharge and pre-cooling the plasma, which—for a strong enough plasma perturbation—can increase both the penetration and the fuelling efficiency.
- (ii) The heating of the deposited material is faster when the additional power increases, leading to a higher value of the cloud β , and thus to a larger ∇B -induced displacement. Since the latter helps the matter penetration for HFS-launched pellets but expels it out of the discharge in the case of LFS injection, the difference between both configurations increases with additional power [137].

From that time, systematic studies were performed to characterize the performances of pellet injection—in terms of deposition depth and fuelling efficiency—with both the location of the injection point and pellet velocity.

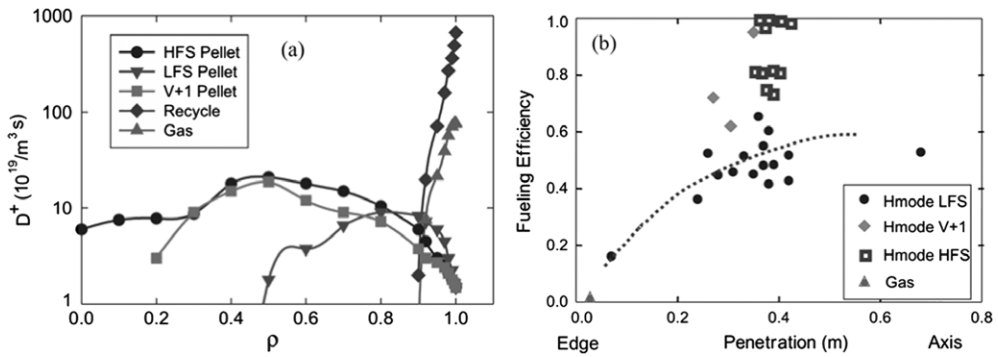


Figure 31. (a) Fuelling source profiles in DIII-D for a 4.6 MW ELM plasma with different fuelling schemes: HFS, LFS and VHFS pellet injection, gas puff. The pellet source profiles are from experimental results in similar H-mode discharges and assume continuous 3 Hz injection of $r_p = 1.35$ mm size pellets. (b) Fuelling efficiency in ELM plasma as a function of fuel penetration for LFS pellets, vertical pellets, HFS pellets and inner wall and outside top gas puffing. The dashed line is an approximate fit to the LFS injected pellet data [118].

It was shown in JET that, in L-mode plasmas, injection from the HFS was globally more efficient than from the LFS, all other parameters being equal [149]. For two pellets of identical particle content, the increment of density is $\sim 50\%$ higher and the post-pellet density relaxation slower by $\sim 30\%$ when the pellet is injected from the HFS- 45° than when it is injected from the LFS, in the equatorial plane. As a whole, the material deposition is deeper for HFS-launched pellets, even at lower injection velocity. In DIII-D, the effective source and fuelling efficiency of gas puff and pellet injection were compared as a function of the poloidal location of the fuel injection [90, 118], figure 31. It was found that, for gas puff, $\varepsilon_f \sim 1\%$ whatever the location of injection when, in the case of pellets, it depends strongly on the poloidal location of the launching point. Four different injection lines were used, with pellets penetrating typically up to midradius in ELM plasma discharges: LFS, V + 1 (at the top of the vacuum chamber), HFS- 45° and HFS. It was observed that the increment of density Δn increases continuously when the injection point shifts from the LFS to the HFS: $\Delta n(\text{LFS}) \leq \Delta n(\text{V} + 1) < \Delta n(\text{HFS-}45^\circ)$ even if, in this last case, the injection velocity is reduced by a factor ~ 4 (from 570 to 120 m s^{-1}). The corresponding fuelling efficiencies follow the same trend, with $\varepsilon_f(\text{LFS}) \sim 50\text{--}60\%$, $\varepsilon_f(\text{V} + 1) \sim 60\text{--}70\%$ and $\varepsilon_f(\text{HFS-}45^\circ) \sim 80\text{--}90\%$. In addition, in the case of HFS injection, the matter deposition is observed to be well inside the radius of maximum pellet penetration, clearly demonstrating the predominant role of the ∇B -induced drift.

For a given pellet size, as well as the location of the launching point, the other parameter that can be varied to optimize ε_f is the injection velocity (in START, fuelling efficiencies of $\sim 100\%$ were obtained in VHFS injection with pellets penetrating up to the plasma equatorial plane [150]). To determine the scaling of the pellet penetration λ_p with injection velocity in the HFS configuration, the pellet launching system of ASDEX-U (LFS and HFS- 45° , with $v_p = 240 \text{ m s}^{-1}$) was completed by the addition of a line HFS- 72° , allowing velocities up to 560 m s^{-1} [151]. Experiments confirmed that, also for HFS-launched pellets, the scaling of the penetration remained similar to that deduced from the IPADB in the LFS configuration: $\lambda_p \propto r_p^{15/27} v_p^{1/3}$ [26] and that the improved matter penetration was the result of the ∇B -induced drift. This confirms that the increase in penetration due to the plasma pre-cooling remains modest as soon as the pellet penetrates deep enough. From a practical point of view, the optimization of ε_f requires that the radius of maximum pellet deposition (tangency point

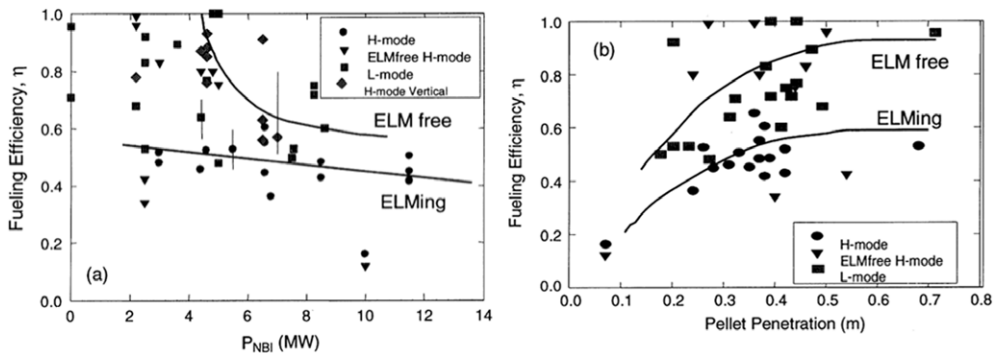


Figure 32. (a) Fuelling efficiency as a function of the NBI power in DIII-D. (b) Fuelling efficiency as a function of the pellet penetration depth. Curves showing the trend for ELM-free and ELM_y discharges are also shown [135].

between the pellet path and the flux surfaces in the off-axis injection configuration) is the closest possible to the magnetic axis. This means the combination of a launching point located on the HFS and of a high velocity. In this perspective, attempts were made to harden the pellets by doping the frozen hydrogen with $\sim 1\% N_2$. First results indicate a significant reduction of pellet degradation for operation in the vicinity of the critical velocity [149].

The dependence of ε_f on the confinement regime was studied in ASDEX-U and DIII-D [135, 137], figure 32. If, in L-mode discharges, the fuelling efficiency is essentially determined by the pellet penetration and location of the launching point, one must take into account the effect of pellet-induced ELMs as soon as H-mode plasmas are considered since the associated mass loss can be as large as $\sim 50\%$ of the pellet initial particle content. As a consequence, the value of the fuelling efficiency is similar in L- and ELM-free H-mode plasmas ($\varepsilon_f \sim 80\%$ for $\lambda_p/a \sim 0.6$) and lower in ELM_y H-mode discharges ($\sim 50\%$ for the same penetration).

5.2. Global particle balance

If the above discussion points up the higher fuelling efficiency of pellets with respect to gas puff (ε_f being defined just at the end of the fuel injection), the overall efficiency of a fuelling technique depends not only on the instantaneous matter deposition but also on its time of residence in the plasma and possibly induced wall pumping. In fact, it was shown in TEXTOR-94 that the deuterium wall retention increased during ~ 100 ms after every pellet injection, likely due to the drop of ion- (or high-energy neutral-) induced desorption driven by the transient decrease of the plasma temperature [152]. Also, in Tore Supra, two macroscopically similar LHCD discharges of 2 min duration were compared, the first fuelled by conventional gas puff, the second by pellet injection [153]. Although a satisfactory pellet fuelling efficiency ($\varepsilon_f \sim 60\%$) was obtained by notching the LH power, much higher than that of gas puff ($\sim 5\%$), the global particle balance was identical for both discharges, exhibiting in particular the same wall retention, figure 33. As demonstrated by the identical edge parameters, this situation, which is mainly due to the domination of the overall particle recirculation by the recycling, questions the possibility of controlling the particle balance and reducing the wall retention by optimizing the fuelling method, at least for the low plasma current and average density considered in this experiment.

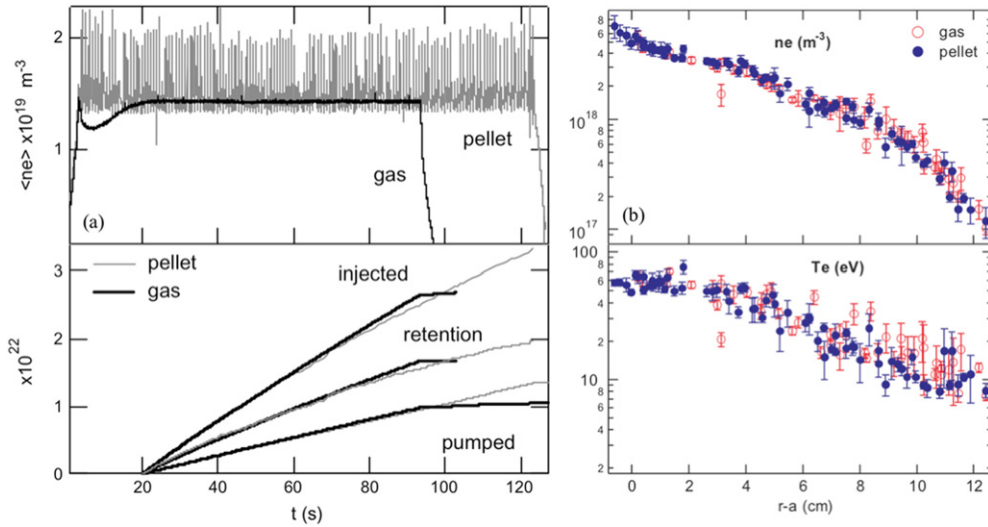


Figure 33. (a) Comparison of the volume average density, injected and pumped particle fluxes and resulting retention for two Tore Supra 2 min discharges fuelled by pellet injection (TS33009) or gas puff (TS33001). (b) Comparison of the density and temperature profiles in the SOL for discharges TS33001 ($t = 20.2$ s) and TS33009 ($t = 12.3$ s, 180 ms after pellet ablation) from a reciprocating Langmuir probe [153].

6. High density/high performance scenarios

6.1. H-mode plasmas

6.1.1. L–H transition and operational domain. Future reactor grade experiments, like ITER, are planned to operate in H-mode [154] and close to the Greenwald density limit [155]. If, with standard fuelling methods, these two requirements are hardly compatible, the situation is greatly improved when using pellet injection. This is due to the ability of the latter to deposit material deeper in the discharge, which allows the decoupling of the edge and core plasma parameters.

In fact, pellet injection was demonstrated not only to be compatible with H-mode operation but also to lower the threshold of the L–H transition, figure 34. In DIII-D, the injection of a peripheral pellet, outside $\rho/a \sim 0.7$, reduces the threshold of the L–H transition by 20–25% [156]. In these experiments, both the edge density and temperature at the transition are lower than those predicted by the different available theories, demonstrating that the attainment of a critical temperature is not necessary to trigger a H-mode: if both T_e and T_i drop after the injection of a pellet, the density gradient increases, and thus the radial electric field $E_r(\propto \nabla n/n)$. Globally, the injection of a shallow pellet increases ∇E_r , and thus the shear velocity $E_r \times B$, which explains the lower threshold of the L–H transition [157, 158]. Also, in the circular-limiter tokamaks TUMAN3 and TUMAN3M, ohmic H-modes were obtained consecutively to the injection of a shallow LiD pellet [159]. Despite the differences in the geometries and heating methods, the energy confinement of these ohmic H-mode plasmas is consistent with the JET/DIII-D ELM-free H-mode scaling.

Pellet fuelling also enables to extend the H-mode operational domain toward high densities. In JT60-U, pellet injection allowed to maintain a good confinement ($H_{89p} \sim 2$) H-mode operation up to a density $\sim 0.7 \times n_{Gw}$ (where n_{Gw} is the Greenwald density), when the H–L

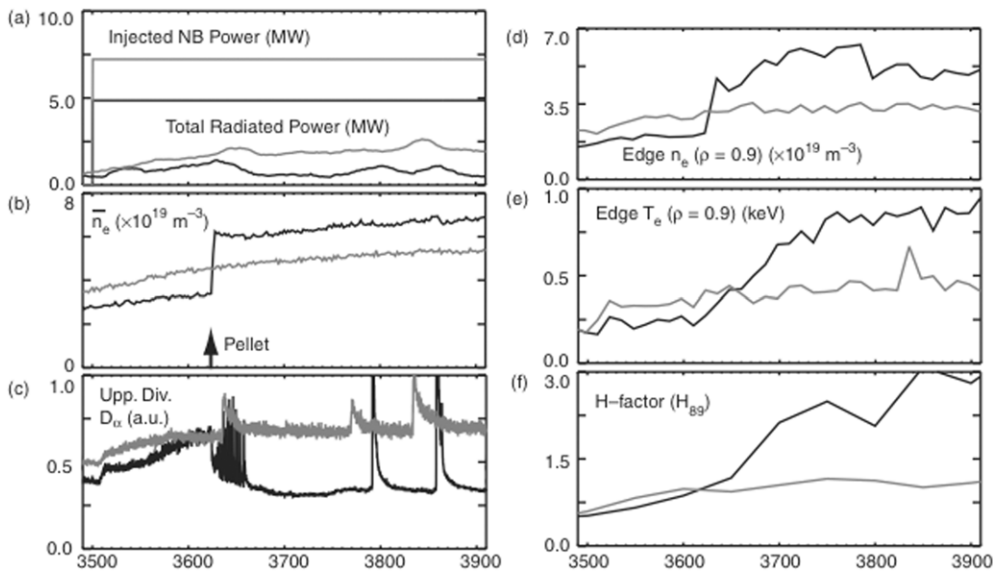


Figure 34. Time-history of a pellet-induced H-mode transition discharge in DIII-D (black line) and reference discharge (grey line) with no H-mode transition. (a) Total NBI power and total radiated power, (b) line averaged electron density, (c) divertor $D\alpha$ emission, (d) edge electron density at $\rho = 0.9$, (e) edge electron temperature at $\rho = 0.9$, (f) confinement enhancement factor H_{89} . A single pellet is injected at time $t = 3622$ ms from the HFS of the plasma [156].

limit is at $n/n_{Gw} \sim 0.6$ with conventional gas puff [138, 160, 161]. These pellet-fuelled discharges exhibit a density profile similar to those fuelled by gas puff, but develop in addition transport barriers on both T_e and T_i [162]. In ASDEX-U, high-confinement H-mode discharges were performed up to densities larger than n_{Gw} using pellet fuelling. However, to maintain such a high performance requires an efficient pumping of the plasma edge. If the latter is not strong enough, the confinement is degraded [163]. In JET, the domain of operation in ELM My H-mode was extended from 0.5 to $1.6 \times n_{Gw}$ by pellet fuelling, the price being nevertheless a relative degradation of the confinement above $0.7 \times n_{Gw}$ [164]. As a whole, and despite some machine-to-machine variability, the H-mode operational domain in density is extended from $n/n_{Gw} \sim 0.5\text{--}0.6$ to $n/n_{Gw} \geq 1$ in pellet fuelled discharges, and up to ~ 2 in some particular cases, figure 35. The global trend is nevertheless a decrease in the confinement with increasing density.

More difficult is the fuelling of quiescent H-mode discharges [165]. This high-confinement regime is characterized by a high-ion temperature in both the plasma core and the pedestal region, and by the absence of ELMs that are replaced by smoother MHD edge oscillations. Attempts were performed to increase the density of QH-mode plasmas by pellet injection because using gas puff generally causes a transition toward a standard ELM My H-mode regime. In ASDEX-U, preliminary pellet fuelling experiments allowed to reach densities up to $\sim 1.4 \times n_{Gw}$ without triggering an ELM [166, 167]. Conversely, in DIII-D, no scenario to increase the density of QH-mode plasmas by means of pellet injection was found: when the injection of a first pellet increased the density by $\sim 30\%$ (in both the core and pedestal), the second pellet triggered systematically an ELM [168]. In quiescent double-barrier H-mode plasmas, the injection of a shallow pellet provokes an ELM phase that lasts $\sim 40\text{--}80$ ms, but the density decreases on a longer timescale (~ 180 ms), leading to a transient phase of higher performance [169].

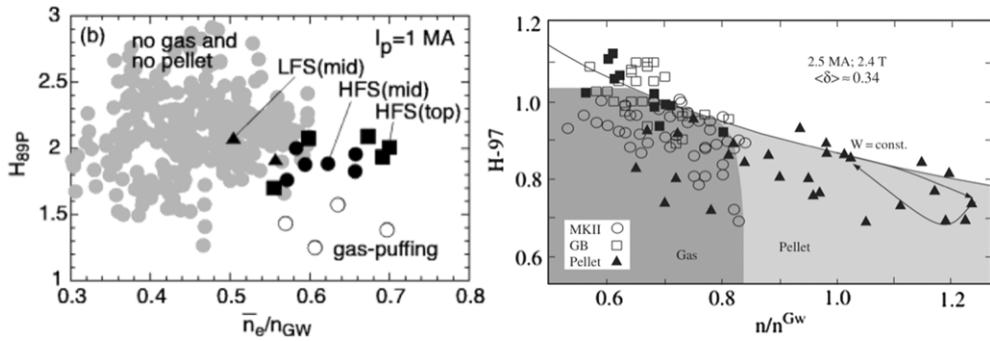


Figure 35. Extension of the H-mode operational area from the relationship between the confinement enhancement factors H_{89P} and H_{97} and the Greenwald fraction n/n_{GW} . (left) JT60-U plasmas. Grey symbols show data without gas puffing and without pellet injection; solid circles, squares and triangles are for HFS, VHFS and LFS pellet injection, respectively; open circles are for gas puffing. (right) JET 2.5 MA/2.4 T high-triangularity plasmas. Open symbols are for gas puffing in the MKII (circles) and GB (squares) divertor configurations. Full symbols are for reference discharges (squares) and pellet-fuelled discharges (triangles) in the GB divertor configuration [160, 164].

6.1.2. Integrated scenarios. Integrated scenarios combining pellet fuelling, additional heating and edge pumping were developed, the aim of which was to approach (or to allow an extrapolation to) ITER-like conditions.

In JT60-U, ELMMy H-mode discharges were fuelled by shallow pellet injection, in order to reproduce the effective deposition profile expected in ITER. No significant loss of confinement was observed ($H_{89P} \sim 1.5$), but the heat and particle fluxes on the inner leg of the divertor were increased by a factor of two, and the peak value by ~ 1.6 . It is noteworthy that a beneficial effect of such a high-particle flux could be the drag of the α -particles towards the pumping ducts [170, 171]. In DIII-D, experiments were performed to realize discharges exhibiting simultaneously a density above the Greenwald limit and a H-mode confinement. The scenario was defined from the analysis of the H-L transition, generally caused by a divertor or scrape-off layer (SOL) thermal collapse. It consists of (i) directly fuelling the plasma core by means of pellet injection, (ii) actively pumping the edge to avoid the development of multifaceted asymmetric radiation from the edge (MARFE) and (iii) limiting the additional NBI power to avoid the onset of MHD instabilities (always observed for $P_{NBI} > 3$ MW when combined with pellet injection). With this strategy, 600 ms duration discharges were realized at $n/n_{GW} \sim 1.5$, with a phase of H-mode confinement lasting as long as 300 ms [172]. Similarly, in ASDEX-U, high-density pellet-fuelled H-mode discharges were performed using the HFS-45° injection line (see [173] for a general review on these experiments). The high-density phase ($\sim 1.2 \times n_{GW}$) was maintained during 2 s, i.e. about 20 times the particle confinement time [139]. From the analysis of these experiments, it follows that the H-mode limits in both confinement and density are linked to the edge parameters and that the deeper fuelling by means of pellet injection allows a steady-state operation at higher density, the increment δn being proportional to the pellet fuelling rate, figure 36. This is because, when using conventional gas puffing, both the core and edge densities increase simultaneously, which leads to a loss of confinement even for $n < n_{GW}$. When using pellet injection, the plasma behaviour depends on the available pumping power. When it is low, the edge density increases and the confinement is degraded. Conversely, when it is efficient enough to maintain the edge density at a constant value, the H-mode is maintained even at $n > n_{GW}$. It remains that—even for pellet-fuelled discharges—the global trend is a decrease in the confinement with increasing density, and the higher the power coupled to the

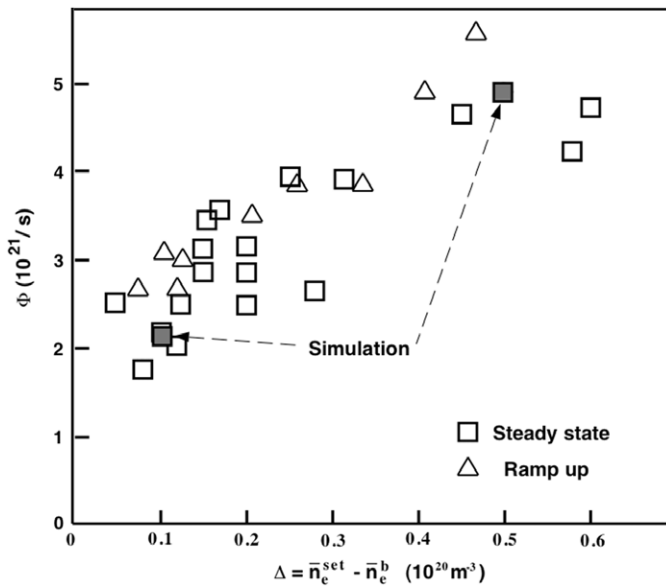


Figure 36. Pellet particle flux Φ versus pellet-induced density increment Δ in ASDEX-U. Data are taken from steady-state discharges (open squares) and from discharges with slow density ramp-up [139].

plasma, the stronger the degradation, see section 5.1. The cause of the latter is triple, i.e. (i) the increase in both the density and neutral flux at the edge, (ii) the onset of NTMs owing to the cooling of the plasma core consecutively to the injection of a pellet and (iii) the pellet-induced ELMs that can expel out of the discharge up to 50% of the pellet material in ~ 10 ms. However, after a phase of rapid expulsion of the deposited material, the plasma energy content recovers its pre-pellet value faster than the density decreases. This leads to a transient high-performance phase, the confinement being as high as before the pellet injection, but at a higher density [139, 140], figure 37. In ASDEX-U, the highest densities were obtained by combining gas and pellet fuelling, allowing discharges at $n \sim 2 \times n_{Gw}$, with 5 MW of NBI [137]. In JET, these results were used to optimize the fuelling of ELM My H-mode, in order to realize discharges at $n \sim n_{Gw}$ without confinement loss ($H_{97} \sim 1$). The pellets were launched from the HFS-45° injection line showing a matter deposition deeper than in the case of LFS injection [97]. In such a configuration, the displacement of the deposited material increases with the power coupled to the plasma, which compensates for a part the small pellet penetration owing to the low injection velocity. Practically, the three causes of confinement degradation mentioned above were limited by (i) restricting to 6 Hz the maximum injection frequency to minimize the increase in the edge density, (ii) maintaining at a significant level the coupled power to keep the core temperature high enough and avoid the onset of NTMs and (iii) by limiting—once the target density is reached—the fuelling to short trains of 3 pellets injected at 2.5 Hz to minimize the losses due to the induced ELMs. With such a scenario, discharges with density $n \sim n_{Gw}$, $\beta_N = 1.85$ and $H_{97} = 0.86$ were obtained [149, 164, 174, 175], figure 38 (left). These discharges are characterized by a peaked density and a temperature profile relatively flat, the pressure and safety factor profiles remain unchanged, the increase in resistivity owing to the plasma cooling being compensated by the decrease in the effective charge Z_{eff} (from 2 to 1.5). Globally, if pellet fuelling significantly extends the domain of operation in ELM My

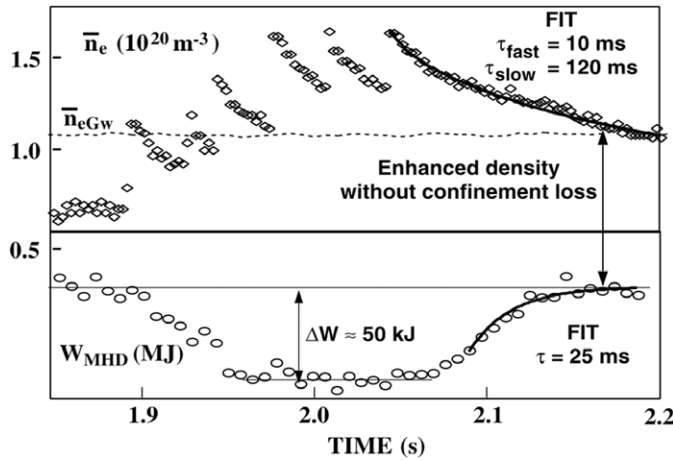


Figure 37. Evolution of plasma density \bar{n}_e and stored energy W_{MHD} ¹ during and after a pellet sequence in ASDEX-U. Fit results for the phase after the sequence are also displayed, during which the stored energy recovers transiently its pre-sequence value at enhanced density [140].

H-mode, the H_{97} scaling in density ($\propto n^{0.4}$) is only valid for $n < 0.7 \times n_{Gw}$. Beyond this value, the confinement becomes independent of the density.

Pellet injection was also demonstrated to be efficient to fuel high-triangularity ITER-like plasmas. In JT60-U, high-density, high-triangularity ($n \sim 0.7 \times n_{Gw}$, $\delta = 0.45$) discharges were fuelled with multiple VHFS pellet injection, showing an improved performance ($H_{89PL} > 2$, $\beta_N \sim 2.2$) with respect to a similar discharge fuelled by gas puff ($H_{89PL} > 1.2$). The main difference between these two types of discharge is the behaviour of the pedestal parameters: in pellet-fuelled plasmas, both T_e and T_i increase with the pedestal density, when the opposite is observed with conventional gas puff [176]. In JET, discharges of upper triangularity $\delta^u = 0.53$ and density $n \sim n_{Gw}$ were fuelled by HFS-45° pellet injection. They show a better confinement of the deposited material than standard discharges (the pellet fuelling rate was only 20% of the one required in gas puff) and the post-pellet density decay displays only a very small fast component, figure 38 (right). However, this good confinement creates a cold, dense plasma core that results in a strong increase in radiative losses by Bremsstrahlung, finally causing an abrupt loss of confinement that terminates the high-performance phase of the discharge [164].

It is interesting to compare the performance obtained up to now with that required to operate ITER in the $Q_{DT} = 10$ reference regime. In JET, $I_p = 2.5$ MA, $B = 2.4$ T ($W_{MHD} = 6$ MJ)¹ discharges at $n \sim n_{Gw}$ were performed (for a target value of $0.85 \times n_{Gw}$ in ITER), with $H_{98(y,2)} = 0.82$ (1 required) and $\beta_N \sim 1.8$ (1.8 required). These results were obtained with 4 mm³ pellets launched at 160 m s⁻¹ from the HFS-45° injection line. The injection frequency was 6 Hz during the current ramp-up, then reduced to 2 Hz during the plateau. Although the values obtained are transiently close to the target, developments are still necessary to maintain steady-state performance [177]. Finally, it can be noted that, when compared with the other methods aiming at performing high-triangularity, high-performance discharges (extreme shaping, impurity seeding), HFS pellet injection has the advantage of decoupling the edge and core plasma parameters, which limits for a part the magnitude of the ELMs [178].

¹ W_{MHD} is the plasma stored energy calculated from the magnetic measurements by statistical regression on a database of pre-calculated equilibria.

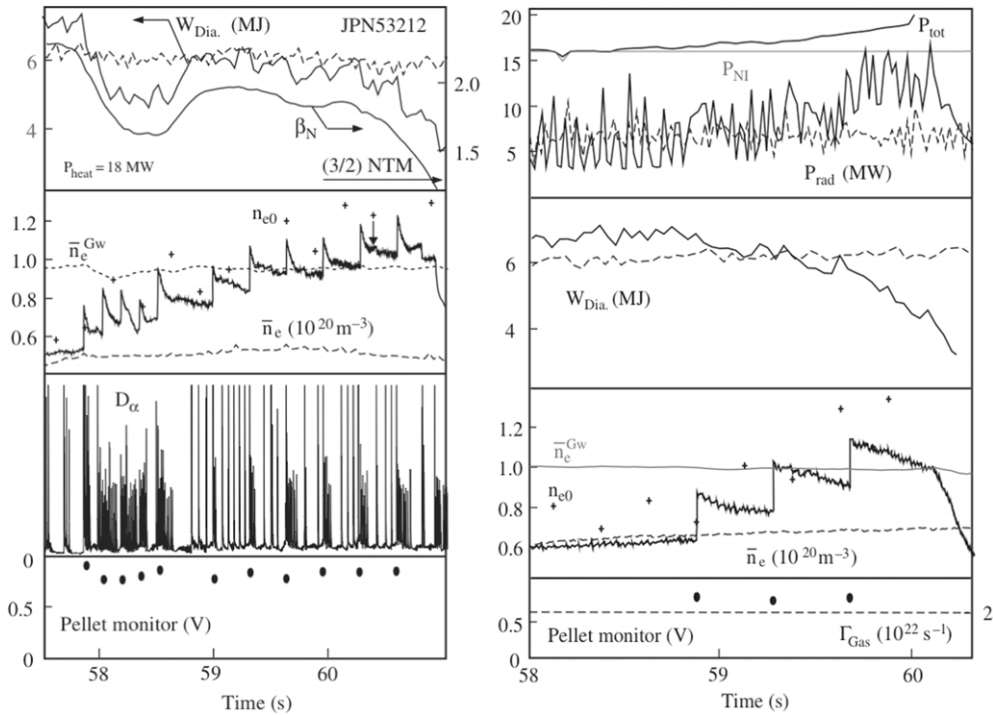


Figure 38. (left) Optimized pellet refuelling for high-performance high-density operation. From bottom to top, fourth box: microwave pellet mass detector signal, showing the two trains of pellets, the first at 5 Hz to increase the density above n_{Gw} , the second at 3 Hz to maintain it at the target value; third box: D_α radiation signal from the outer divertor region monitoring ELMs; second box: line averaged (full line), Greenwald (short-dashed line) and central (++) densities for the pellet-fuelled discharge and line averaged density for a reference unfuelled discharge (long-dashed line); first box: diamagnetic plasma energy and normalized pressure for the pellet-fuelled discharge and diamagnetic plasma energy for the reference discharge (long-dashed line): it can be seen that $n_e > n_{Gw}$ is achieved at the energy content of the unfuelled reference discharge as energy recovers after the initial pellet sequence. (right) Pellet refuelling in a discharge with extreme triangularity compared with a gas puff reference shot. From bottom to top, fourth box: sequence of pellets (three pellets at 2.5 Hz, equivalent to $0.4 \times 10^{22} \text{ s}^{-1}$ averaged particle flux) and steady-state gas puffing at $2 \times 10^{22} \text{ s}^{-1}$ injected in the high-triangularity and reference discharges, respectively; third box: line averaged (full line), Greenwald (grey line) and central (++) densities for the pellet fuelled discharge (note the absence of the fast decay phase after each pellet injection) and line averaged density for the reference discharge (long-dashed line), showing that the pellet sequence initiates a much stronger density ramp-up than the steady-state gas puffing; second box: diamagnetic plasma energy for the high-triangularity (full line) and reference (dashed line) discharges, showing that the strong density peaking and according temperature reduction in the pellet-fuelled discharge (for $t > 59.5 \text{ s}$) finally causes a core collapse due to Bremsstrahlung losses terminating the high performance phase; first box: power balance for both discharges, showing that the radiated power remains constant for the reference discharge (dashed line) when it increases for $t > 59.5 \text{ s}$ in the case of the extreme triangularity discharge (full line) [164].

6.2. ITBs plasmas

6.2.1. Pellet-induced ITBs. The injection of a pellet (or of a train of pellets) is a powerful technique to trigger an internal transport barrier (ITB), with or without preheating of the target plasma [179] (see [180] for a recent review). These pellet-induced ITB plasmas are in fact an extension of the so-called pellet-enhanced performance (PEP) mode, where the preheating

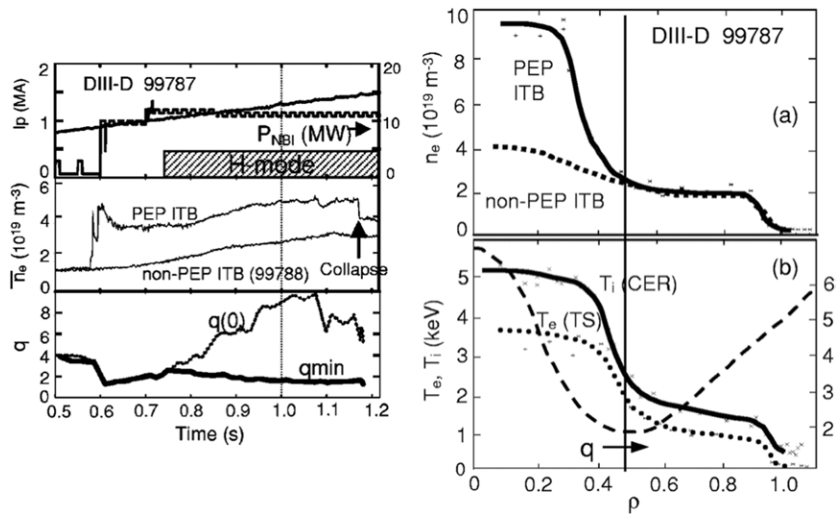


Figure 39. (left) Temporal evolution of the key parameters in a typical PEP-mode ITB discharge in DIII-D. A pellet is injected from the LFS during the current raise followed 20 ms later by a HFS-launched pellet at 0.6 s. (top) Plasma current I_p and NBI power, (middle) averaged density, (bottom) central and minimum values of the safety factor. (right) Profiles of the (a) electron density, (b) electron and ion temperatures and q -profile. In both figures, the density for a non-pellet ITB plasma is also shown for comparison [90].

allows independent control of the current and pressure profiles. These regimes, which are characterized by a pressure strongly peaked in the core of the discharge, were first obtained in JET [181, 182], then in ALCATOR C-mod [183], TFTR [184], DIII-D [90], JT60-U [185, 186] and Tore Supra [187]. High confinement modes exhibiting similarities with PEP-modes were also obtained in T10 [188, 189], FTU [93, 94, 190] and HL-2A [191]. The simplest method of triggering a PEP-mode consists of injecting a pellet into the plasma core and then heating the centre of the discharge in such a way that the temperature rapidly recovers its pre-injection value. The details of the scenario vary from machine to machine. In JET, the core is fuelled either by a single big pellet ($r_p = 2$ or 3 mm) or by a train of smaller pellets whose penetration increases progressively. In ALCATOR C-mod, one uses Li or D-pellets. In DIII-D, a first pellet is launched from the LFS to pre-cool the plasma periphery, and then a second is injected from the HFS, the material of which penetrates up to the discharge centre, figure 39. The additional power can be indifferently ICRH or NBI, in both co- and counter-current injection. The role of preheating is to generate—or maintain—a region of strongly negative magnetic shear in the plasma core: LHCD is used in JET to build a hollow current profile during the initial phase of the current ramp, during which a core electron ITB is observed. The LHCD is then switched off and a 1 s ‘gap’ is used for pellet fuelling and low-power NBI (~ 4 MW) before main heating is applied. In DIII-D, the plasma is preheated by NBI or ECRH. In both cases, this moderate heating prior to core fuelling is believed to limit the current diffusion by increasing the temperature while not heating the plasma sufficiently to inhibit deep pellet penetration.

The characteristics and performance of the pellet-induced ITBs depend on the way they are triggered and on the parameters of the target plasma. In ALCATOR C-mod, the peaking of the density profile is larger when the ITB is triggered by a lithium pellet than by a deuterium pellet. Moreover, in the former case, sawtooth activity is entirely suppressed during the

whole improved confinement phase, when it is only slowed down in the latter [183]. In TFTR and JT60-U, the PEP duration increases with plasma current I_p and central safety factor (q_0), and the size of the high-confinement core increases with decreasing edge safety factor (q_a) [184, 186]. The heating method, NBI or ICRH, is indifferent [183–184] and, when both are applied simultaneously, as in JET, no strong synergy is observed. However, a few MW of additional ICRH in an NBI-heated discharge can increase the neutron yield by twofold. This is because the increased electron heating by ICRH raises the electron temperature, which decreases the rate at which the beams slow down on the electrons and so increases the power to the ions, thereby increasing both thermal and beam-plasma neutron production [182]. As far as performance is concerned, it is noticeable that the highest neutron yields were measured in pellet-induced ITB plasmas: up to 10^{14} s^{-1} in ALCATOR C-mod (i.e. ~ 10 times what is measured in an equivalent L-mode discharge) [192] and, in TFTR, the neutron yield is multiplied by a factor of the order of 4 to 5 during PEP-modes [184].

The main deleterious effect associated with such a high confinement is impurity accumulation. In JET, if impurity transport is strongly anomalous in the outer part of the plasma ($D \geq 1 \text{ m}^2 \text{ s}^{-1}$), it is neoclassical inside the ITB. For extreme peaking factors, the deuterium profile can become hollow. This generally causes the onset of MHD modes that limit impurity accumulation. As a whole, it is this increase in the MHD activity that is responsible for the disappearance of the ITB: onset of low- n ballooning modes when q_0 becomes smaller than ~ 1.1 in JET, off-axis resistive modes in TFTR, sawtooth-like MHD oscillations in JT60-U [184, 186, 193], or when the density peaking falls down ~ 3 , as in ALCATOR C-mod [192].

Pellet-induced ITBs are only transient phenomena (of a typical duration of 2–3 times the energy confinement time τ_E [90, 182, 184]) and the attempts aiming at maintaining them a longer time by fuelling directly the plasma centre were in most cases unsuccessful. In JET, an ITB located at $\rho/a \sim 0.5$ is destroyed by a pellet penetrating at $0.7 \geq \rho/a \geq 0.6$. For shorter penetrations ($\rho/a \geq 0.8$), the ITB can survive the pellet injection but no fuelling is observed in the plasma core [96, 194, 195]. As a whole, ITBs are more sensitive to HFS- than to LFS-launched pellets because, in the former case, the ∇B -induced drift yields an effective matter deposition beyond the radius of maximum pellet penetration. However, encouraging results were obtained with HFS-launched pellets showing that, if the confinement barrier is temporarily suppressed, it recovers quickly while the density decays, figure 40. Nevertheless, substantial optimization remains to be done before this technique can be effectively used to fuel the ITB core [175]. In JT60-U, the injection of a pellet outside the ITB leads to an increase in the particle confinement in the plasma core. This enhancement is associated with a decrease in the density fluctuations that drop from $\delta n/n \sim 1\text{--}2\%$ during the pre-pellet phase down to 0.4–0.6% after the pellet injection [196].

6.2.2. Confinement and transport properties. A favourable condition for an ITB formation is the presence of a region of weak or negative magnetic shear in the plasma core. This requires a broad or hollow current profile that—in the case of a pellet-induced ITB—is achieved by generating a large bootstrap current driven in an off-axis location by the pressure gradient. In early experiments, with no plasma preheating, essentially the bootstrap current resulting from the pellet-induced density peaking modified the q -profile. The achievement of a PEP-phase was therefore facilitated when the pellet was injected during the current ramp-up or when the target plasma exhibited a central safety factor $q_0 \geq 1$ [90, 182] (PEP-modes with $q_0 \leq 1$ were only reported in JT60-U [185]). More recent experiments demonstrated that a region of negative central magnetic shear could be maintained during pellet injection and subsequent density peaking, opening the possibility of controlling independently the current and pressure profiles.

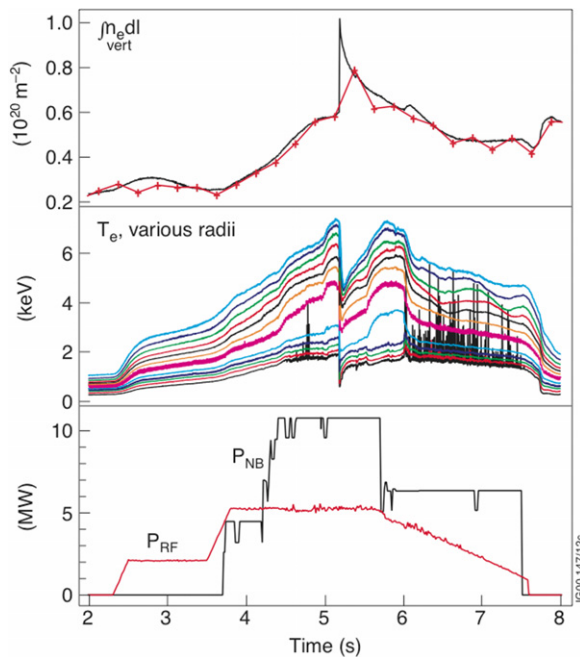


Figure 40. HFS pellet fuelling of an ITB plasma. (a) Line-integrated density, (b) electron temperature at different radii, (c) additional power. The confinement barrier is temporarily suppressed, probably due to large changes in the plasma edge. The ITB subsequently quickly recovers while the density decays, but the time duration of the applied power is not long enough to possibly benefit from an increase in the central density [175].

A significant drop in both the ion (χ_i) and electron (χ_e) thermal diffusivities is measured in the high-confinement core. In TFTR and JET (where the discharge centre can be in the second stability region [193]), both χ_e and χ_i are globally divided by a factor of ~ 2 [182, 184]. In DIII-D, they are measured to be close to their neoclassical value in the plasma core [90], figure 41. As a whole, the drop in the transport coefficients is interpreted to be due to the stabilization of both the electron and ion temperature gradient (ETG and ITG) modes by the density peaking [184, 191, 197]. However, in Tore Supra, an analysis in terms of drift wave stability showed that the peaked density profile is in general unable to justify on its own the improved core confinement and that an increase in the $E_r \times B$ velocity shear and a lowering of the magnetic shear (with optimum for $s \sim -0.5$) are required to explain the low values of the transport coefficients [187], figure 42. Globally, this interpretation agrees with measurements: in TFTR, there is no reversed magnetic shear ($s \geq 0$) but the density profile is strongly peaked ($n_0/\langle n \rangle \geq 5$) and the $E_r \times B$ velocity shear important and, in JET, the shear reversal remains moderate in the plasma core $0 \leq s \leq -0.5$. Owing to the limited volume enclosed by the ITB ($\sim 25\%$ of the total plasma volume [193]), and despite the low values of the transport coefficients reported above, the global confinement enhancement remains moderate: $H_{89L} \times 1.4$ in TFTR, and from 1 to 4 in JET, with an average value of ~ 2 [182, 184]. In what concerns the difficulties encountered up to now for fuelling the core of ITB plasmas, they are interpreted to be due to the reduction of the zonal flows and of their shearing rate consecutively to the injection of the pellet. This could explain the different response of the barrier to the pellet deposition profile and the loss of the ITB for a deep enough penetration [195].

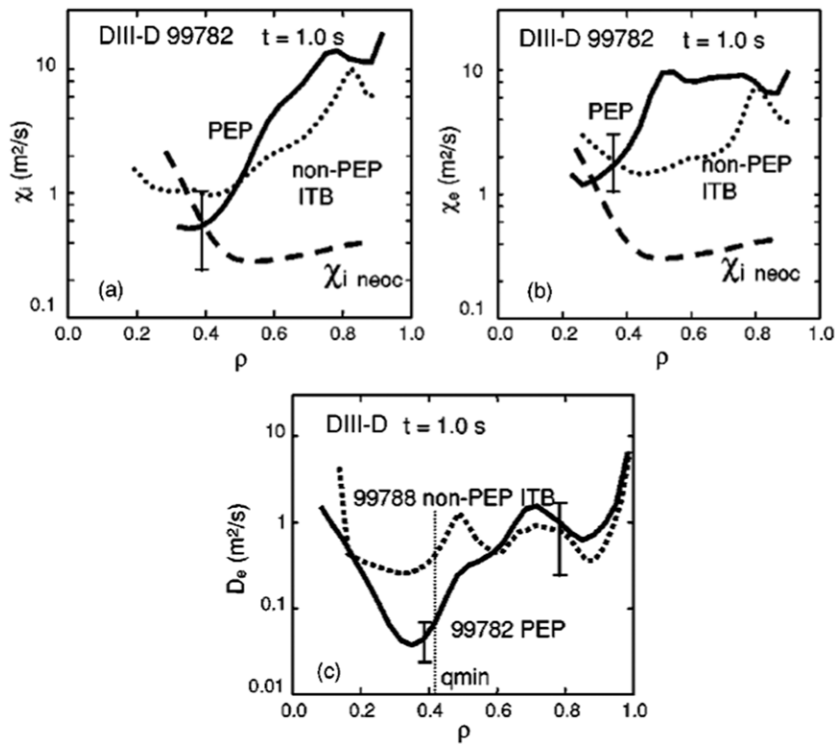


Figure 41. Transport analysis results for a PEP-mode discharge (full line) with a non-PEP ITB comparison discharge (dotted line) in DIII-D, showing (a) the ion thermal diffusivity, (b) the electron thermal diffusivity and (c) the electron particle diffusivity [90].

6.3. Other regimes and confinement devices

6.3.1. Other confinement regimes The deep fuelling associated with pellet injection leads in most cases to a beneficial transient change in the particle and energy transport. Numerous experiments are reported in a number of machines and with various target plasmas, which are briefly reviewed below.

In FTU, an important experimental activity was devoted to high-density operation (see [198] for a general review). It was found that—in pellet-fuelled discharges—the possibility of triggering a high-confinement phase depends on the pellet penetration and target plasma parameters (density, temperature and edge safety factor q_a). In low-density, high-temperature, high- q_a discharges, with peripheral pellet penetration, the temperature does not recover its pre-injection value and sawtooth activity is suppressed. This leads to a rapid accumulation of impurities at the plasma centre (a pinch velocity two orders of magnitude larger than the neoclassical one is required to reproduce the measurements [199]) and then to a disruption. Oppositely, in low- q_a , high-density and moderate temperature discharges with deeper pellet penetration, the temperature recovers rapidly and sawtooth activity is only slowed down as long as the pellet remains outside the $q = 1$ flux surface. In this case, the density does not decrease after the pellet injection and both τ_E and the plasma energy content increase (the effective heat diffusivity falls to ~ 0.2 m² s⁻¹). The high-performance phase can be maintained by the injection of 5 pellets separated by ~ 100 ms, with characteristics $H_{89p} \sim 1.3\text{--}1.5$, $nT\tau_E \sim (0.6\text{--}0.8) \times 10^{20}$ m⁻³ keV s⁻¹, and a neutron yield larger than 10¹³ s⁻¹ [190, 200].

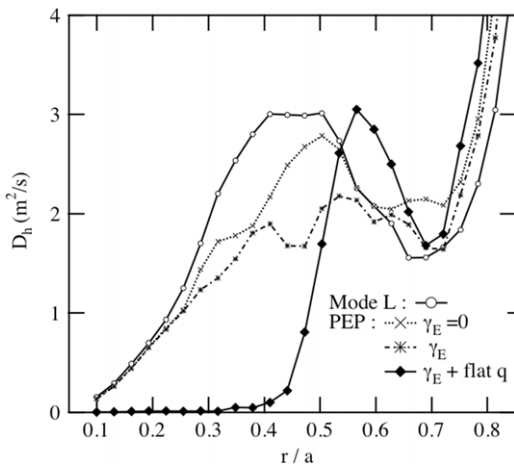


Figure 42. Heuristic diffusion parameter D_h (derived from the mixing length estimate), taking into account density peaking only ($\gamma_E = 0$), then density peaking and $E_r \times B$ shear (γ_E), and finally density peaking, $E_r \times B$ shear and flat current profile ($\gamma_E + \text{flat } q$) [187]. Since D_h does not account for non-linear effects, it cannot be compared directly with experimental values of anomalous diffusivities. It is nevertheless well suited to comparing different situations, such as PEP- and L-modes, or to doing a parametric analysis, as is the case here.

From the analysis of the above experiments, it appears that a thorough conditioning of the wall (titanization then boronization) and the presence of the $q = 1$ flux surface in the plasma are required conditions to trigger an improved confinement phase because they allow to maintain a sawtooth activity and to avoid impurity accumulation [190]. In some cases, the development of a snake can also prevent impurities from accumulating, but the confinement is degraded when it becomes too important [131]. As a function of the fuelling method, it was observed that when using conventional gas puff, the energy confinement time saturates at ~ 50 ms as soon as $n \sim 0.5 \times n_{GR}$. In both LFS and VHFS pellet-fuelled discharges, see figure 43, the neo-Alcator scaling is recovered up to $n \sim n_{GR}$, and the ion heat diffusivity falls to its neoclassical value, leading to a higher saturation of the confinement at $\tau_E \sim 100\text{--}120$ ms ($H_{97L} \sim 1.3$) [93, 201, 202]. These experiments were analysed with the gyrokinetic codes Kinezero and GS2 to determine the effects of pellet injection on electrostatic turbulence. It was shown that density peaking is systematically stabilizing only when ion modes only or electron modes only are unstable, i.e. at low wavelength, when trapped electron modes (TEMs) are stabilized by collisions. This is the case in FTU plasmas where the collisionality is high enough to detrap most of the electrons. The low-wavelength unstable modes remaining are then pure ion temperature gradient (ITG) modes that are stabilized by the more peaked density profiles of pellet-fuelled plasmas. In the post-pellet phase, the density peaking stabilizes also strongly the high-wavelength electron temperature gradient (ETG) modes [197].

In HL-1M, experiments aiming at characterizing the behaviour of particle transport with the fuelling method showed that both the density peaking and particle confinement time τ_p are increasing with fuelling efficiency: from $n_0/\langle n \rangle \sim 1.3\text{--}1.5$ and $\tau_p \sim 5$ ms when using conventional gas puff to $n_0/\langle n \rangle \sim 2\text{--}2.3$ and $\tau_p \sim 60$ ms with pellet injection [203]. On the same machine, quasi-stationary, high-density discharges (up to $n \sim n_{GR}$) were obtained with multiple pellet injection (up to 8 consecutive pellets) and a thorough conditioning of the first wall (siliconization, then He-glow discharges), which showed no significant confinement degradation [98, 204]. Similar measurements were made in TEXTOR-94, HT-7 and HT-6M

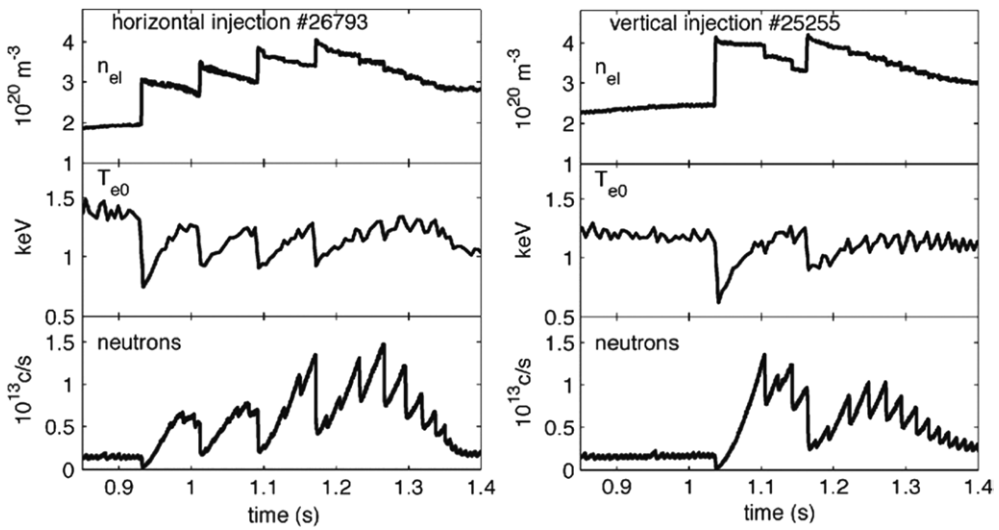


Figure 43. Comparison of high performance phases (multiple PEP-modes) achieved in FTU with LFS (#26793) and VHFS (#25255) pellet injection. Plasma parameters are $B = 7.2\text{ T}$ and $I_p = 1.1\text{ MA}$. n_{el} refers to the line averaged density. (top) Average density, (middle) central electron temperature, (bottom) neutron yield [201].

with different target plasma parameters and heating scenarios, showing a phase of improved confinement after the injection of a pellet. Typically, this phase lasts $(2\text{--}3) \times \tau_E$ and is characterized by an increase in both the density peaking (by 30–50%) and energy confinement time (by $\sim 20\text{--}40\%$) [23, 78, 205–211]. In START, a transient improvement of the confinement was observed ($\tau_E \times 1.3$ during $\sim 0.7 \times \tau_E$) after the injection of a pellet from the VHFS in a high- β , high-density discharge ($\beta_T \sim 27\%$, $n \sim n_{GR}$) [150].

Both an increase in the density peaking and an enhancement of the confinement were obtained in T10 after the injection of a deuterium pellet in an ECRH plasma [188]. In these experiments, although the pellet ablation remains peripheral (outside $\rho/a \sim 0.7$), both the core temperature and the density peaking increase in $\sim 100\text{ }\mu\text{s}$, i.e. typically 1% of the resistive time. Then, the line-integrated density recovers its pre-injection value, but the peaking persists and the plasma temperature remains high ($T_i \times 1.3$ and $T_e \times 1.2\text{--}1.3$). Such discharges display an ohmic-like scaling of the confinement that is typically 60% higher than in similar ECRH plasmas with no pellet injection.

In TEXTOR-94, in strongly heated RI mode plasmas [212], a phase of improved confinement of long duration is observed with pellet fuelling, figure 44. The time-history of the main plasma parameters is the following. Immediately after the pellet injection, about 50% of the deposited material is ejected in a short time interval of $\sim 20\text{ ms}$. Then the density increases slowly inside the $q = 3/2$ flux surface, when the current and temperature profiles remain unchanged (except—for the temperature—during a short transient just after pellet injection). In such discharges, the confinement is similar to that of an ELM-free H-mode and is maintained as long as additional power is applied. The end of the enhanced confinement phase is triggered by the onset of a MARFE or by the increase in the neutral density at the edge in the case of multiple pellet injection. The most likely explanation is that the injected pellet does not create a new plasma mode of improved confinement but that it continues the RI mode to the upper limit, the density peaking allowing the stabilization of ITG modes deeper in the plasma core [213].

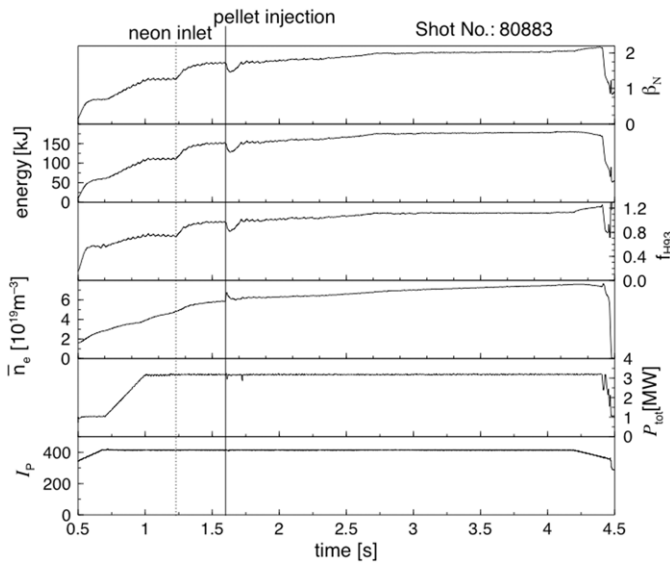


Figure 44. Example of an RI mode discharge in TEXTOR-94 with a long and stationary high-confinement phase (saturated at high β_N) triggered by a pellet. From top to bottom: normalized β_N , stored energy, confinement enhancement factor H_{93} , average density, total power coupled to the plasma current [213].

6.3.2. Stellarators and reversed field pinches. Pellets were also demonstrated to have beneficial effects in confinement devices other than tokamaks. In LHD, with pellet fuelling, the operational domain was extended up to average densities $\sim 8 \times 10^{19} \text{ m}^{-3}$ without a significant confinement drop when, with conventional gas puff, the confinement is degraded as soon as $\langle n \rangle$ reaches $3.5 \times 10^{19} \text{ m}^{-3}$ and the limit in density is $\sim 5 \times 10^{19} \text{ m}^{-3}$. Also, higher volume-averaged β_T -values were obtained with pellet fuelling [33, 214]. However, in such discharges exhibiting a peaked density profile, the stiffness of the pressure profile coincides with a higher electron heat diffusivity [215]. On the route toward steady-state, quasi-stationary operation ($\langle n \rangle \sim 8 \times 10^{19} \text{ m}^{-3}$, $T_e \sim T_i \sim 1 \text{ keV}$ with 4 MW NBI) was achieved by using 10 Hz repetitive pellet injection with relatively shallow penetration, showing a confinement equal to that obtained transiently in the high-performance phase following a nearly central pellet injection [216]. In local island ($m/n = 1/1$) divertor (LID) discharges, the injection of 6 to 10 pellets triggered the development of a stable super-dense core with a density as high as $4.6 \times 10^{20} \text{ m}^{-3}$ and a temperature of $\sim 0.85 \text{ keV}$. The core is maintained by an ITB with a very high-density gradient, the base of which is close to the radius of zero magnetic shear [217, 218], figure 45. A transient enhancement of the confinement following the injection of a pellet was also observed in L-mode plasmas in Heliotron-E [219].

Pellet injection experiments were also performed in the RFX reversed field pinch, showing a more contrasting situation. In standard discharges, if no deleterious effect is observed when the ablation remains peripheral, a pellet penetrating up to the plasma core triggers a dynamo relaxation event (DRE) that is the cause of a brutal confinement drop. In improved confinement regime (pulsed poloidal current drive—PPCD²), a synergy between pellet injection and PPCD

² PPCD is a technique to stabilize the internally resonant tearing modes responsible for magnetic field stochasticization and transport in the RFP core [221].

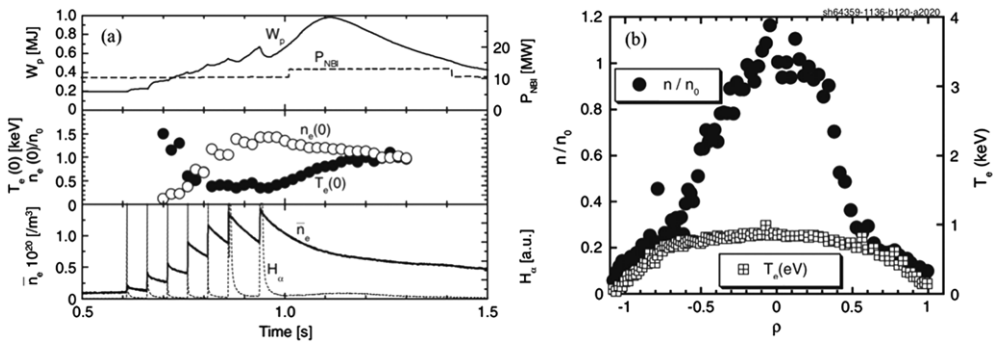


Figure 45. (a) Time evolution of the plasma parameters for super-dense core (SDC) plasma operation in LHD. (top) Stored energy and additional power, (middle) central temperature and peaking factor, (bottom) averaged density and H α signal. (b) Density and temperature profiles for a 10 MW SDC discharge [217].

is observed when the effect of the latter is strong enough and, in this case, plasma fuelling without dramatic confinement reduction is possible [220].

7. Pellets for plasma control

7.1. ELMs mitigation

Edge localized modes (ELMs) are instabilities typical for H-mode scenarios that result in large quasi-periodic heat and particle flows to the first wall and divertor target plates. Since the corresponding heat load is high enough to lead potentially to an important erosion of these plasma facing components (PFCs), an important experimental effort was devoted to ELMs mitigation. In many divertor tokamaks, it was observed that the product $f_{\text{ELM}}^0 \times \Delta W_{\text{ELM}}^0$ was constant, where f_{ELM}^0 is the intrinsic ELM frequency and ΔW_{ELM}^0 the energy loss per ELM. Since pellets are already known to trigger ELMs when injected during type-I ELMy H-mode phases [135–138], and provided the relation $f_{\text{ELM}} \times \Delta W_{\text{ELM}} = \text{Const}$ also holds for externally triggered ELMs, a further option for ELM mitigation is to increase f_{ELM} beyond f_{ELM}^0 to reduce the energy loss in the proportion $f_{\text{ELM}}^0/f_{\text{ELM}}$.

This technique was extensively investigated in ASDEX-U. First experiments were performed in discharges close to the L-H transition threshold and in which the intrinsic ELM frequency was $f_{\text{ELM}}^0 \sim 3$ Hz. Control was done with pellets launched at $v_p = 560$ m s⁻¹ from the HFS-72° injection line and a frequency $f_{\text{Pel}} = 19$ Hz [222]. These first experiments demonstrated the feasibility of external ELM control by continuous small pellet injection. Further experiments using smaller pellets at a higher injection frequency [223–227] showed that active triggering of ELMs requires a density perturbation in the gradient region about 1 cm inside the separatrix (measured at the horizontal midplane) and that the control is total as soon as $f_{\text{ELM}}/f_{\text{ELM}}^0 \geq 1.5$ (figure 46). It was established that, as far as the pedestal pressure, fluctuation spectrum or space-time heat flux distribution onto the divertor plates are concerned, the characteristics of an externally triggered ELM are indistinguishable from those of an intrinsic ELM for a given value of f_{ELM}^0 . Also, the confinement degradation was observed to be lower for externally triggered ELMs than for intrinsic ELMs (the energy content W_{MHD} scaling as $W_{\text{MHD}} \propto f_{\text{ELM}}^{-0.16}$ instead of as $W_{\text{MHD}} \propto f_{\text{ELM}}^{-0.6}$, figure 46). More quantitatively, it was shown that ΔW_{ELM} is reduced by 30–40% at fixed pedestal collisionality, while pellets only weakly enhance the ELM loss power $P_{\text{ELM}} = f_{\text{ELM}} \times \Delta W_{\text{ELM}}$, figure 47. As a whole, for

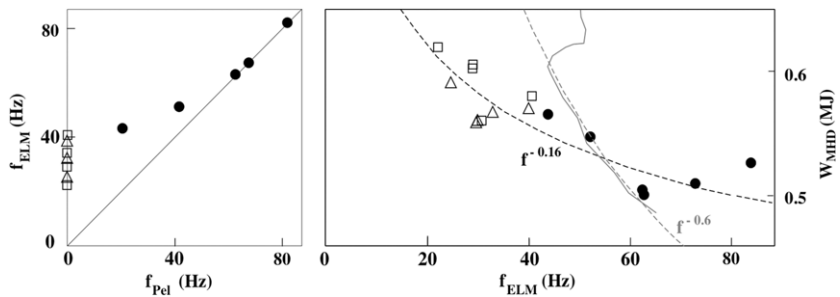


Figure 46. Demonstration of ELM control by pellets (left) and impact on confinement (right) in ASDEX-U. Data from pellet phases (full circles) and reference phases ($f_{\text{Pel}} = 0$) without (open squares) and with (open triangles) gas puffing. Pellet drive of f_{ELM} causes less confinement loss (black-dashed line) than rising f_{ELM}^0 by gas puff (grey solid, dashed lines: scaling expectation) [227].

constant edge particle source and pedestal parameters, the reduction in ΔW_{ELM} (with respect to ΔW_{ELM}^0) is balanced by the increased ELM frequency and pellet fuelling of the pedestal region.

In order to prepare ITER operation with a full tungsten first wall (see general review in [167]), an integrated exhaust scenario was developed in ASDEX-U providing simultaneous control of particle exhaust, time-averaged divertor heat flux and ELM losses via pace-making of the ELM frequency [228]. Feedback quantities were the divertor neutral flux and temperature (actuators: deuterium and argon injection rates) and the ELM frequency was stabilized at ~ 40 Hz by repetitive HFS injection of small pellets. This scenario was demonstrated to be fully compatible with the present tungsten wall coating, which constitutes about 65% of the area of the PFCs. A high value of f_{ELM} was shown to be necessary to avoid unstable situations with excursions of the radiation and impurity accumulation in the plasma core. Further improvements could be obtained by injecting smaller pellets (of particle content $\sim 10^{17}$ atoms) from the LFS, in order to decouple the fuelling and ELM pace-making systems [225].

7.2. Wall conditioning

Proper wall conditioning turned out to be an essential element to achieve high-performance in present day fusion devices, the main issues being to control the fuel recycling and the generation of impurities liberated by plasma–surface interaction [229]. Among the different methods developed up to now, in-flight conditioning by injection of Li-pellets was successfully tested in two machines equipped with a carbon-wall: DIII-D [230] and TFTR [231–234]. Owing to the relatively rapid erosion of the Li-coating, the conditioning procedure must take place immediately prior to—or during—the discharge in which the conditioning effect is desired. Two scenarios were used, consisting of conditioning the wall either before high-performance operation (up to four Li-pellets injected at the end of the preceding discharge in DIII-D [230], a series of ~ 10 ohmic discharges with two Li-pellets per discharge in TFTR [234]), or in conditioning the wall during the high-performance discharge itself (in TFTR, a pre-conditioning discharge with four Li-pellets, then up to two Li-pellets during the high-performance discharge itself, injected less than 1 s before NBI is switched on [233]). The same trend of the conditioning effect to increase with the plasma current was observed in both machines.

In DIII-D, the observed improvements were (i) the possibility of limiting in time the He-glow conditioning before each high-performance discharge, (ii) the reduction of the oxygen

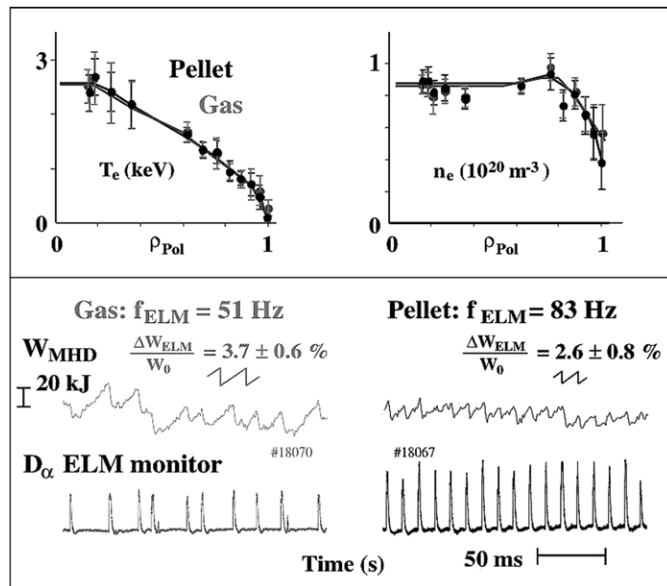


Figure 47. Plasma parameter matching of discharges with ELM control and gas puffing in ASDEX-U. Virtually identical global plasma parameters and n_e and T_e profiles (upper part) are obtained. However, there is a striking difference in the ELMing behaviour (lower part) with the pellet controlled frequency of 83 Hz beyond the ‘natural’ frequency of 51 Hz. Mitigation of the energy loss per ELM is obvious in the pellet case [227].

concentration in the plasma (but not of that of carbon) and (iii) the better reproducibility and average discharge performance. For long operation, the lithium appears to be uniformly distributed over the whole vacuum chamber, but it is rapidly eroded (on the time scale of one discharge) in the divertor region [230]. In TFTR supershot DT-campaigns, Li-conditioning led to (i) an increase in the energy confinement time (with τ_E reaching ~ 190 ms for pure deuterium plasmas, and up to 250–280 ms in DT, i.e. $\sim 40\%$ higher than in standard discharges), (ii) a higher density peaking and (iii) a decrease in the recycling and carbon influx, figures 48 and 49. The beneficial effect of Li-coating appears as soon as the first pellet is injected. It increases as long as additional lithium is deposited onto the limiter and lasts about ~ 10 discharges after the end of the injection [231–233].

Concerning metal-wall devices, an attempt was performed in Heliotron-E to reduce the plasma contamination by metallic impurities by Li-pellet injection, but no significant conditioning effect was observed although it was measured that the Li-coating survives ~ 1 –2 discharges after the end of the injection [235–237]. The same absence of effect was observed in ALCATOR-C Mod (first wall in molybdenum) and, globally, it seems that the good results obtained with Li-conditioning are only observed in carbon-wall machines [229].

7.3. Fast plasma termination

In a reactor grade device such as ITER, the implementation of a technique for fast plasma termination is required because, should there be a loss of control of the plasma equilibrium at high performance, the damage caused to first-wall materials could yield an unacceptable limitation to the lifetime of PFCs. Also, halo currents generated during the plasma current quench can lead to intense electromagnetic forces and locally impose considerable mechanical

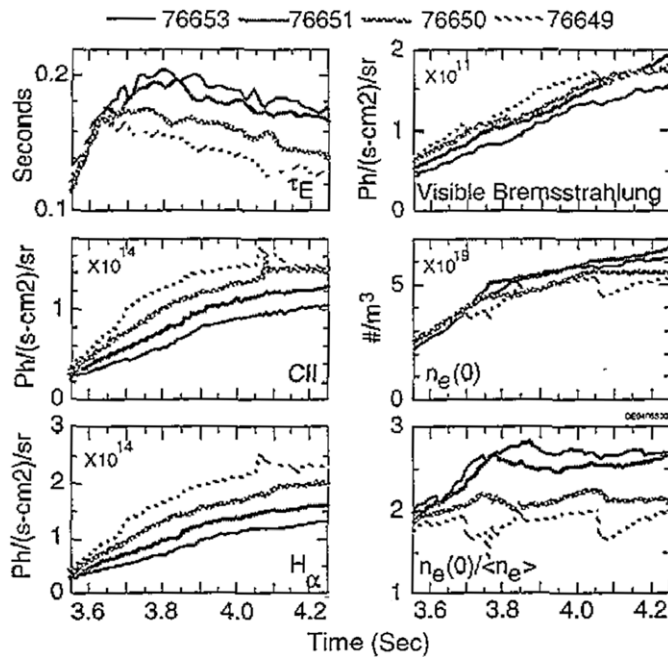


Figure 48. Time evolution of four TFTR plasmas each having 19.5 MW of NB-heating. Discharge 76649 has no Li-pellet. Discharge 76650 has one Li-pellet about 1 s before NBI, discharge 76651 has two Li-pellets about 1 s before NBI and discharge 76653 has two Li-pellets prior to NBI and was preceded by a four Li-pellet ohmic (pre-conditioning) shot. The data are energy confinement time, visible Bremsstrahlung emission, H_α light-hydrogen flux, CII light-carbon influx, central electron density and density peaking factor $n_e(0)/\langle n_e \rangle$. The beam injection begins at $t = 3.5$ s [233].

constraints to the machine structure. To minimize these undesirable effects, three factors must be simultaneously avoided or suppressed. They are the high-energy heat flux onto the divertor plates, the generation of halo currents and the acceleration of runaway electrons.

One of the possible methods for disruption mitigation is the injection of a ‘killer’-pellet of medium-Z impurity in order to radiate in a short time interval the quasi-totality of the plasma thermal energy and to limit accordingly the heat flux onto the divertor plates. Demonstration experiments were performed in JT60-U [238, 239], then in ASDEX-U, T-10 [240, 241] and DIII-D [242]. In this last machine, neon or argon pellets were injected, leading—on the scale of ablation (less than 1 ms)—to a threefold increase in the density, twofold in Z_{eff} (from 1.5 to 2.9) and to a decrease in the temperature from 2 keV to 50 eV. In the same time, between 50 and 100% of the plasma thermal energy was radiated, lowering considerably the heat load in the divertor [112, 242]. A similar trend is observed in the other devices [239–241], figure 50. The injection of a killer-pellet also allows reduction by $\sim 50\%$ of the intensity of halo currents as well as the associated mechanical loads [240, 242], figure 51. In JT60-U, vertical displacement events (VDEs)—and thus halo current generation—were totally avoided during the current quench by maintaining the plasma position close to the neutral point when injecting the killer-pellet [239]. The main drawback of the method is the generation of runaway electrons, as measured in DIII-D, T-10 and JT60-U [239, 242, 243]. The reason is the rapid cooling of the plasma that leads to the rise of large electric fields at the plasma edge just after the pellet is injected. In JT60-U, this was avoided by injecting up to three Ne-pellets and by heating the plasma by NBI during the current quench [239].

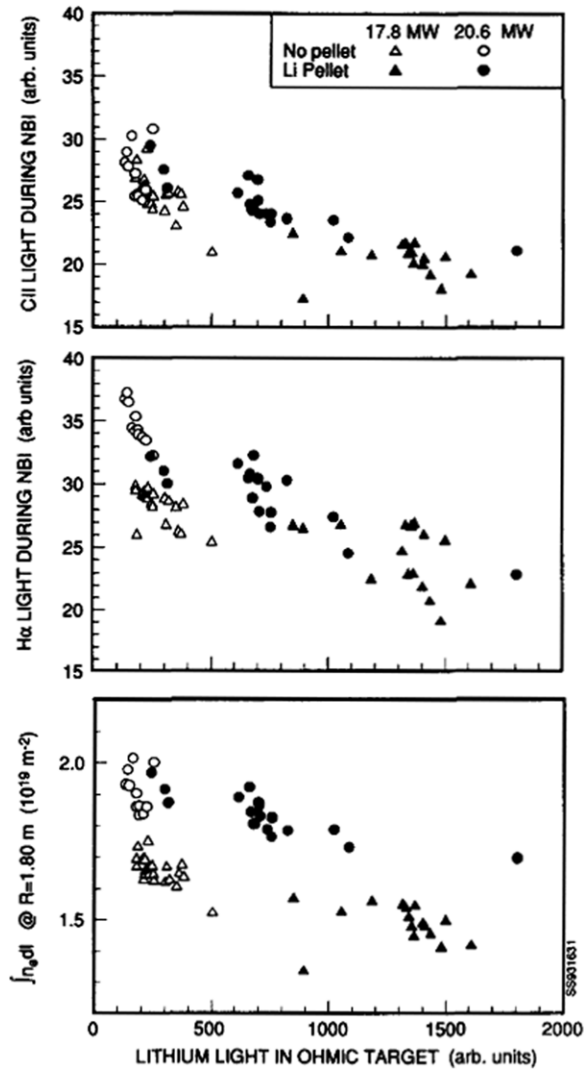


Figure 49. From top to bottom: the CII light, H α emission and edge line integral density during NBI plotted versus Li light in the ohmic phase during TFTR DT-experiments [232].

In the case of ITER-like plasmas, a scenario was proposed that consists of injecting a train of $\sim 30\text{--}50$ deuterium pellets doped with a high-Z impurity (few 10^{-6} of krypton) and of ramping down in ~ 4 s the pre-programmed currents in the poloidal field coils, but keeping the vertical and radial control feedback systems turned on [244]. Another technique allowing a plasma termination on a shorter time scale consists of injecting an $r_p = 5$ mm Kr-pellet (8×10^{21} atoms) that, injected at $\sim 3\text{--}4 \text{ km s}^{-1}$, can penetrate up to half the minor radius. Following the presented calculation, the plasma energy content is radiated in ~ 80 ms, with a maximum heat load on the divertor of $100\text{--}300 \text{ MW m}^{-2}$ during ~ 10 ms, insufficient to cause serious damage to the PFCs [245]. In both cases, no significant runaway population is generated.

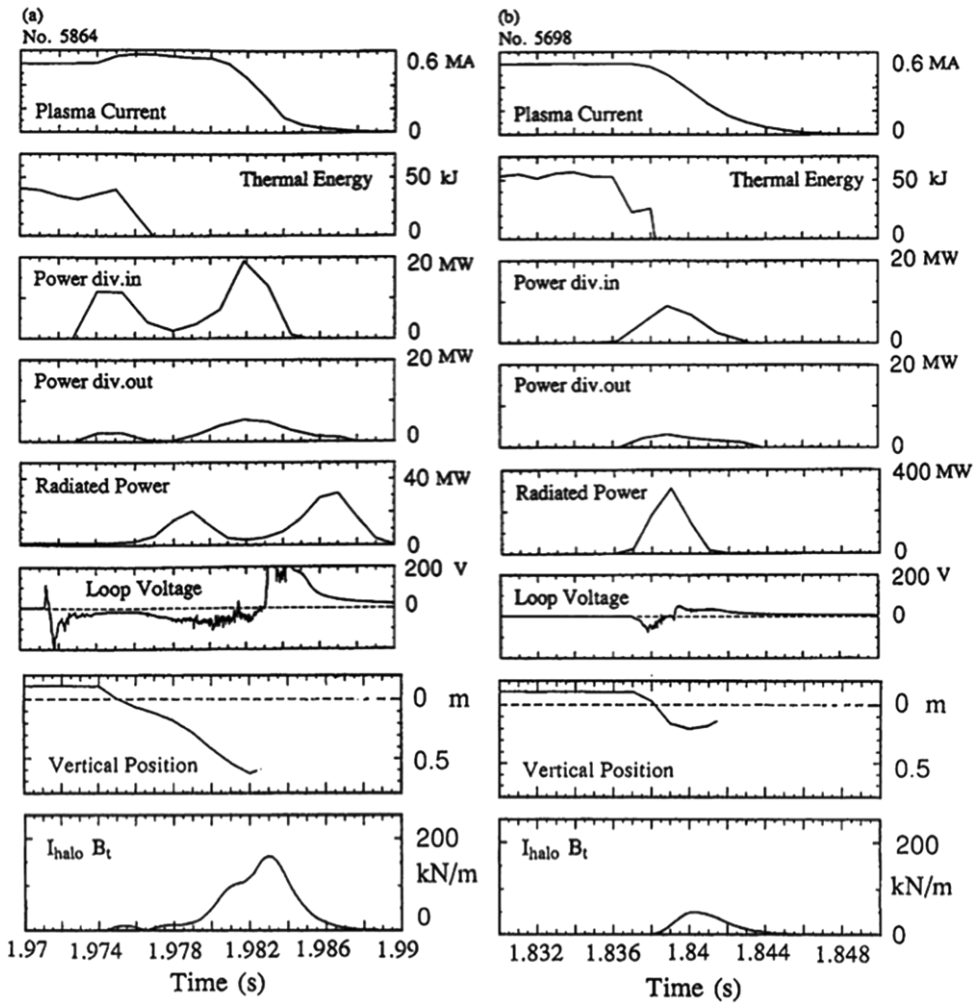


Figure 50. Time histories of the plasma current, plasma thermal energy, power deposition on inner and outer divertor plates, radiated power, loop voltage, vertical position of the plasma current centre and product of the total halo current by the magnetic field in ASDEX-U for (a) a density limit disruption in an ohmic plasma (shot 5864) and (b) a disruption in an ohmic plasma following the injection of a Ne-pellet at $t = 1.8356$ s (shot 5698) [240].

8. Pellets for diagnostic purpose

The relaxation of the density and temperature profiles consecutively to the injection of a pellet, the ablation characteristics ($H\alpha$ emission, deflection of the pellet trajectory) or even the neutral source represented by the ablation cloud were sometimes used as a diagnostic means of the plasma, mainly in what concerns the physics of particle or heat transport, the current density profile or the distribution of fusion-born α -particles during DT experiments.

8.1. Heat and particle transport

An original method for characterizing impurity transport was developed in CHS and LHD [246–249]. It is based on the analysis of the behaviour of a localized particle source of

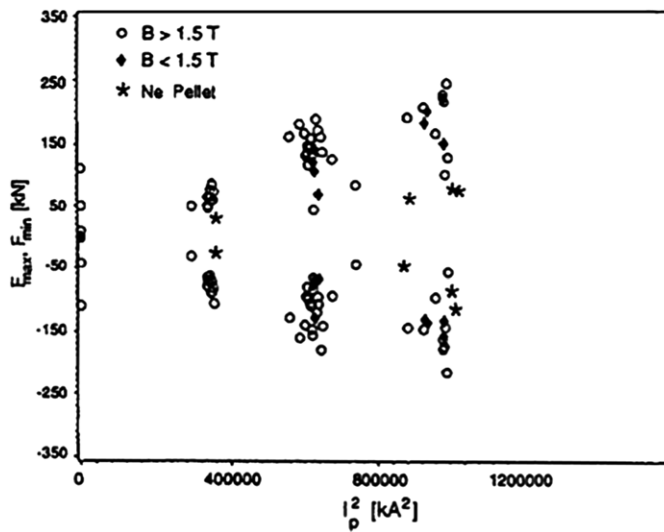


Figure 51. Maximal upward and downward vertical forces at the vessel suspension rods for disruptions during current flat-top with and without injection of Ne-pellets in ASDEX-U [240].

impurity ions as a tracer, deposited in a small volume in the plasma core. The tracer-encapsulated solid pellet (TESPEL) technique consists of launching a small composite pellet made of an outer shell of polystyrene in which an inner core of lithium hydride or titanium is embedded. The tracer particles (originating from the core of TESPEL) are locally deposited on a radial interval of 1–3 cm and immediately ionized and heated by the bulk electrons and ions. They first expand along the field lines, then fill up the magnetic flux surface and diffuse radially outward or inward, depending on the relative magnitudes of the diffusion coefficient and pinch velocity. This motion of the tracer particles is measured by charge exchange recombination spectroscopy (CXRS) in the case of a LiH-core and NBI heated plasmas, or by the observation of the Ti-K α and Ti-XIX emission lines in the case of a Ti-core, figure 52. In CHS, both the impurity diffusion coefficient profile and the typical value of the pinch velocity were obtained by this technique [247]. In LHD hydrogen discharges, where intrinsic metallic impurity accumulation is observed in a narrow density window ($(2\text{--}3) \times 10^{19} \text{ m}^{-3}$), the behaviour of the TESPEL tracer particles shows a long confinement time and an inward convection in the impurity accumulation window, consistent with that of intrinsic impurities [248]. Finally, in the same device, the impurity transport and recycling were characterized by modelling the behaviour of Bremsstrahlung radiation consecutively to the injection of pellets of different materials (C, Al, Ti, Mo) [250–252]. It was found that Al and Ti do not recycle, when the recycling coefficient and transport characteristics of carbon change with the working gas (H or He), in agreement with neoclassical scaling.

Concerning the main ion, the post-pellet relaxation of the density profile can hardly be used for a direct determination of its transport characteristics since, in a number of cases, the injection of a pellet leads to a change in the transport regime, see section 6.2. However, fitting the density behaviour can be a discriminatory test for transport models. Such a study was done in JET [253], showing that sawtooth activity is the main mechanism for particle transport in the plasma core ($\rho/a \sim 0.5$) but that an anomalous pinch is necessary to reproduce the density profile in the gradient zone ($0.5 \leq r/a \leq 0.9$), at least for L-mode plasmas. This anomalous convective flux was shown to be well reproduced by the off-diagonal elements of the transport

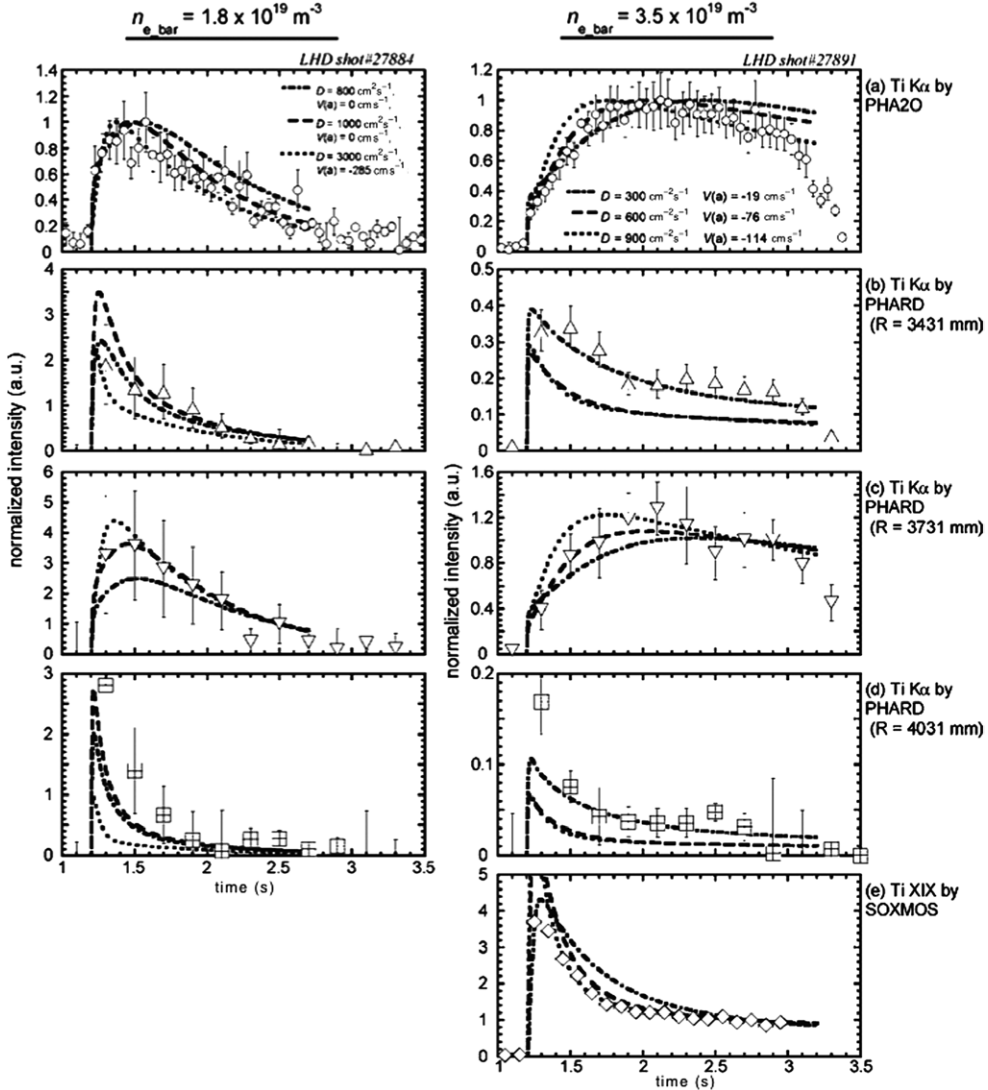


Figure 52. Comparison of normalized temporal evolution of the Ti- $\text{K}\alpha$ and Ti-XIX lines measured at different radial positions (open symbols) with those calculated by the MIST impurity transport code with several sets of diffusion coefficient D and pinch velocity V . Two density cases are considered: $\langle n_e \rangle = 1.8 \times 10^{19} \text{ m}^{-3}$ (left, LHD discharge #27884) and $\langle n_e \rangle = 3.5 \times 10^{19} \text{ m}^{-3}$ (right, LHD discharge #27891). Calculations are done with: (left) $D = 800 \text{ cm}^2 \text{s}^{-1}$ and $V = 0 \text{ cm s}^{-1}$ (dashed-dotted line), $D = 3000 \text{ cm}^2 \text{s}^{-1}$ and $V = 0 \text{ cm s}^{-1}$ (dashed line), $D = 1000 \text{ cm}^2 \text{s}^{-1}$ and $V = -285 \text{ cm s}^{-1}$ at the edge (dotted line). (right), $D = 300 \text{ cm}^2 \text{s}^{-1}$ and $V = -19 \text{ cm s}^{-1}$ (dashed-dotted line), $D = 600 \text{ cm}^2 \text{s}^{-1}$ and $V = -76 \text{ cm s}^{-1}$ (dashed line), $D = 900 \text{ cm}^2 \text{s}^{-1}$ and $V = -114 \text{ cm s}^{-1}$ (dotted line). For $\langle n_e \rangle = 1.8 \times 10^{19} \text{ m}^{-3}$, the best fit is obtained with $D = 1000 \text{ cm}^2 \text{s}^{-1}$ and $V = 0 \text{ cm s}^{-1}$, i.e. no convection. For $\langle n_e \rangle = 3.5 \times 10^{19} \text{ m}^{-3}$, a global agreement is obtained for $D = 300\text{--}900 \text{ cm}^2 \text{s}^{-1}$ and V from 19 to -114 cm s^{-1} [249].

matrix given by the Weiland's model [254]. In LHD, the analysis of the post-pellet density relaxation was used to characterize the improvement of confinement after wall conditioning by mixed $\text{CH}_4 + \text{H}_2$ gas puff discharges, showing a reduction of $\sim 60\%$ in the particle transport coefficient at $\rho/a \sim 0.5$ [255]. Finally, in FTU, pellet injection was used in conjunction

with other methods (gas puff modulation, current ramp-up) to determine the characteristics of particle transport as a function of the average density [256].

For heat transport studies, a widely used technique consists of injecting a shallow pellet and in analysing the propagation of the cooling wave into the plasma, figure 53. In JET, it was shown by this method that ITBs are regions of significantly reduced heat diffusivity, but that they are easily deteriorated by the propagation of the cold pulse that kills the weak ITBs and erodes the strong ones. Cold pulses in non-ITB low or reversed shear discharges indicate the existence of two regions in the plasma: an outer region where the transport appears to be stiff (fast cold pulse propagation) and an inner region associated with lower reversed magnetic shear where the transport appears to be greatly reduced (slow cold pulse propagation) [257]. Similar experiments were also performed in RTP and Tore Supra, showing in both cases the evidence of a non-local response of the plasma temperature to the edge perturbation [145, 146], see section 4.2. In LHD also, the TESPEL technique was used to determine the heat diffusivity inside a static magnetic island created artificially. The heat diffusivity χ_{\perp} inside/out of the island is determined from the analysis of the cold pulse characteristics (magnitude, propagation) depending on whether the TESPEL was injected at the O- or X-point of the magnetic island. It was found that the value of χ_{\perp} does not depend on the island size and is typically an order of magnitude lower inside the island than outside ($\sim(0.1\text{--}0.2)\text{ m}^2\text{ s}^{-1}$ instead of $\sim 1\text{--}2\text{ m}^2\text{ s}^{-1}$) [258]. Finally, in the TPE-RX reversed-field pinch, the perturbative electron heat diffusivity was determined from the propagation of a cold pulse generated by the injection of a pellet. It was found that χ_{\perp} follows the Rechester–Rosenbluth scaling and that the electron heat transport is ~ 3 times lower during the PPCD phase than in standard plasmas [259].

8.2. Current density profile

Three different methods were developed that aim at determining the current density or safety factor profile from pellet ablation characteristics. They use the striation spectrum, the tilt of the ablation cloud with respect to the toroidal direction or the deflection of the pellet trajectory.

The more obvious information that can be obtained on the q -profile from the ablation pattern is given by the conspicuous striation that appears quasi-systematically on the H α signal when the pellet crosses the $q = 1$ flux surface. It was used in HL-1M to estimate the current density on the magnetic axis from a parabolic approximation of the q -profile inside the $q = 1$ radius [260]. An attempt was made to develop the method further by associating each striation with a rational q -value, which would in principle allow an accurate identification of the safety factor profile [77]. Although—in TEXTOR-94—a good agreement was obtained in a few cases between the q -profile obtained by this technique and that resulting from equilibrium identification, it was not possible to fully validate the method and it is now abandoned [78].

Another technique, initially developed in TFR, T10 and TEXT [13, 261, 262], consists of measuring the tilt of the cigar-shaped ablation cloud with respect to the toroidal direction, i.e. the local direction of the magnetic field. The method is direct for plasmas of circular cross-section and it was used in HL-1M to determine the safety factor profile with an accuracy of $\sim 50\%$ [23]. More difficult is the case of plasmas with D-shaped cross-section. In this case, a detailed knowledge of the plasma geometry is required to calculate q from the inclination of the ablation cloud and an efficient procedure consists of constraining the equilibrium identification with the local measurements of the field geometry. This was done in ASDEX-U, using D₂, C and SiC pellets [105], the advantage of impurity pellets being that they allow a more accurate determination of the magnetic field direction because their ions can be observed farther in the parallel direction. Globally, it was found that introducing the measurement of the inclination

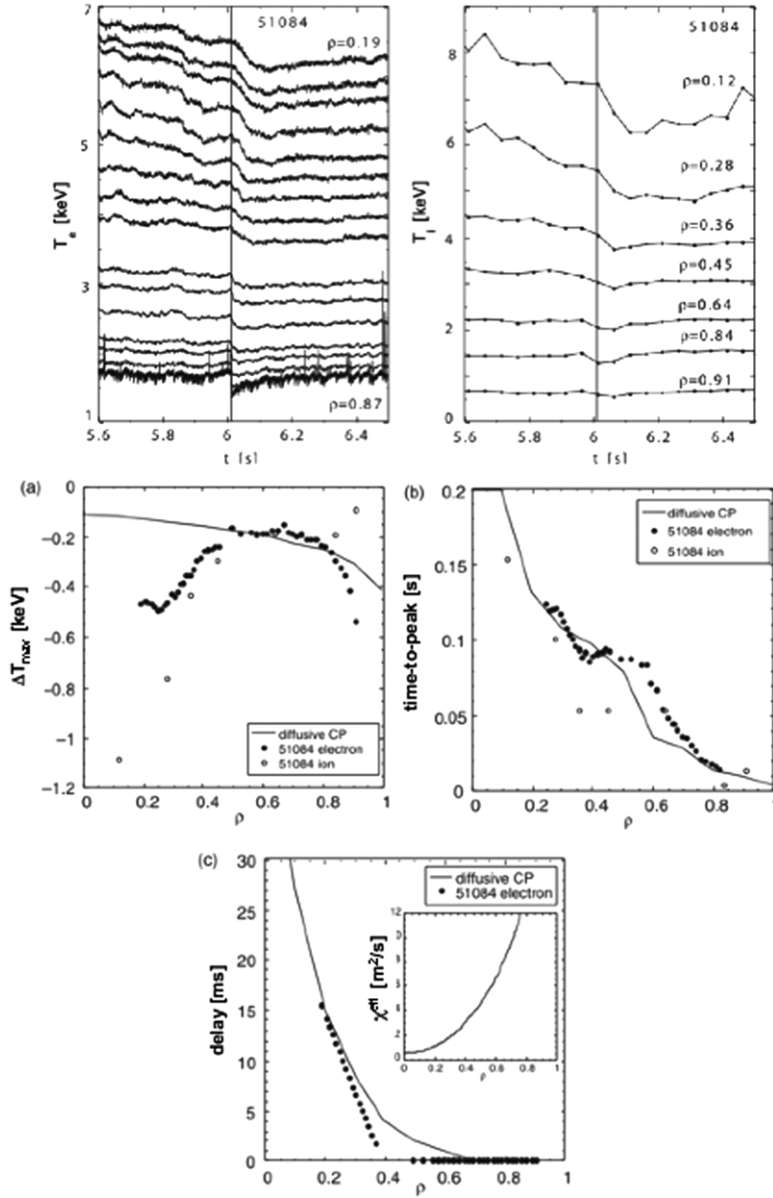


Figure 53. (top) Experimental time traces of electron and ion temperatures for a shallow pellet cold pulse ($t = 6.011$ s) in a non-ITB weakly reversed magnetic shear JET plasma. (bottom) Experimental (dots) and radial profiles for maximum cold pulse amplitude (a), (b) time-to-peak, (c) delay-time for electron (●) and ion (○) components. The line indicates the behaviour of a standard diffusive model assuming a heat diffusivity constant in time and equal to its power balance value (shown in the subplot of (c)) [257].

angle as additional data can improve the accuracy of the q -profile determination by up to $\sim 60\%$ in the plasma centre, figure 54.

The last method consists of analysing the deflection of the pellet trajectory. Indeed, owing to the asymmetry of the electron distribution function, the ablation is unbalanced on the co-

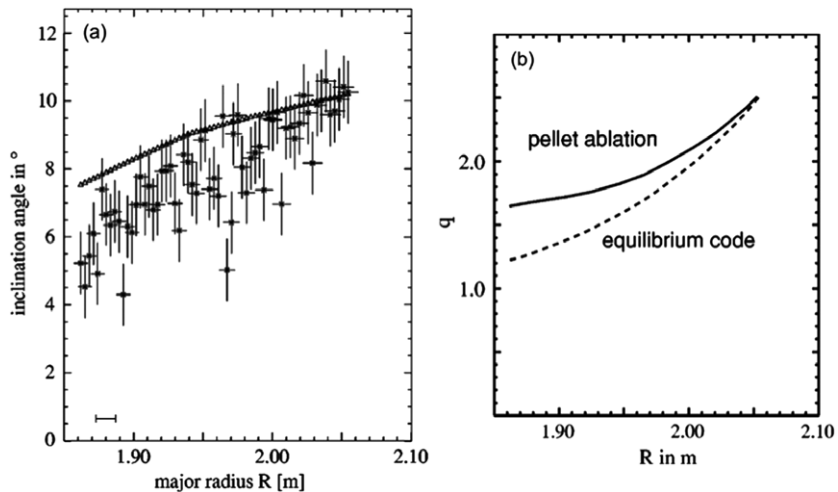


Figure 54. (a) Inclination angles determined by pellet observation (\times) compared with the results of the equilibrium code FPP (Δ). (b) Approximation of the q -profile determined by pellet ablation (solid line) compared with the q -profile determined by FPP calculation (dashed line) [105].

and counter-current sides of the pellet. The associated rocket effect results in an acceleration of the pellet–cloud system in the counter-current direction, see section 2.1.3. In T10, both hydrogen and carbon pellet were used [38, 39], and a comparison of the q -profiles determined from the deflection of the trajectory of a carbon pellet and from the tilt of the ablation cloud of a hydrogen pellet is presented in [263]. More details on the electron distribution were obtained in Tore Supra and RFX, figure 55. In the former, the perturbation of the pellet trajectory at the crossing of the $q = 1$ flux surface was analysed and it was shown that, just after a sawtooth crash, the quasi-rectilinear trajectory of the pellet inside $q = 1$ was compatible with an ergodization of the magnetic field draining the most energetic electrons outside the plasma core [37]—see figure 24. In the reversed field pinch RFX, the deflection of the pellet trajectory was used to diagnose the suprathermal electrons in the plasma. It was shown that the classical Spitzer–Härm distortion of the electron distribution function—consistent with the MHD dynamo electric field—allows to reproduce satisfactorily the pellet trajectory, when using an electron distribution function as predicted by the kinetic dynamo theory (KDT) leads to deflections larger than those measured [36].

8.3. α -population

The principle of the pellet charge exchange (PCX) diagnostic consists of injecting a light impurity pellet (boron or lithium) and of measuring the high-energy particles (T or α) escaping from the plasma after having experienced a charge exchange reaction with the neutrals of the ablation cloud [264–267]. Detailed calculations of the steady-state distribution of the α -particles and of their interaction with the cloud were performed [268, 269], showing in particular that, owing to the uncertainties on the cloud geometry and composition, their density cannot be measured absolutely. Nevertheless, the neutralized fraction was shown to be rather insensitive to the cloud characteristics above ~ 0.5 MeV, allowing an accurate determination of their energy distribution. This technique was used to diagnose the α -particles during TFTR DT-campaigns, giving information on their slowing down process, sensitivity to stochastic ripple diffusion

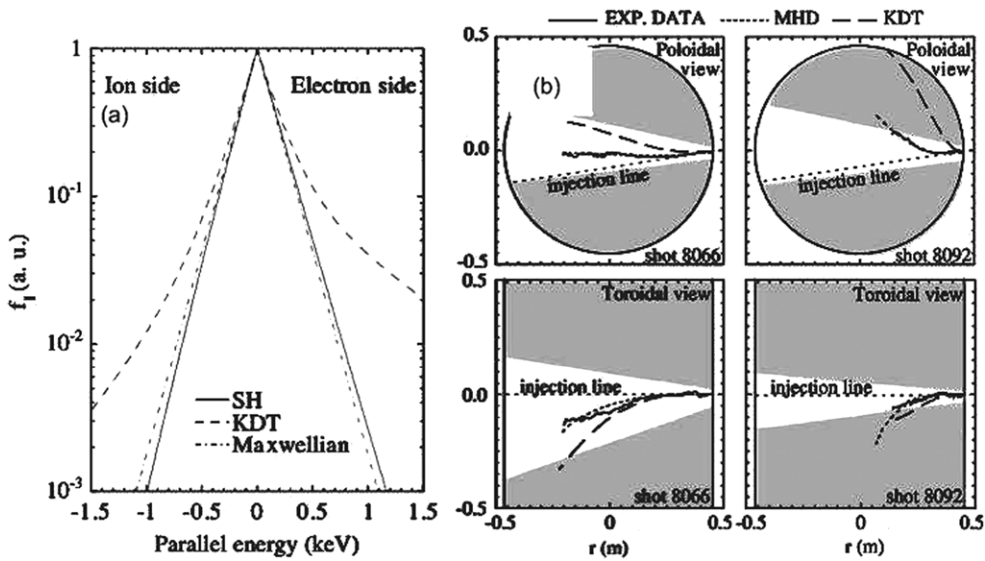


Figure 55. (a) Electron distribution function normalized to $f_{\parallel}(0)$ on the ion and electron sides of the pellet is shown for Spitzer–Härm and KDT modelling with local plasma parameters at $\rho/a = 0.75$ and compared with a Maxwellian distribution. (b) Comparison of experimental and simulated pellet trajectories for the RFX discharges #8066 and #8092. The shaded area is outside the H α detector field of view. The thick line is the first wall of the device [36].

and redistribution by sawtooth activity and toroidal Alfvén eigenmodes (TAEs) [270–272], figure 56.

Future devices will be characterized by a larger size and higher density and temperatures, making it more difficult to inject a pellet deep enough for relevant measurements. For instance, a $r_p = 1$ mm beryllium pellet injected at 4 km s^{-1} in ITER (corresponding to a density perturbation $\delta n/n \sim 8\%$) penetrates only at $\rho/a \sim 0.65$. A bigger pellet would penetrate deeper (up to $\rho/a \sim 0.15$ for $r_p = 2$ mm) but would lead to a much larger density perturbation ($\delta n/n \sim 60\%$), more demanding in terms of capability of the divertor to accept strong edge density perturbations. Two techniques were proposed to solve this problem. The first consists of injecting a deeply penetrating Be-pellet near the end of the discharge, and to avoid any concern about initiating a disruption by injecting subsequently a ‘killer’-pellet to benignly terminate the discharge a few milliseconds later. The second consists of injecting two ‘stacked’ pellets separated by a short time delay of $\sim 5\text{--}20$ ms, the first pellet producing a significant drop in the plasma electron temperature via radiation losses, thus allowing the second pellet to penetrate further. Also, owing to the increasing size of the devices and high-plasma density, it will be mandatory to correct the measured α ’s distribution for the energy-dependent fraction of neutrals that are re-ionized by the plasma electrons between the ablation cloud and the detector [273]. To overcome this difficulty, an alternative technique was proposed that consists of measuring the Doppler broadening of the He II ($\lambda = 468.6$ nm) line emitted by the α -particles having experienced a charge exchange reaction in the ablation cloud [274]. However, first measurements in TFTR show no difference between DD and DT plasmas.

9. ITER projections

Pellet fuelling is an essential feature of ITER operation because, owing to the thicker SOL in ITER than in present day machines, only a small fraction of the neutrals injected by

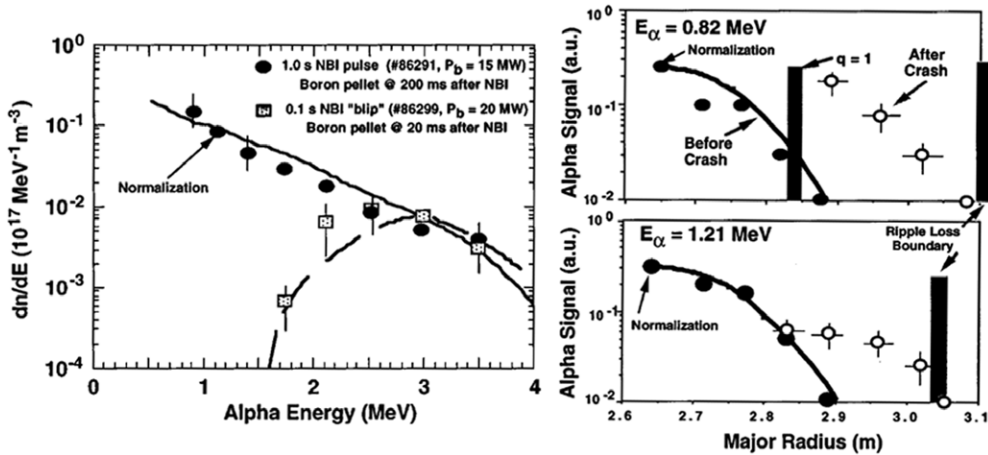


Figure 56. (left) Comparison of measured α energy spectra with simulation during the fully slowed down phase (circles and solid curve) and partly slowed down phase (squares and dashed curve). The agreement indicates that α -particles thermalize classically in the core of MHD quiescent supershot discharges. (right) In the presence of strong sawtooth activity, α -particles are depleted in the core and redistributed to well outside the $q = 1$ radius, but are not observed beyond the stochastic ripple loss boundary for the associated energy [271].

conventional gas puff can penetrate across the separatrix. It follows that a sufficiently high-pebble density ($n_{\text{ped}} \sim (7\text{--}9) \times 10^{19} \text{ m}^{-3}$) cannot be achieved with edge fuelling only—even assuming a particle diffusion coefficient as low as the neoclassical level—and that core fuelling is mandatory in ITER [275]. Calculations predict that, due to the ∇B -induced displacement, the material of a $r_p = 5 \text{ mm}$ pellets ($\delta n/n \sim 50\%$) injected from the HFS, with a velocity $v_p \sim 300 \text{ m s}^{-1}$, can be deposited beyond the pedestal region, up to $\rho/a \sim 0.85$, thus providing the required core fuelling [99], figure 57. Other arguments are that density limits in reactor grade plasmas are higher with pellet fuelling than with gas puff and that, all other parameters being equal, Q_{DT} can be higher and the ELM energy losses minimized in pellet-fuelled plasmas [276, 277]. This is partly due to the fact that this technique clearly separates the locations of the particle sources and sinks, opening the possibility of controlling independently the core and edge parameters: e.g. raising the central density to maintain a prescribed fusion power when keeping that at the separatrix below the density limits [278]. However, owing to the size of the device and the performance of present day injectors, it will be difficult to generate strongly peaked density profiles in ITER since a penetration up to $\rho/a \sim 0.3$ requires an injection velocity of several km s^{-1} , even for pellets representing a density perturbation as large as $\sim 50\%$ of the total plasma particle content [279]. Thereby, the use of pellets for controlling ITER plasmas requires the simultaneous satisfaction of two conflicting demands: namely, minimizing the density perturbation when maximizing the depth of the particle source.

As an example of closer discharge control, it was shown that pellets can be used as an actuator of the fusion power P_{fus} , provided their particle content is limited to $(1\text{--}2) \times 10^{20}$ atoms to avoid too large P_{fus} oscillations and their penetration is deeper than $\rho/a \sim 0.4\text{--}0.5$ [280], figure 58. Following [116], this would require injection velocities of $\sim 1.3 \text{ km s}^{-1}$ for pellets launched from the HFS, in the equatorial plane, and up to $4\text{--}5 \text{ km s}^{-1}$ in the case of VHFS injection, all performances beyond that of present day injectors. In addition, such deep penetrations are not necessarily compatible with advanced ITB-scenarios since it was demonstrated that if an ITB can survive a pellet injection if the latter is totally ablated at

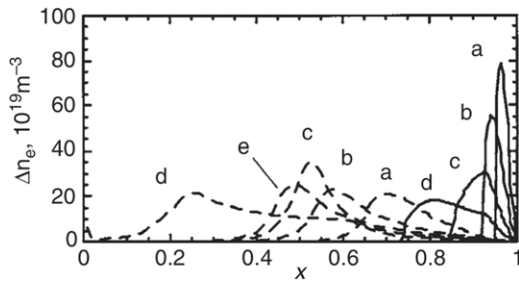


Figure 57. Model predictions for HFS injection in ITER. Solid and dashed lines are the ablation and the mass deposition profiles, respectively, x is the normalized radius. The pellet injection velocity is (a) $v_p = 100 \text{ m s}^{-1}$, (b) $v_p = 300 \text{ m s}^{-1}$, (c) $v_p = 1000 \text{ m s}^{-1}$ and (d) $v_p = 3000 \text{ m s}^{-1}$ for positive magnetic shear. Case (e) is for $v_p = 300 \text{ m s}^{-1}$ in a reversed magnetic shear configuration [99].

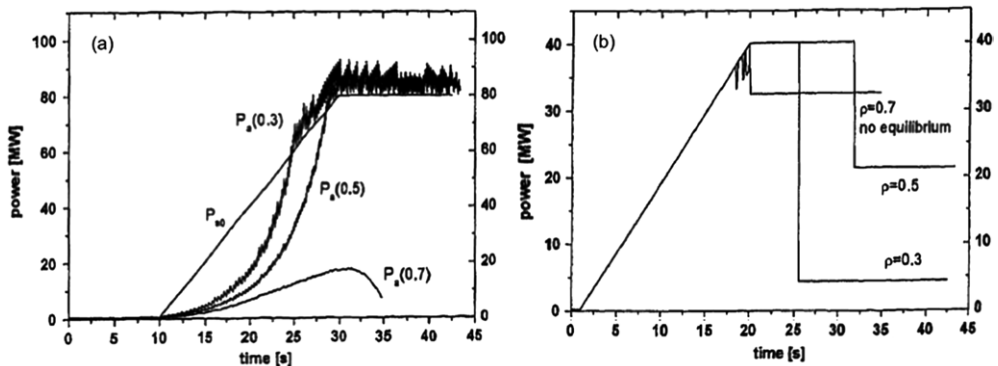


Figure 58. ITER-FEAT scenarios with pellets as actuators of the fusion power. (a) P_{a0} is the prescribed α -power, P_a (ρ_p/a) its actual value, where ρ_p/a is the radius of maximum pellet penetration. No equilibrium can be found for $\rho_p/a > 0.5$. (b) Required additional power for the three cases shown in (a) [280].

the plasma periphery, it is destroyed when the pellet penetrates inside the high confinement core [175, 194, 196], see section 6.2.1.

Polevoi and collaborators performed self-consistent transport simulations to assess the requirements for HFS pellet fuelling in different ITER scenarios. In the case of the reference inductive scenario ($P_{\text{fus}} \leq 500 \text{ MW}$, $n/n_{\text{GR}} \sim 0.85-0.9$, $Q_{\text{DT}} \geq 10$, $H_{\text{H98(y,2)}} \sim 1$, $I_p = 15 \text{ MA}$), it is shown that HFS injection of $r_p \leq 3.5 \text{ mm}$ pellets, at velocity $v_p \sim 500 \text{ m s}^{-1}$ and frequency $f_p \sim 4 \text{ Hz}$ ($\sim 85 \text{ Pa m}^3 \text{ s}^{-1}$) offers a possibility of operating with moderate ELM losses, high-energy multiplication factor $Q_{\text{DT}} \leq 20$ and power across the separatrix above the estimated H-L transition threshold [281, 282]. For the hybrid scenario ($n/n_{\text{GR}} \sim 0.9$, $Q_{\text{DT}} \geq 10$, $H_{\text{H98(y,2)}} \sim 1.2$, $I_p = 12 \text{ MA}$) and steady-state scenario ($n/n_{\text{GR}} \sim 0.8$, $Q_{\text{DT}} \geq 5$, $H_{\text{H98(y,2)}} > 1$, $I_p = 9 \text{ MA}$) with enhanced confinement, an extra core fuelling of the order of $\sim 20 \text{ Pa m}^3 \text{ s}^{-1}$ is needed to achieve the required performance. Two possible improvements are proposed. The first consists of using a separate system launching pellets from the LFS for the purpose of ELM control when the required pellet core fuelling is weak, the second in replacing—in the steady-state scenario—LHCD by NBI and electron cyclotron current drive to avoid the reduction of LHCD efficiency owing to the pellet-induced oscillation of the edge

density. This would allow extension of the range of stable operation when maintaining a high confinement, up to $H_{H98(y,2)} \sim 1.7$ [282].

In the present status of the design, the ITER fuelling system is planned for discharges lasting up to 3000 s, with a capacity to deliver $400 \text{ Pa m}^3 \text{ s}^{-1}$ in conventional gas puff and $200 \text{ Pa m}^3 \text{ s}^{-1}$ in pellet injection ($\sim 120 \text{ Pa m}^3 \text{ s}^{-1}$ in D₂ or DT pellets and $\sim 90 \text{ Pa m}^3 \text{ s}^{-1}$ in T₂ pellets). The pellets, each of particle content $(1.25\text{--}6) \times 10^{21}$ atoms ($r_p = 1.5\text{--}2.5 \text{ mm}$), will be launched from the HFS, at a velocity of the order of 300 m s^{-1} [283]. As a whole, this performance meets the fuelling requirements listed above, although a more efficient plasma control would be possible if the injection velocity was higher. With conventional injectors, where pellets are accelerated before entering the guiding system, their velocity is limited to $\sim 300\text{--}500 \text{ m s}^{-1}$ by the stress experienced in the curved sections of the guide tube [284]. However, new acceleration schemes are developed, where the acceleration results from the vaporization of a composite 'pusher' medium attached behind the fuel pellet using millimetre-microwaves from MW-gyrotron sources. With such a method, pellets could be accelerated on a very short distance just before penetrating the vacuum chamber, allowing injection velocities up to $\sim 3 \text{ km s}^{-1}$ for HFS injection in ITER-like tokamaks [285].

10. Concluding remarks

Owing to significant progress during the last decade, pellet injection is nowadays a key technique for fuelling as well as controlling fusion plasmas. Concerning the fuelling itself, the most important finding is undoubtedly the demonstration that the discrepancy between the ablation profile and that of density increment is due to the drift of the ablated material down the magnetic field gradient. This drift originates in the charge separation that appears at the boundary of the homogenizing cloud as a result of the uncompensated vertical drift current. If the leading process is now well understood, the precise phenomenon responsible for the stopping of the drift before complete pressure equilibration is yet unidentified. Several candidates were proposed that are all originating in the tokamak magnetic configuration (rotational transform or magnetic shear). Although all of them reproduce satisfactorily the experiments in a limited number of cases, their extrapolation to ITER-like conditions is yet uncertain and remains an open question. The main consequence of such a drift is that the pellet material tends to be expelled out of the discharge or to penetrate deeper in the plasma depending on whether it is deposited on the low- or high-field side of the machine. Numerous experiments were performed that confirm the better performance obtained by injecting pellets from the high-field side: more efficient fuelling and lower confinement degradation with additional power, despite a limited injection velocity. In the domain of ablation, the database of cloud characteristics was extended for tokamaks as well as stellarators or reversed field pinches, and the differences in the ablation physics in these three devices analysed and globally understood. The relative importance of the different shielding mechanisms was quantified showing that the more efficient were the collisional energy losses of the plasma electrons in the dense cloud surrounding the pellet and the development of an electrostatic sheath at the cloud-plasma interface. If the predictions of available ablation models agree within a factor of ~ 2 with measured ablation rates in present day tokamaks, they can differ significantly for reactor grade conditions. The main reasons for this dispersion are the possible deformation of the pellet owing to the non-uniform pressure distribution at its surface, the cloud diamagnetism that can create a magnetic bubble and divert from the cloud a part of the incident heat flux and the funnelling of the ablatant in a narrow flux tube due to rapid heating of the cloud at the moment when the pellet enters the discharge. Presently, there is no model taking into account self-consistently all the mechanisms identified as playing a role in pellet ablation. It follows

that, although remarkable progress was made in the understanding of both ablation and drift physics, further work is needed to dispose of really reliable predictions of pellet penetration and deposition profile in ITER-like conditions.

With respect to conventional gas puff, the main advantage of feeding plasmas by pellet injection is the decoupling of edge and core parameters, namely the possibility of increasing the core density without changing the one at the edge. This allowed enlargement of the H-mode operational domain up to densities larger than the Greenwald limit. High-density high-confinement plasmas with performance close to the ITER requirements were achieved in high-triangularity and ELMMy H-mode discharges with optimized heating scenario, high-field side pellet fuelling and strong divertor pumping. When injected at the beginning of a discharge, pellets lower the L–H transition threshold (ohmic H-modes were obtained consecutively to the injection of a pellet) and, with an appropriated strategy, trigger an ITB in the case of nearly central penetration. In this last case, the high-confinement phase is due to the change in the density and current profiles that stabilize both the electron and ion temperature gradient turbulence in the plasma core. However, these high-performance scenarios are intrinsically transient because subsequent pellets destroy weak ITBs and weaken the strong ones. Up to now, no means was found for deep fuelling of ITB plasmas and—although encouraging results were obtained—maintaining them for a long time remains a challenging question.

Demonstration was also made that pellets are an efficient means for plasma control. Taking advantage of the fact that a pellet injected in an H-mode discharge triggers systematically an ELM and that—for a given machine—the average power loss due to ELMs is roughly constant whatever their frequency, pellet injection was successfully used to increase the ELM frequency and lower their magnitude. This technique was demonstrated to be compatible with high-performance scenarios, but still requires improvements for completely decoupling the edge control from the fuelling of the plasma core. Impurity pellets were also used to mitigate disruptions or in the case of fast plasma termination, yielding a significant drop of the heat load on the divertor plates and a lower mechanical stress due to halo currents on the machine structure. The main drawback of the technique is the generation of runaway electrons due to the rise of large electric fields during the thermal quench. Several methods were proposed to avoid this phenomenon.

It is now well recognized that, due to the opacity to neutrals of the scrape-off layer, pellet injection is mandatory for proper fuelling of ITER discharges. It must nevertheless meet conflicting requirements, as ensuring an efficient fuelling beyond the separatrix when minimizing the density perturbation. Although these constraints are strong, computations point out the capability of pellets to fuel the different scenarios envisaged for ITER with present day technology. However, a more complete control of the plasma would require higher injection velocities.

The domain now appears rather mature and, even if developments are underway in the different pending points underlined in the present review, the lone issue that remains widely open concerns tritium handling and the possibility of minimizing wall retention by pellet fuelling. The assessment of such an effect in long discharges is crucial and would help significantly in the route towards steady-state operation.

References

- [1] Kaufmann M 1986 *Plasma Phys. Control. Fusion* **28** 1341
- [2] Lengyel L L 1989 *Nucl. Fusion* **29** 325
- [3] Chang C T 1991 *Phys. Rep.* **4** 143
- [4] Nagami M 1993 *Nucl. Fusion* **33** 1583

- [5] Milora S L *et al* 1995 *Nucl. Fusion* **35** 657
- [6] Milora S L 1981 *J. Fusion Energy* **1** 15
- [7] Milora S L 1989 *J. Vac. Sci. Technol. A* **7** 925
- [8] Combs S K 1993 *Rev. Sci. Instrum.* **64** 1679
- [9] Chang C T *et al* 1980 *Nucl. Fusion* **20** 859
- [10] Parks P B and Turnbull R J 1978 *Phys. Fluids* **21** 1735
- [11] Thomas C E *et al* 1979 *Bull. Am. Phys. Soc.* **24** 1035
- [12] McNeill D H, Greene G J and Shuresko D D 1985 *Phys. Rev. Lett.* **55** 1398
- [13] TFR Group 1986 *Europhys. Lett.* **2** 267
- [14] Durst R D *et al* 1990 *Nucl. Fusion* **30** 3
- [15] McNeill D H *et al* 1991 *Phys. Fluids B* **3** 1994
- [16] Müller H W *et al* 1999 *Phys. Rev. Lett.* **83** 2199
- [17] Müller H W *et al* 2002 *Nucl. Fusion* **42** 301
- [18] Segeev I Yu, Kostryukov A Yu and Shibaev S A 1997 *Fusion Eng. Des.* **34–35** 323
- [19] Sakakita H *et al* 1997 *Fusion Eng. Des.* **34–35** 329
- [20] Kuteev B V, Kostryukov A Y and Bakhareva O A 2002 *Tech. Phys.* **47** 935
- [21] Bakos J S *et al* 1996 *IEEE Trans. Plasma Sci.* **24** 29
- [22] Canton A *et al* 2001 *Plasma Phys. Control. Fusion* **43** 225
- [23] Longwen Y *et al* 2002 *Nucl. Fusion* **42** 265
- [24] Pégoürié B *et al* 1993 *Nucl. Fusion* **33** 591
- [25] Houlberg W A *et al* 1992 *Nucl. Fusion* **32** 1951
- [26] Baylor L R *et al* 1997 *Nucl. Fusion* **37** 445
- [27] Garzotti L *et al* 1997 *Nucl. Fusion* **37** 1167
- [28] Pégoürié B *et al* 2005 *Plasma Phys. Control. Fusion* **47** 17
- [29] Ishizaki R *et al* 2004 *Phys. Plasmas* **11** 4064
- [30] Baldzuhn J *et al* 2004 *Fusion Sci. Technol.* **46** 348
- [31] Ledl L *et al* 2004 *Nucl. Fusion* **44** 600
- [32] Sakamoto R *et al* 2004 *Nucl. Fusion* **44** 624
- [33] Sakamoto R *et al* 2001 *Nucl. Fusion* **41** 381
- [34] Timokhin V M *et al* 2004 *Tech. Phys. Lett.* **30** 298
- [35] Spitzer L Jr and Härm R 1953 *Phys. Rev.* **89** 977
- [36] Garzotti L *et al* 2000 *Phys. Rev. Lett.* **84** 5532
- [37] Waller V *et al* 2003 *Phys. Rev. Lett.* **91** 205002
- [38] Egorov S M *et al* 1994 *Plasma Phys. Rep.* **20** 140
- [39] Sergeev V Yu and Polivaev D A 2001 *Fusion Eng. Des.* **34–35** 215
- [40] Kuteev B V and Kostryukov A Y 1999 *Tech. Phys. Lett.* **25** 606
- [41] Dnestrovski Y N and T-10 Team 2001 *Plasma Phys. Rep.* **27** 825
- [42] Morita S *et al* 2002 *Nucl. Fusion* **42** 876
- [43] Parks P B, Turnbull R J and Foster C A 1977 *Nucl. Fusion* **17** 539
- [44] Felber F S *et al* 1979 *Nucl. Fusion* **19** 1061
- [45] Parks P B *et al* 1994 *Nucl. Fusion* **34** 417
- [46] Kaufmann M *et al* 1986 *Nucl. Fusion* **26** 171
- [47] Houlberg W A, Milora S L and Attenberger S E 1988 *Nucl. Fusion* **28** 595
- [48] Lengyel L L 1989 *Nucl. Fusion* **29** 37
- [49] Nakamura Y *et al* 1992 *Nucl. Fusion* **32** 2229
- [50] MacAulay A K 1994 *Nucl. Fusion* **34** 43
- [51] Kuteev B V 1995 *Nucl. Fusion* **35** 431
- [52] Ishizaki R *et al* 2003 *J. Nucl. Mater.* **313–316** 579
- [53] Parks P B and Rosenbluth M N 1998 *Phys. Plasmas* **5** 1380
- [54] Samulyak R, Lu T and Parks P B 2007 *Nucl. Fusion* **47** 103
- [55] Lengyel L L and Spathis P N 1994 *Nucl. Fusion* **34** 675
- [56] Kristol G and Lengyel L L 1998 *Phys. Plasmas* **5** 315
- [57] Pégoürié B and Picchiottino J-M 1993 *Plasma Phys. Control. Fusion* **35** B157
- [58] Lengyel L L 1978 *Phys. Fluids* **21** 1945
- [59] Parks P B 1991 *Nucl. Fusion* **31** 1431
- [60] Rozhansky V A 1989 *Sov. J. Plasma Phys.* **15** 638
- [61] Lengyel L L, Rozhansky V A and Veselova I Yu 1996 *Nucl. Fusion* **36** 1679
- [62] Parks P B, Leffler J S and Fisher R K 1988 *Nucl. Fusion* **28** 477

- [63] Lengyel L L *et al* 1999 *Nucl. Fusion* **39** 791
[64] Morozov D Kh *et al* 2004 *Nucl. Fusion* **44** 252
[65] Rozhansky V A and Senichenkov I Yu 2005 *Plasma Phys. Rep.* **31** 993
[66] Senichenkov I Yu *et al* 2005 *J. Nucl. Mater.* **337–339** 446
[67] Deng B-Q *et al* 2004 *Chin. Phys. Lett.* **21** 276
[68] Baiquan D *et al* 2005 *Plasma Sci. Technol.* **7** 2615
[69] Wurden G A *et al* 1990 *Rev. Sci. Instrum.* **61** 3604
[70] Baldzuhn J, Sandmann W and W7-AS Team 1993 *Plasma Phys. Control. Fusion* **35** 1413
[71] Gill R D, Edwards A W and Weller A 1989 *Nucl. Fusion* **29** 821
[72] Pégourié B and Dubois M A 1990 *Nucl. Fusion* **30** 1575
[73] Mansfield D K *et al* 1993 *Nucl. Fusion* **33** 150
[74] Kocsis G *et al* 1999 *Plasma Phys. Control. Fusion* **41** 881
[75] Pégourié B and Dubois M A 1989 *Nucl. Fusion* **29** 745
[76] Drawin H-W and Dubois M A 1992 *Nucl. Fusion* **32** 1615
[77] Dubois M A *et al* 1992 *Nucl. Fusion* **32** 1935
[78] Finken K H *et al* 1997 *Plasma Phys. Control. Fusion* **39** A351
[79] Terry J L *et al* 1992 *Rev. Sci. Instrum.* **63** 5191
[80] Parks P B 1996 *Plasma Phys. Control. Fusion* **38** 571
Lengyel L L 1997 *Plasma Phys. Control. Fusion* **39** 647
[81] Terry J L *et al* 2004 *Rev. Sci. Instrum.* **75** 4196
[82] Mansfield D K *et al* 1991 *Phys. Rev. Lett.* **66** 3140
[83] Heidbrink W W *et al* 1987 *Nucl. Fusion* **27** 3
[84] Pégourié B and Picchianti J-M 1996 *Phys. Plasmas* **3** 4594
[85] Yamada H *et al* 2001 *Plasma Phys. Control. Fusion* **43** A55
[86] Hong W Y *et al* 1999 *J. Nucl. Mater.* **266–269** 542
[87] Hamada Y *et al* 1996 *Nucl. Fusion* **36** 1047
[88] Baylor R L *et al* 1992 *Nucl. Fusion* **32** 2177
[89] Baylor L R, Jernigan T C and Hsieh C 1998 *Fusion Technol.* **34** 425
[90] Baylor L R *et al* 2000 *Phys. Plasmas* **7** 1878
[91] deKloe J *et al* 1999 *Phys. Rev. Lett.* **82** 2685
[92] Takenaga H, JT-60 Team 2001 *Phys. Plasmas* **8** 2217
[93] Frigione D *et al* 2004 *Fusion Sci. Technol.* **45** 339
[94] Giovannozzi E *et al* 2005 *Nucl. Fusion* **45** 399
[95] Terranova D *et al* 2007 *Nucl. Fusion* **47** 288
[96] Tuccillo A A *et al* 2006 *Nucl. Fusion* **46** 214
[97] JET Team 2001 *Nucl. Fusion* **41** 189
[98] Liu Y *et al* 2002 *Fusion Sci. Technol.* **42** 94
[99] Polevoi A R and Shimada M 2001 *Plasma Phys. Control. Fusion* **43** 1525
[100] Kuteev B V *et al* 2003 *Tech. Phys. Lett.* **29** 302
[101] Parks P B, Sessions W D and Baylor L R 2000 *Phys. Plasmas* **7** 1968
[102] Rozhansky V A and Veselova I Yu 1994 *Nucl. Fusion* **34** 665
[103] Luciani J-F, Mora J-P and Virmont J 1983 *Phys. Rev. Lett.* **51** 1664
[104] Dong J-F, Wang S-Q and Li W-Z 2006 *Chin. Phys.* **15** 2368
[105] Müller H W *et al* 1997 *Rev. Sci. Instrum.* **68** 4051
[106] Veselova I Yu and Rozhansky V A 1991 *Sov. J. Plasma Phys.* **17** 817
[107] Rozhansky V, Veselova I and Voskoboinikov S 1995 *Plasma Phys. Control. Fusion* **37** 399
[108] Aiba N *et al* 2004 *J. Phys. Soc. Japan* **73** 364
[109] Strauss H R and Park W 1998 *Phys. Plasmas* **5** 2676
[110] Strauss H R *et al* 1999 *Nucl. Fusion* **39** 2069
[111] Strauss H R and Park W 2000 *Phys. Plasmas* **7** 250
[112] Whyte D G *et al* 1998 *Phys. Rev. Lett.* **81** 4392
[113] Parks P B *et al* 2005 *Phys. Rev. Lett.* **94** 125002
[114] Rozhansky V A *et al* 2004 *Plasma Phys. Control. Fusion* **46** 575
[115] Senichenkov I Yu *et al* 2006 *Nucl. Fusion* **46** 788
[116] Pégourié B *et al* 2007 *Nucl. Fusion* **47** 44
[117] Lang P T *et al* 1997 *Phys. Rev. Lett.* **79** 1487
[118] Baylor L R *et al* 2003 *J. Nucl. Mater.* **313–316** 530
[119] Kuteev B V *et al* 2006 *JETP Lett.* **84** 239

- [120] Volkov V V *et al* 1995 *Plasma Phys. Rep.* **21** 699
- [121] Buratti P *et al* 2004 *Fusion Sci. Technol.* **45** 350
- [122] Giovannozzi E *et al* 2004 *Nucl. Fusion* **44** 226
- [123] Annibaldi S V *et al* 2004 *Nucl. Fusion* **44** 12
- [124] da Cruz D F *et al* 1995 *Phys. Rev. Lett.* **75** 3685
- [125] Hogeweij G M D *et al* 1996 *Nucl. Fusion* **36** 535
- [126] Weller A *et al* 1987 *Phys. Rev. Lett.* **59** 2303
- [127] Hutchinson I H *et al* 1994 *Phys. Plasmas* **1** 1511
- [128] Pecquet A-L *et al* 1997 *Nucl. Fusion* **37** 451
- [129] Liqun H *et al* 2003 *Plasma Phys. Control. Fusion* **45** 349
- [130] Yi L *et al* 2004 *Plasma Phys. Control. Fusion* **46** 455
- [131] Alladio F *et al* 1993 *Plasma Phys. Control. Fusion* **35** B241
- [132] Wesson J A 1995 *Plasma Phys. Control. Fusion* **37** A337
- [133] Bécoulet M *et al* 2003 *Plasma Phys. Control. Fusion* **45** A93
- [134] Bécoulet M *et al* 2005 *J. Nucl. Mater.* **337–339** 677
- [135] Baylor L R *et al* 1999 *J. Nucl. Mater.* **266–269** 457
- [136] Baylor L R *et al* 2001 *J. Nucl. Mat.* **290–293** 398
- [137] Lang P T *et al* 1996 *Nucl. Fusion* **36** 1531
Lang P T *et al* 1997 *Nucl. Fusion* **37** 567
- [138] Kamada K and JT-60 Team 2001 *Nucl. Fusion* **41** 1311
- [139] Lang P T *et al* 2000 *Nucl. Fusion* **40** 245
- [140] Lang P T *et al* 2001 *J. Nucl. Mater.* **290–293** 374
- [141] Gruber O *et al* 2001 *Nucl. Fusion* **41** 1369
- [142] TFR Group 1987 *Nucl. Fusion* **27** 1975
- [143] Liu W and Talvard M 1994 *Nucl. Fusion* **34** 337
- [144] Galli P *et al* 1999 *Nucl. Fusion* **39** 1355
- [145] Gorini G *et al* 2000 *Plasma Phys. Control. Fusion* **42** A161
- [146] Zou X L *et al* 2000 *Plasma Phys. Control. Fusion* **42** 1067
- [147] Igamaki S *et al* 2006 *Plasma Phys. Control. Fusion* **48** A251
- [148] Kalmykov S G, Kuteev B V and Svoiskaya M L 1995 *Nucl. Fusion* **35** 795
- [149] Lang P T *et al* 2002 *Nucl. Fusion* **42** 388
- [150] Ribeiro C *et al* 2001 *Fusion Eng. Des.* **58–59** 319
- [151] Lang P T *et al* 2001 *Nucl. Fusion* **41** 1107
- [152] Banno T *et al* 1995 *J. Nucl. Mater.* **220–222** 478
- [153] Géraud A *et al* 2005 *J. Nucl. Mater.* **337–339** 485
- [154] Wagner F *et al* 1982 *Phys. Rev. Lett.* **49** 1408
- [155] Greenwald M *et al* 1988 *Nucl. Fusion* **28** 2199
- [156] Gohil P *et al* 2003 *Plasma Phys. Control. Fusion* **45** 601
- [157] Gohil P *et al* 2001 *Phys. Rev. Lett.* **86** 644
- [158] Rozhansky V A 2004 *Plasma Phys. Control. Fusion* **46** A1
- [159] Lebedev S V *et al* 1996 *Plasma Phys. Control. Fusion* **38** 1103
- [160] Takenaga H *et al* 2002 *Fusion Sci. Technol.* **42** 327
- [161] Yamamoto T and JT-60 Team 2003 *Fusion Eng. Des.* **66–68** 39
- [162] Kubo H and JT-60 Team 2002 *Phys. Plasmas* **9** 2127
- [163] Stober J K, Lang P T and Mertens V 2003 *Fusion Sci. Technol.* **44** 650
- [164] Lang P T *et al* 2002 *Plasma Phys. Control. Fusion* **44** 1919
- [165] Burrell K H *et al* 2002 *Plasma Phys. Control. Fusion* **44** A253
- [166] Suttrop S *et al* 2005 *Nucl. Fusion* **45** 721
- [167] Günter S *et al* 2005 *Nucl. Fusion* **45** S98
- [168] Baylor L R *et al* 2005 *J. Nucl. Mater.* **337–339** 535
- [169] Gohil P *et al* 2006 *Plasma Phys. Control. Fusion* **48** A45
- [170] Yoshino R, Itami K and Sakurai A 1995 *J. Nucl. Mater.* **220–222** 433
- [171] Ushigusa K and JT-60 Team 2001 *Fusion Technol.* **39** 315
- [172] Maingi R *et al* 1997 *Phys. Plasmas* **4** 1752
- [173] Gruber O *et al* 1999 *Nucl. Fusion* **39** 1321
- [174] Ongena J *et al* 2001 *Plasma Phys. Control. Fusion* **43** A11
- [175] JET Team 2001 *Nucl. Fusion* **41** 1327
- [176] Kamada Y *et al* 2002 *Plasma Phys. Control. Fusion* **44** A279

- [177] Onsga J *et al* 2004 *Nucl. Fusion* **44** 124
[178] Suttrop W *et al* 2002 *Phys. Plasmas* **9** 2103
[179] Challis C D 2004 *Plasma Phys. Control. Fusion* **46** B23
[180] Litaudon X 2006 *Plasma Phys. Control. Fusion* **48** A1
[181] JET Team 1988 *Plasma Phys. Control. Fusion* **30** 1467
[182] Smeulders P *et al* 1995 *Nucl. Fusion* **35** 225
[183] Takase Y *et al* 1997 *Phys. Plasmas* **4** 1647
[184] Baylor L R *et al* 1997 *Nucl. Fusion* **37** 127
[185] Yoshino R 1989 *Nucl. Fusion* **29** 2231
[186] Kamada Y, Yoshino R and Nagami M 1991 *Nucl. Fusion* **31** 23
[187] Maget P *et al* 1999 *Nucl. Fusion* **39** 949
[188] T-10 Team 2001 *Nucl. Fusion* **41** 1473
[189] Ossipenko M V and T-10 Team 2003 *Nucl. Fusion* **43** 1641
[190] Gormezano C *et al* 2004 *Fusion Sci. Technol.* **45** 303
[191] Ding X-T *et al* 2006 *Chin. Phys. Lett.* **23** 2502
[192] Takase Y *et al* 1996 *Plasma Phys. Control. Fusion* **38** 2215
[193] JET Team 1994 *Plasma Phys. Control. Fusion* **36** A23
[194] Garzotti L *et al* 2006 *Nucl. Fusion* **46** 73
[195] Frigione D *et al* 2007 *Nucl. Fusion* **47** 74
[196] Oyama N *et al* 2004 *Plasma Phys. Control. Fusion* **46** A355
[197] Romanelli M, Bourdelle C and Dorland W 2004 *Phys. Plasmas* **11** 3645
[198] Angelini B *et al* 2003 *Nucl. Fusion* **43** 1632
[199] Esposito B *et al* 2004 *Fusion Sci. Technol.* **45** 370
[200] Frigione D *et al* 2001 *Nucl. Fusion* **41** 1613
[201] Angelini B *et al* 2005 *Nucl. Fusion* **45** S227
[202] Esposito B *et al* 2004 *Plasma Phys. Control. Fusion* **46** 1793
[203] Jiao Y-M *et al* 2005 *Chin. Phys.* **14** 1600
[204] Xiao Z G *et al* 2003 *Fusion Sci. Technol.* **43** 45
[205] Yang Y *et al* 1999 *Nucl. Fusion* **39** 1871
[206] Xie J *et al* 2001 *Nucl. Fusion* **41** 1495
[207] Xiang G *et al* 2000 *Nucl. Fusion* **40** 1875
[208] Xiang G *et al* 2000 *Phys. Plasmas* **7** 2933
[209] Yang Y *et al* 2002 *Chin. Phys. Lett.* **19** 701
[210] HT-7 Team and Baonian Wan 2002 *Fusion Sci. Technol.* **42** 116
[211] HT-7 Team 2000 *Plasma Phys. Control. Fusion* **42** 135
[212] Messiaen A M *et al* 1996 *Phys. Rev. Lett.* **77** 2487
[213] Hobirk J *et al* 2000 *Nucl. Fusion* **40** 1469
[214] Sakakibara S *et al* 2001 *Nucl. Fusion* **41** 1177
[215] Yamada H *et al* 2001 *Nucl. Fusion* **41** 901
[216] Sakamoto R *et al* 2006 *Nucl. Fusion* **46** 884
[217] Ohyabu N *et al* 2006 *Phys. Rev. Lett.* **97** 055002
[218] Ohyabu N *et al* 2006 *Plasma Phys. Control. Fusion* **48** B383
[219] Ida K *et al* 1996 *Plasma Phys. Control. Fusion* **38** 1433
[220] Lorenzini R *et al* 2002 *Plasma Phys. Control. Fusion* **44** 233
[221] Bartiromo R *et al* 1999 *Phys. Rev. Lett.* **82** 1462
[222] Lang P T *et al* 2003 *Nucl. Fusion* **43** 1110
[223] Horton L D *et al* 2004 *Plasma Phys. Control. Fusion* **46** B511
[224] Urano H *et al* 2004 *Plasma Phys. Control. Fusion* **46** A315
[225] Lang P T *et al* 2004 *Nucl. Fusion* **44** 665
[226] Lang P T *et al* 2006 *Plasma Phys. Control. Fusion* **48** A141
[227] Lang P T *et al* 2005 *Nucl. Fusion* **45** 502
[228] Kallenbach A *et al* 2005 *J. Nucl. Mater.* **337–339** 732
[229] Winter J 1996 *Plasma Phys. Control. Fusion* **38** 1503
[230] Jackson G L *et al* 1997 *J. Nucl. Mater.* **241–243** 655
[231] Bell M G *et al* 1995 *Nucl. Fusion* **35** 1429
[232] Owens D K *et al* 1995 *J. Nucl. Mater.* **220–222** 62
[233] Strachan J D *et al* 1994 *Plasma Phys. Control. Fusion* **36** B3
[234] Strachan J D *et al* 1994 *J. Nucl. Mater.* **217** 145

- [235] Sergeev V Yu *et al* 1998 *Plasma Phys. Control. Fusion* **40** 1785
[236] Khlopov K V *et al* 1997 *Fusion Eng. Des.* **34–35** 337
[237] Kondo K *et al* 1997 *J. Nucl. Mater.* **241–243** 956
[238] Yoshino R, Nakamura Y and Neyatani Y 1996 *Nucl. Fusion* **36** 295
[239] Yoshino R *et al* 1997 *Plasma Phys. Control. Fusion* **39** 313
[240] Pautasso G *et al* 1996 *Nucl. Fusion* **36** 1291
[241] Kuteev B V *et al* 1994 *Fusion Technol.* **26** 938
[242] Taylor P L *et al* 1999 *Phys. Plasmas* **6** 1872
[243] Timokhin V M *et al* 2001 *Tech. Phys. Lett.* **27** 795
[244] Jardin S C *et al* 2000 *Nucl. Fusion* **40** 923
[245] Kuteev B V, Sergeev V Yu and Sudo S 1995 *Nucl. Fusion* **35** 1167
[246] Khlopov K *et al* 2001 *Plasma Phys. Control. Fusion* **43** 1547
[247] Sudo S *et al* 2002 *Plasma Phys. Control. Fusion* **44** 129
[248] Nakamura Y *et al* 2003 *Nucl. Fusion* **43** 219
[249] Tamura N *et al* 2003 *Plasma Phys. Control. Fusion* **45** 27
[250] Nozato H R *et al* 2004 *Phys. Plasmas* **11** 1920
[251] Nozato H *et al* 2005 *Rev. Sci. Instrum.* **76** 073503
[252] Nozato H *et al* 2006 *Phys. Plasmas* **13** 092502
[253] Garzotti L *et al* 2003 *Nucl. Fusion* **43** 1829
[254] Weiland J 2000 *Collective Modes in Inhomogeneous Plasma—Kinetic and Advanced Fluid Theory* (Bristol: Institute of Physics Publishing)
[255] Miyazawa J *et al* 2002 *Plasma Phys. Control. Fusion* **44** A203
[256] Zanza V *et al* 1996 *Nucl. Fusion* **36** 825
[257] Mantica P *et al* 2002 *Plasma Phys. Control. Fusion* **44** 2185
[258] Inagaki S *et al* 2004 *Phys. Rev. Lett.* **92** 055002
[259] Frassinetti L *et al* 2007 *Nucl. Fusion* **47** 135
[260] Dong J-F *et al* 2004 *Chin. Phys.* **13** 379
[261] Egorov S M *et al* 1987 *JETP Lett.* **46** 180
[262] Durst R D, Philips P E and Rowan W L 1988 *Rev. Sci. Instrum.* **59** 1623
[263] Egorov S M *et al* 1994 *Plasma Phys. Rep.* **20** 143
[264] Fisher R K *et al* 1988 *Fusion Technol.* **13** 536
[265] McChesney J M *et al* 1995 *Rev. Sci. Instrum.* **66** 348
[266] Petrov M P *et al* 1998 *Plasma Phys. Rep.* **24** 154
[267] Medley S S *et al* 1997 *Rev. Sci. Instrum.* **68** 336
[268] Parks P B, Fisher R K and McChesney J M 1995 *Nucl. Fusion* **35** 1297
[269] McChesney J M *et al* 1997 *Phys. Plasmas* **4** 381
[270] Redi M H *et al* 1999 *Phys. Plasmas* **6** 2826
[271] Medley S S *et al* 1998 *Nucl. Fusion* **38** 1283
[272] Fisher R K *et al* 1995 *Phys. Rev. Lett.* **75** 846
[273] Fisher R K *et al* 1995 *Rev. Sci. Instrum.* **66** 348
[274] Sasao M, Wurden G A and Mansfield D K 1997 *Fusion Eng. Des.* **34–35** 333
[275] Federici G *et al* 2003 *J. Nucl. Mater.* **313–316** 11
[276] Stacey W M 2001 *Phys. Plasmas* **8** 850
[277] Shimada M *et al* 2004 *Nucl. Fusion* **44** 350
[278] Houlberg W A, Attenberger S E and Grapperhaus M J 1994 *Nucl. Fusion* **34** 93
[279] Mikkelsen D R *et al* 1995 *Nucl. Fusion* **35** 521
[280] Kamelander G *et al* 2004 *Fusion Sci. Technol.* **45** 558
[281] Polevoi A R *et al* 2003 *Nucl. Fusion* **43** 1072
[282] Polevoi A R *et al* 2005 *Nucl. Fusion* **45** 1451
[283] Rasmussen D A *et al* 2005 *Fusion Sci. Technol.* **47** 753
[284] Combs S K, Griffith A E and Foust C R 2001 *Rev. Sci. Instrum.* **72** 273
[285] Parks P B and Perkins FW 2006 *Nucl. Fusion* **46** 770